BRNO UNIVERSITY OF TECHNOLOGY

VYSOKÉ UČENÍ TECHNICKÉ V BRNĚ

FACULTY OF MECHANICAL ENGINEERING

FAKULTA STROJNÍHO INŽENÝRSTVÍ

INSTITUTE OF PHYSICAL ENGINEERING

ÚSTAV FYZIKÁLNÍHO INŽENÝRSTVÍ

MAGNETO-OPTICAL GRADIENT EFFECT IMAGING OF MAGNETIC TEXTURES

ZOBRAZOVÁNÍ MAGNETICKÝCH TEXTUR POMOCÍ MAGNETOOPTICKÉHO GRADIENTNÍHO EFEKTU

MASTER'S THESIS

DIPLOMOVÁ PRÁCE

AUTHOR — **Bc. Tomáš Molnár**

AUTOR PRÁCE

SUPERVISOR — **M.Sc. Jon Ander Arregi Uribeetxebarria, Ph.D.**

VEDOUCÍ PRÁCE

BRNO 2023

BRNO UNIVERSITY OF TECHNOLOGY
FACULTY OF MECHANICAL ENGINEERING

Assignment Master's Thesis

Institut:	Institute of Physical Engineering
Student:	**Bc. Tomáš Molnár**
Degree programm:	Physical Engineering and Nanotechnology
Branch:	no specialisation
Supervisor:	**M.Sc. Jon Ander Arregi Uribeetxebarria, Ph.D.**
Academic year:	2022/23

As provided for by the Act No. 111/98 Coll. on higher education institutions and the BUT Study and Examination Regulations, the director of the Institute hereby assigns the following topic of Master's Thesis:

Magneto–optical gradient effect imaging of magnetic textures

Brief Description:

Nanoscale magnetic textures, consisting of spatially confined non–uniform magnetization configurations, are currently the focus of many research efforts due to their potential integration in magnetic memory, sensing, and logic devices. Their small size and fast dynamics upon application of electric and spin currents make them interesting building blocks for low–power nanoelectronics. The magneto–optical Kerr and Voigt effects enable imaging regions with uniform magnetization within a material, identifying at the same time the existence of magnetic domain walls between them. However, Kerr and Voigt effects cannot resolve the internal spin structure of a domain wall, as its typical size lies under the optical resolution limit. This thesis proposes using the magneto–optical gradient effect, emerging under spatially non–uniform magnetization configurations, to obtain information about the internal structure of nanoscale magnetic textures, such as domain walls. Magneto–optical gradient effect measurements will be attempted in a variety of ferromagnetic and ferrimagnetic thin films and multilayers providing different magnetic textures, such as chiral and non–chiral domain walls.

Master's Thesis goals:

1. Investigation and classification of the magneto–optical gradient effect signals generated by different magnetic textures (e.g. domain walls) and optimization of the measurement geometries using optical microscopy.
2. Fabrication of magnetic thin films and multilayer systems showing magnetic textures of different types (e.g., in–plane and out–of–plane magnetized, ferromagnetic and ferrimagnetic materials)and their structural and magnetic characterization.
3. Imaging of magnetic textures using the magneto–optical gradient effect in an opticalmicroscope.

Recommended bibliography:

MCCORD, J. Progress in magnetic domain observation by advanced magneto-optical microscopy. Journal of Physics D: Applied Physics. 2015, 48(33), 333001.

SCHÄFER, R.; HUBERT, A. A new magnetooptic effect related to non□uniform magnetization on the surface of a ferromagnet. physica status solidi (a), 1990, 118(1), 271-288.

CHEN, G.; MA, T.; N'DIAYE, A.T., et al. Tailoring the chirality of magnetic domain walls by interface engineering. Nature Communications. 2013, 4(1), 1-6.

Deadline for submission Master's Thesis is given by the Schedule of the Academic year 2022/23

In Brno,

L. S.

prof. RNDr. Tomáš Šikola, CSc. Director of the Institute	doc. Ing. Jiří Hlinka, Ph.D. FME dean

Abstract
Foundations of magneto-optics (MO), the field studying the influence of magnetic fields and magnetization on the propagation of light within matter, had been laid over a century and a half ago. Since then, MO has become one of the most widely used methods for magnetic imaging at the micro-scale. In addition to the MO Faraday and Kerr effects, which are linear in magnetization, effects quadratic in magnetization (Voigt or Cotton-Mouton effect) or dependent on magnetization-gradients (gradient effect) were later found. In particular, the MO gradient effect was the last to be discovered, but as it only decorated magnetic domain boundaries, it has not attracted so far the same interest as the Kerr effect for magnetic imaging. This work investigates the usefulness of the magneto-optical gradient effect to characterize nanoscale spin configurations, such as domain walls in perpendicularly magnetized materials. We present a novel experimental approach to reveal the properties of the MO gradient effect by exploiting its symmetries with respect to the polarization of light. Further, we analytically express the corresponding signal using an available theoretical model. By comparing simulated MO gradient effect signals obtained from the transfer matrix method and experimentally retrieved signals, we explore the possibility of characterizing the internal spin structure of nanoscale magnetic domain walls.

Abstrakt
Základy magnetooptiky (MO), oboru zkoumajícího vliv magnetických polí a magnetizace na šíření světla v hmotě, byly položeny před více než půldruhým stoletím. Od té doby se MO stala jednou z nejpoužívanějších metod magnetického zobrazování v mikroměřítku. Kromě MO Faradayova a Kerrova jevu, které jsou lineární v závislosti na magnetizaci, byly později objeveny efekty kvadratické v závislosti na magnetizaci (Voigtův nebo Cottonův-Moutonův jev) nebo závislé na gradientech magnetizace (gradientní jev). Zejména MO gradientní jev byl objeven jako poslední, ale protože zdobí pouze hranice magnetických domén, nepřitahoval zatím takový zájem jako Kerrův jev pro magnetické zobrazování. Tato práce zkoumá užitečnost magnetooptického gradientního jevu pro charakterizaci spinových konfigurací v nanorozměrech, jako jsou doménové stěny v kolmo zmagnetovaných materiálech. Představujeme nový experimentální přístup k odhalení vlastností MO gradientního jevu využitím jeho symetrie vzhledem k polarizaci světla. Dále analyticky vyjadřujeme odpovídající signál pomocí dostupného teoretického modelu. Porovnáním simulovaných signálů MO gradientního jevu získaných metodou přenosové matice a experimentálně získaných signálů zkoumáme možnost charakterizovat vnitřní spinovou strukturu magnetických doménových stěn v nanorozměrech.

Keywords
magneto-optical microscopy, magneto-optical gradient effect, perpendicular magnetic anisotropy, Néel and Bloch magnetic domain walls, differential imaging, transfer matrix method

Klíčová slova
magnetooptická mikroskopie, magnetooptický gradientní jev, kolmá magnetická anizotropie, Néelovy a Blochovy doménové stěny, diferenciální zobrazování, metoda přenosové matice

MOLNÁR, T. *Magneto-optical gradient effect imaging of magnetic textures.* Brno: Vysoké učení technické v Brně, Fakulta strojního inženýrství, 2023. 52 s. Vedoucí práce Jon Ander Arregi Uribeetxebarria.

I declare that I have written my master's thesis on the theme of *Magneto-optical gradient effect imaging of magnetic textures* independently, under the guidance of the supervisor M.Sc. Jon Ander Arregi, Ph.D., and using the sources quoted in the list of literature at the end of the thesis.

Bc. Tomáš Molnár

In the first place, I would like to express my immense thanks to M.Sc. Jon Ander Arregi, Ph.D., for his knowledgeable insights, exemplary supervision, guidance and patience, especially in times of the most need.

I am also incredibly grateful to the entire *Nanomagnetism and Spintronics* research group at CEITEC and Ing. Vojtěch Uhlíř, Ph.D., for their willing help and fruitful and inspiring discussions. My thanks also belong to Prof. Dr.-Ing. Jeffrey McCord for his exceptional leadership and hospitality during my Erasmus stay in Kiel.

Dále bych rád vyjádřil své díky své rodině za nezměrnou podporu nejen při psaní této diplomové práce, ale i během celého studia. Dále bych velice rád poděkoval svým kamarádům za neřídké strhávání mé pozornosti od studijních povinností a také za to, že byli mnohdy úspěšní a napomáhali tak mé duševní pohodě.

CzechNanoLab project LM2023051 funded by MEYS CR is gratefully acknowledged for the financial support of the measurements/sample fabrication at CEITEC Nano Research Infrastructure.

Bc. Tomáš Molnár

Contents

Introduction 1

1. Nanoscale magnetic textures 3
- 1.1. Interactions in magnetic systems . . . 3
- 1.2. Magnetic domains and domain walls . . . 5
  - 1.2.1. In-plane magnetized systems . . . 6
  - 1.2.2. Out-of-plane magnetized systems . . . 10
- 1.3. Chiral and achiral magnetic domain walls . . . 13
- 1.4. Complex nanoscale textures . . . 15

2. Microscopy of magnetic textures 17
- 2.1. Bitter method . . . 17
- 2.2. Scanning probe microscopies . . . 17
- 2.3. Electron microscopies . . . 20
- 2.4. Magneto-optical microscopy . . . 23

3. Magneto-optical effects dependent on magnetization and its gradient 27
- 3.1. The dielectric permittivity tensor . . . 27
- 3.2. Magneto-optical effects' geometries . . . 29
- 3.3. Overview of the magneto-optical gradient effect experiments in the literature 32

4. Sample fabrication and characterization 37
- 4.1. Experimental methods . . . 37
- 4.2. Magnetic characterization . . . 37
- 4.3. Domain wall type determination . . . 38

5. Magneto-optical gradient effect imaging and simulation 41
- 5.1. Can magnetic domain walls be imaged via the longitudinal Kerr effect? . . . 41
- 5.2. Gradient effect dielectric displacement in out-of-plane magnetic domains . . . 42
- 5.3. Magneto-optical effects separation . . . 46
- 5.4. Gradient effect experiments . . . 47
  - 5.4.1. Phenomenology of the gradient effect . . . 47
  - 5.4.2. Separation of the gradient effect components . . . 52
- 5.5. Differential imaging simulations . . . 58

6. Proposal for optical imaging of domain wall type and chirality 62

Conclusion 65

References 66

List of abbreviations i

A. Transfer matrix method ii

B. Light polarization and optical components in the Jones formalism iv

Introduction

The research landscape of magnetism is no longer exclusively scientific, and it has been like this for many years, given the still-enlarging portfolio of industrial applications. Particularly the hard disk drive (HDD) technology, which remains the most dominating digital data storage technology and will continue to be so for many years, possibly even decades. Considering the success of the field of spintronics in commercial magnetic random access memory (MRAM) and domain wall-based multi-turn sensors [1], research efforts toward higher energy efficiency, scalable memory and logic devices, and neuromorphic computing are made.

Next generation magnetic memory cells and logic devices were initially envisioned to be based on nanoscale shift registers via magnetic domain wall displacement. The current-induced displacement is facilitated by the spin-transfer torque (STT), in which spin-polarized current transfers the spin angular momentum from an adjacent magnetic layer having a non-collinear magnetization. The applied voltage acts effectively in such devices as an applied magnetic field, allowing all-electrical control of magnetization dynamics in ultra-fast velocities ($\sim$ 100 m/s) [2]. Unlike STT, spin-orbit torques (SOTs) arise from spin-orbit coupling and angular momentum transfer between conduction electrons and spin reservoir (typically a non-magnetic conductor located in the vicinity of a magnetic layer or the magnetic material itself). SOTs are most effective when the information carrier – the magnetic domain walls – are of Néel type [3]. Alternatively, using other high-mobility magnetic textures, like skyrmions, has been shown to enhance the capabilities of such spintronic devices [4]. Skyrmions are topologically protected, hedgehog-like textures which can be stabilized in layered perpendicular magnetic anisotropy (PMA) systems with interfacial Dzyaloshinskii-Moriya interaction (DMI). Most recently, hopfions – 3D topological solitons with non-trivial knot-like topology – drag an immense amount of attention due to their exotic physics and potential in spin-torque-based devices [5].

Another promising application takes inspiration from human brain architecture and uses various algorithms to produce low-energy-consumption computing systems in order to solve cognitive tasks such as pattern recognition, data analysis, and outcome prediction. Turns out that such a concept of neuromorphic computing binds rather well with spintronics as certain features of spintronics are key in this field, mainly its non-volatile memory, multifunctionality, non-linearity, and dynamics [6]. Neuromorphic chips with integrated STT-MRAMs on top of complementary metal–oxide–semiconductor (CMOS), working as a memory component, have already been used as a proof-of-concept [7]. A variety of spintronic nano-synapses and nano-neurons have been developed; spintronic memristors, just like synapses in the brain, modulate information carried from one neuron to another by passing through an electrical current. Through the progressive transformation of magnetic textures within the memristor by the electric current, its conductance gradually changes due to magneto-resistive phenomena. These changes in individual memristors, mediated by nucleating and moving domain walls or skyrmions, are implemented as changes in computational weights.

What all the mentioned spintronic applications have in common is that they utilize the motion of nanoscale magnetic textures - domain walls, skyrmions, or hopfions (even though their research is still in its infancy). Typically, the dimensions of these textures are around $\sim 10^1$–10^2 nm. In order to study their behavior and structure, their real-time visualization is of huge importance. Nowadays, numerous imaging techniques are considered common practice, and they vary in the physical origin of the interaction with magnetization, spatial and temporal resolution, contrast mechanisms, information depth and acquisition time. Targeting real-space observation of such nanoscale magnetic textures requires the development of ex-

perimental techniques with the ability to resolve magnetization-related information down to the $\sim 10^0$ nm scale and below.

Among one of the most commonly used are scanning probe microscopies, while another large group of imaging techniques stems from the massive development of electron microscopy in recent decades. Some of them rely on secondary electron microscopy, while other very powerful techniques are accessible in transmission electron microscopy. Nowadays, these pronounced techniques are capable of achieving spatial resolution ranges from below 1 nm to 100 nm. However, since these technologies require sophisticated and often very costly equipment, or sometimes even are carried at large-scale facilities (e.g., synchrotron or free electron lasers), these techniques are not easily accessible.

In contrast with the mentioned techniques, the field of magneto-optical (MO) imaging is based on polarized-light microscopy. Given its foundation in optical microscopy, MO comprises a plethora of well-established methods, which depend on polarization-altering phenomena due to interaction with magnetization in a material [8]. MO allows for geometries in transmission as well as reflection, and because we aim at observing magnetic textures that usually occur in multilayered metallic systems, we focus only on MO phenomena in reflection. While MO microscopy is a fast, affordable, and well-established method [9, 10] for magnetic imaging at the $1 - 100$ μm scale and beyond (with special implementations allowing to reach ~ 0.2 μm resolution), it fails to characterize nanoscale spin textures.

The most significant magneto-optical effect in reflection geometry is the Kerr effect, which is linear in magnetization and is hence well suited for imaging of magnetic domains. There are also higher-order MO effects, like the magneto-optical Voigt effect, which is quadratic in magnetization, or the magneto-optical gradient effect, an effect proportional to spatial magnetization gradients. Since magnetization does not change within the domain itself (in general) but rather in areas between the two domains, the gradient effect has the capacity to image non-uniform magnetization textures such as domain walls. Because different domain wall types change magnetization differently, the magnetization gradient is different, giving rise to the idea that the gradient effect could be used to distinguish between domain wall types.

This thesis explores the possibility of the magneto-optical gradient effect utilization in magnetic domain wall imaging in out-of-plane magnetized systems. We analytically describe the measured gradient effect contributions using its dielectric permittivity tensor and a simple dielectric law model. By exploiting the symmetries of the Kerr and gradient effects, we manage to separate them and thus investigate the signals at the domain boundaries. Moreover, we show that it is even possible to separate individual components of the gradient effect dielectric tensor and obtain corresponding boundary contrasts. Finally, we implement more sophisticated numerical approaches to simulate the magneto-optical signals originating from the gradient effect and compare them to the experiments.

In Chapter 1, this thesis focuses on giving a theoretical background on nanoscale magnetism. Chapter 2 overviews various magnetic microscopy techniques, their fundamental principles, and their utility. The main topic of magneto-optics is discussed in Chapter 3, where we discuss chosen magneto-optical effects and summarize the most vital works on the anatomy of the magneto-optical gradient effect. Chapter 4 assembles sample characteristics used in the thesis. The central part of the thesis is covered in Chapter 5, where we define how the magnetization gradients manifest in magneto-optical imaging and compare our measurements with analytical models and simulations. Finally, in Chapter 6, we utilize the theoretical approaches and propose experimental geometries in which differentiation between Bloch and Néel walls could be done via magneto-optical microscopy.

1. Nanoscale magnetic textures

By the end of the 19th century, the joint theory of electric and magnetic fields was already circulating worldwide, leading to the electromagnetic revolution. Despite that, physicists still could not explain why the magnetization of iron is enhanced so enormously, even by applying only moderate magnetic fields. Early in the 20th century, Paul Langevin used a statistical thermodynamics approach to explain paramagnetism. He studied the nature of temperature-dependent magnetization evolution and realized that the elementary magnets in ferromagnetics must be strongly coupled, contrasting with paramagnets [11]. Not too long after Langevin's theory was published, Pierre Weiss introduced the theory of a molecular field exerted by the elementary magnets [12]. Even as preposterous a theory as this one was at that time, Weiss was able to explain the phase transition of ferromagnets above the Curie point, where it loses its extraordinary properties. However, a stumbling rock of the molecular field concept was that the net field calculated by the electromagnetic theory did not correspond to actual experiments by a magnitude of a couple of orders. At that point, the arrival of quantum physics helped to solve the conundrum of the strong magnetic interaction – now explained the Heisenberg exchange interaction [13].

Furthermore, Weiss also predicted that the hysteretic behavior of ferromagnets, together with the abrupt field-induced rise of spontaneous magnetization, is caused by splitting of the body into interconnected magnetic segments. The experimental evidence of the existence of the segments (i.e., magnetic domains) was provided a quarter of a century later, in 1932, by Francis Bitter [14], who applied a magnetic powder on a surface of a magnet and observed its segregation due to local magnetostatic fields. Along with other discoveries in the field, this experimental confirmation enormously helped in the development of magnetic materials. The development went through military purposes during World War II until its fruits were welcomed to a consumer market.

This section covers magnetic textures, ranging from mesoscale magnetic domain types reflecting the materials' inherent properties to their corresponding nanoscale domain wall structures. The energy terms responsible for the domains' appearance and behavior are briefly reviewed.

1.1. Interactions in magnetic systems

Of all elements that naturally occur in the universe around us, only three are inherently *ferromagnets* in normal conditions: iron, cobalt, and nickel. Individual atoms possess a magnetic moment, which is, of course, not the case only for these elements. Suppose we put these elements in a crystal lattice. In that case, we find that these atoms arrange themselves in such a manner that the magnetic field of all the atoms is enhanced—this kind of behavior groups the family of ferromagnetic materials. Even though other elements may have a magnetic moment on their own, once they are ordered in a lattice, what will happen is that the net magnetic field will cancel out – these are called *paramagnets*. Lastly, materials whose atoms possess no magnetic moment whatsoever are called *diamagnetic* materials.

However, why do paramagnetic materials not have any net magnetic field? The reason is that in these materials, individual magnetic moments do not interact with each other and thus can have statistically random orientation; magnetization $\vec{M}$ (sum of all magnetic moments per

unit volume) then goes to zero. The situation is different in ferromagnets, where the moments, in fact, do interact with each other.

On the level of quantum mechanics, the electrons belonging to ferromagnetic atoms have uncompensated spins. Moreover, these uncompensated spins are the ones responsible for the interaction; this was first described by Heisenberg [15]. He introduced an energy term called the *exchange interaction*, defined as the scalar product of the two neighboring electron spins $\vec{S}$, summing all neighboring pairs in a lattice gives

$$E_{\text{exchange}} = -\sum_{ij} J_{ij} \vec{S}_i \cdot \vec{S}_j, \tag{1.1}$$

where J is the exchange constant. Given that the magnetic field is enhanced in ferromagnets so that magnetic moments (hence spins as well) tend to be parallel to each other, the exchange constant has to be $J > 0$.

The exchange constant highly depends on the distance and arrangement of atomic sites in a crystal lattice. It is also material dependent and relates to the exchange interaction strength and, therefore, its distance impact. In certain materials, it happens that J goes to negative values. Should the adjacent spins stay parallel, the energy increase would be enormous; hence the spins flip so that the neighboring ones are antiparallel. Because each spin is compensated by its neighbor's, such materials produce no magnetic field on the outside – they are classified as *antiferromagnets*.

Another energy contribution is actually one which allows us to manipulate with material's magnetization $\vec{M}$. It is known as the Zeeman energy, and it writes as follows

$$E_{\text{Zeeman}} = -\vec{M} \cdot \vec{B}_{\text{ext}}, \tag{1.2}$$

where $\vec{B}_{\text{ext}}$ is the external magnetic field acting upon the magnetization. One of the many ways ferromagnetic materials can be classified is by how easily they can be magnetized; in other words, by how much the Zeeman energy outweighs other energy terms. If they are magnetized easily ($|\vec{B}|$ in the range of units of mT), they are called magnetically soft; in the other case, we call them magnetically hard materials.

In condensed matter physics, we can define an order parameter for each phase, which shows substantial difference when the system is above or below a *critical temperature* T_c. This order parameter goes to zero for $T > T_c$ and is non-zero for $T < T_c$. In ferromagnets, the order parameter is simply magnetization. When a ferromagnet exceeds this critical temperature, it becomes paramagnetic; for ferromagnets, we call it the Curie temperature.

So far, we did not put any constraints on the dimensions of the ferromagnetic body under consideration. Suppose we have a finite, bulk ferromagnet. The majority of atoms that are within the bulk feel the presence of their neighbors and keep their properties as if they were in an infinite medium. On the other hand, much fewer atoms that find themselves close to a surface do not have all the neighboring atoms. This absence of neighbors at the surface forces the system to break the symmetry, causing the surface atoms to have substantially different properties than the bulk atoms. Such symmetry breaking applies as well for magnetic properties. If we scale down the dimensions even more and increase the surface-to-bulk atoms ratio, the surface atoms' properties become increasingly important. In the case of ferromagnets, the surface atoms have reduced electronic bandwidth due to the lack of nearest neighbors, leading to an increased density of states at the Fermi level [13, 16]. They are therefore expected to have enhanced magnetic moments.

Since this thesis focuses on magnetic thin film and multilayer systems with thicknesses in order 1 nm and below, here we focus on magnetic phenomena that become relevant at these length scales. The interaction energies leading to non-uniform magnetization configurations – or magnetization textures – at the micro- and nanoscale will be introduced. It is seen that these interactions lead to the existence of spatially confined magnetic textures such as domain walls. More exotic magnetic features, such as skyrmions, will be discussed afterwards.

1.2. Magnetic domains and domain walls

Let us assume a ferromagnetic body in which all the spins are bound only via the exchange interaction. Such a state would mean that all spins are lined up perfectly. Even though this uniform magnetization state is a ground state, it is actually not a stationary one. In real magnetic systems, there are more energy terms whose competition eventually leads to the uniform magnetization state collapsing. However, the exchange interaction, which is the largest in short ranges, still applies, binding the closest spins together. These spins then form non-uniform magnetization regions within which their orientation is unchanged, and we call them *ferromagnetic domains*. The boundary between ferromagnetic domains where the spins transition from one domain orientation to the other is termed magnetic *domain wall* (DW).

The arrangement of domains and DWs, that is, the magnetic microstructure, forms a bridge between the essential physical properties of a magnetic material and its mesoscopic properties. In contrast with bulk magnets, thin films or magnetic multilayers form domains which can be well considered as 2D textures. Domain dimensions can range from higher hundreds of micrometers in thick films (hundreds of nanometers) to hundreds of nanometers in ultrathin films or multilayers. At the same time, DW widths can be smaller by a margin of several orders, from tens to hundreds of nanometers [9]. Usually, DWs can be considered magnetic singularities; despite their small dimensions, they can play a prominent role in the possible application of a particular system.

In order to describe the magnetic microstructure of a material, we usually reach for *micromagnetic theory*. In micromagnetic theory, continuous magnetic moments describing a given microstructure are used. Based on the famous paper by Landau and Lifshitz [17], micromagnetics is described using a variational principle. Simply put, magnetic moments align themselves in such a way that the system's total free energy is minimized. The total free energy comprises energy terms corresponding to various magnetic phenomena. This energy minimization principle leads to a set of non-linear and non-local equations, so-called *micromagnetic equations*. However, in most cases, we rely on a theory that uses discrete, uniformly magnetized domains together with results from the micromagnetic theory (such as DWs) – the *domain theory*. While the micromagnetic theory is possibly too complex if we are interested only in domain configurations, the domain theory is just an indispensable tool.

An important aspect that plays a significant role in magnetic domain formation is the presence of the so-called *magnetic dipolar fields* (*magnetostatic* or *demagnetizing* fields). The dipolar fields' origin is evident when we consider one of Maxwell's equations $\nabla\vec{B} = 0$ and apply the $\vec{B}$-field equation for materials $\vec{B} = \mu_0(\vec{M} + \vec{H})$. By substituting back, we get $\nabla\vec{M} = -\nabla\vec{H}_d$. We usually write the dipolar field energy as [13]

$$E_{\text{dipolar}} = \frac{1}{2}\mu_0\vec{H}_d \cdot \vec{M}. \tag{1.3}$$

Assuming a case with no externally applied field, we can say that the $\vec{H}_d$-field acts as a magnetic field stemming from magnetization. This statement is true even for individual magnetic moments. Individual magnetic moments serve as sources of the dipolar field. Sometimes, they are thought of as the so-called magnetic charges. Within each domain, this dipolar field adds up and acts on the other domains in the vicinity, affecting their orientation as a result.

Another phenomenon can be exhibited as follows. Take a piece of cobalt and magnetize it in one direction. Then rotate it by $90°$, and you will see that the magnetization response is very different. This anisotropic behavior of magnetic materials is referred to as magnetocrystalline anisotropy and plays a cardinal role in domain configuration processes. The anisotropy occurs because cobalt forms a hexagonal structure, making it more favorable for the magnetic moments to align along the $[0001]$ axis. The axis in which moments tend to stay is called the easy axis. Perpendicular to that is a direction with the least preferable orientation – the hard axis. There can even be multiple easy and hard axes in materials with different crystalline structures. In cubic materials, like iron, the easy axes are cube edges $<100>$, whereas the diagonals $<111>$ are the hard axes. When a material has one easy axis, this property is called uniaxial anisotropy, whereas, for two easy axes, the terminology used is biaxial anisotropy. This phenomenon acts as another intrinsic energy term contributing to the total energy pool. We can describe it most simply for uniaxial anisotropy as [13]

$$E_{\text{anisotropy}} = K_1 \sin^2\theta, \tag{1.4}$$

where θ is an angle between magnetization and the easy axis, and K_1 denotes the strength of the tendency to stay magnetized in the easy axis.

The presence of dipolar fields in a ferromagnetic material and its crystalline microstructure causes some materials to prefer to line their domains' magnetization out of the surface plane. Such a phenomenon is called *perpendicular magnetic anisotropy*; given the geometry, magnetic domains here have only a single degree of freedom – they point either up or down. In contrast, other materials instead tend to stay in the surface plane of a material, causing them to have two degrees of freedom, allowing for more complexity of the domain microstructure. In usual thin films, these two preferential orientations are the most dominant. But in general, real materials may have a more complex interplay of different effects; hence the preferred magnetization orientation may be arbitrary.

So far, we have roughly discussed only a few of the most important energy contributions dominant in most ferromagnetic systems. More detailed analysis of these contributions, along with other energy terms that can play major roles in magnetization arrangement, can be found in [9, 13, 16, 18]

1.2.1. In-plane magnetized systems

A. $180°$ **domains**

Let us start with a case of oppositely oriented in-plane magnetic domains with a planar DW. Most commonly, the DW will lie along the domain's axis. Such magnetic structure is called $180°$ *domain wall.* Mathematically we can describe the two domains as $\vec{m}_1$ = (0, 1, 0) for $x < 0$ and $\vec{m}_2$ = (0, -1, 0) for $x > 0$, but as we know, magnetization cannot just switch abruptly; it has to transition gradually. There are two elemental types of transitions, i.e., the DWs.

i. *Bloch wall*

If the magnetization rotates parallel to the DW plane, the magnetization within the wall will not create any dipolar field. The absence of a dipolar field is particularly beneficial for this kind of system. A DW having this type of transition is typically called the *Bloch wall*, in honor of Felix Bloch, who came up with a continuous wall transition [9, p. 202]. The Bloch DW then takes a form [9, p. 203]

$$\vec{m}_{\text{Bloch}} = (0, \text{tgh}(\xi), 1/\cosh(\xi)), \tag{1.5}$$

where $\xi = x\pi/W$, and W is the DW width.

Generally speaking, Bloch walls within in-plane magnetized systems are present if their thickness is above the Bloch wall width, typically 10–100 nm.

ii. *Néel wall*

The second way magnetization can transition is by rotating around the axis parallel to the DW. This type of DW is called the *Néel wall*. In contrast with the Bloch wall, magnetization inside the Néel wall does create a dipolar field, which affects the internal structure of the wall. The most straightforward case – the symmetric Néel wall – decomposes into a sharply localized core and two extensive tails, where most of the rotation occurs. The wall's dipolar field least influences the tails, whereas the core is primarily characterized by the field's pattern [9]. In a first approximation, neglecting magnetostatic fields, we can write

$$\vec{m}_{\text{Néel}} = (-1/\cosh(\xi), \text{tgh}(\xi), 0). \tag{1.6}$$

Both DW types are schematically illustrated in Fig. (1.1).

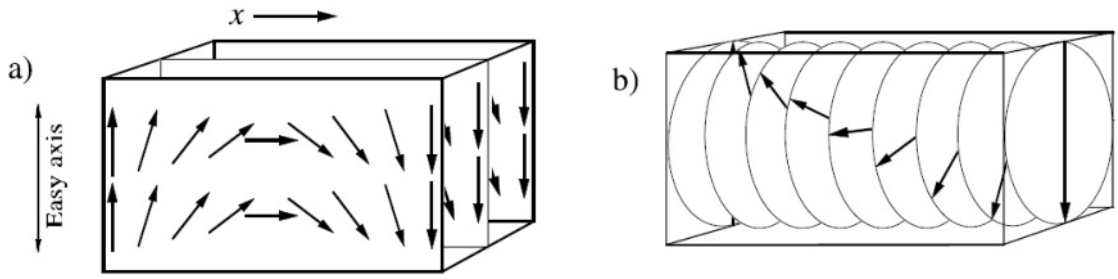

Figure 1.1.: Schematic description of the internal magnetic structure of a) a Néel wall and b) a Bloch wall in 180° domains. Adapted from Ref. 9.

Another example of domain configuration with a 180° wall is the so-called head-on DW. In head-on walls, both neighboring domains' magnetization vectors are perpendicular to the boundary. Usually, it is not very straightforward to achieve such domain configuration due to its high dipolar field energy.

One way to obtain the head-on walls is to fabricate submicron wires, as performed by Nozaki *et al.* [19]. Another way was utilized in a work by Schäfer *et al.*, where they used exchange-bias systems [20]. The exchange bias is achieved by coupling an antiferromagnet and a ferromagnet; this interaction is strong enough to overcome the magnetostatic fields and thus enables the formation of head-on DWs. In such a case, the DW is most likely Néel type.

B. 90° **domains**

As DWs significantly contribute to total energy, one of the mechanisms to bring their energy cost down is to form walls with lower rotation angles. In addition to 180° DWs, another noteworthy group is the 90° *domain walls*. In thin films, the 90° walls are typically Néel walls. According to a micromagnetic model introduced by Néel [21], the 90° Néel wall has approximately 12% of the energy of the 180° Néel wall [9, p. 249]. As a result, it can be favorable for the domains to split into multiple domains with 90° walls instead of having a single 180° wall. A typical example of this splitting into subdomains with 180° DWs corresponds to the case of *cross-tie domains* [22], see Fig. (1.2).

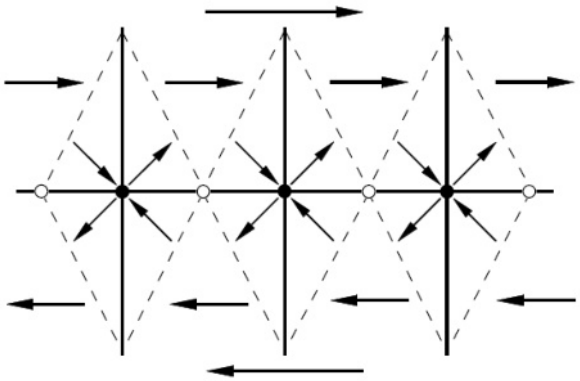

Figure 1.2.: Schematic depiction of cross-tie domains at the boundary of 180° in-plane domains. Breaking into multiple domains with lower wall angles at the cost of additional DW energy can be energetically more favorable. Adapted from Ref. 9.

Generally, 180° in-plane domains occur in samples with a strong uniaxial anisotropy, although not exclusively. 180° domains create dipolar fields that act on the domains themselves, but the domains keep their magnetization orientation because of the strong anisotropy. In cubic materials, which have biaxial anisotropy, the anisotropy is weaker; thus, the domains' magnetization is forced to align with the dipolar fields. This way, the dipolar fields are minimal, and the dipolar energy is reduced. Usually, we refer to the domains formed by this mechanism as *flux closure domains*.

A characteristic flux closure pattern, the Landau pattern, is shown in Fig. (1.3a). In Landau patterns, the magnetization forming the flux closure is present only in discrete directions, meaning that not all stray field energy is suppressed. It is possible to have a domain configuration in which this stray field energy term is brought to a minimum. This configuration is the so-called magnetic vortex. In magnetic vortices, the magnetization curls continuously around its center, known as the vortex core; see Fig. (1.3b). Usually, vortices do not occur in continuous films, so if there is a need for their study, it is necessary to fabricate patterned micro- or nano-sized disks from soft magnetic materials. Let us look at the spin orientation from outside the vortex toward the core. We find that the spin at the very center has trouble finding any suitable in-plane orientation, so instead, it flips into an out-of-plane direction. One parameter that describes a vortex is its polarity, whether the core points up or down. The second vortex parameter is polarity; a vortex can have either a clockwise or a counterclockwise sense of circulation. Moreover, because the polarity and circulation of a vortex are independent, it has four possible states, which allows for a promising application – multi-bit memory cells [23].

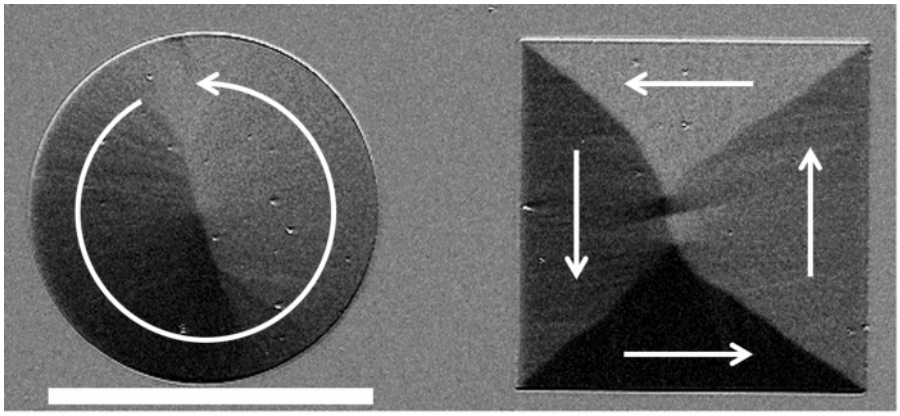

Figure 1.3.: Formation of curling in-plane magnetic domains acting to close magnetic flux, typical for soft magnetic films. Patterned NiFe (permalloy) microstructures showing a magnetic vortex (left) and a Landau pattern (right), imaged by Kerr microscopy (own measurement). The arrows indicate the magnetization orientation. The scale bar is 50 µm.

Another example of flux closure domains, which may not be evident at first sight, is depicted in Fig. (1.4a) from the top view. Even though there are 180° domains on a surface, which, as said earlier, are hardly flux closure domains, the magnetic flux closes as we look under the surface. In these domains, known as V-lines [24], a subsurface domain nucleates with a magnetization orientation perpendicular to the surface, closing the flux. This subsurface domain forms the shape of the letter "V" in a cross-section with its apex in the DW at the surface, as shown in Fig. (1.4b).

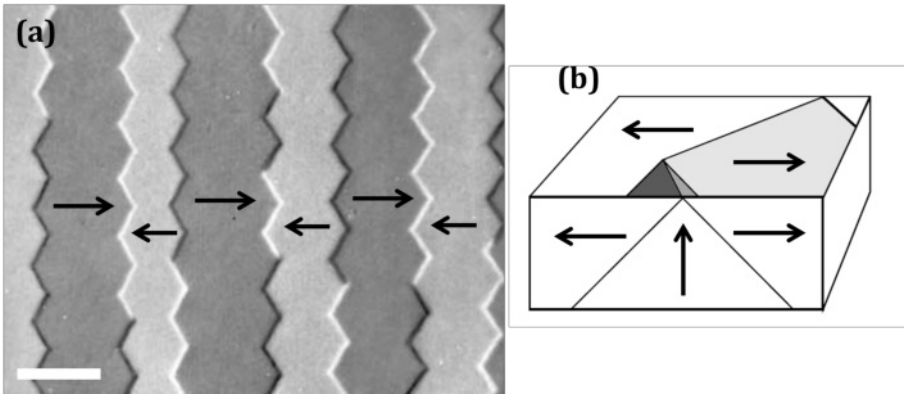

Figure 1.4.: Representation of magnetic flux-closure domains where the surface regions form head-to-head domains, while at their intersection, a subsurface perpendicularly oriented domain appears. a) Top-view V-line domains imaged using the Kerr Microscope. The scale bar corresponds to 10 µm. b) Schematic cross-section of the V-line domain structure. Adapted from Ref. 9.

So far, we have covered only domains magnetized in-plane of material strictly (with a slight exception of V-lines). The following sections will provide an overview of out-of-plane domains, which brings us closer to this thesis's study subjects.

1.2.2. Out-of-plane magnetized systems

Earlier, we pointed out the existence of perpendicular magnetic anisotropy (PMA) – a magnetization's tendency to lie perpendicularly to a surface, yet its origin was not explained. Very thin magnetic films typically promote perpendicular anisotropy, whereas in-plane anisotropy is favored as the material becomes more and more bulk-like. Nevertheless, most studies dealing with the interplay of these types of anisotropies are done in magnetic multilayer systems, whose development was boosted with an industrial application of PMA in HDDs, MRAMs, and sensors [25]. They commonly define an effective anisotropy K_{eff}, which can be separated into the surface or interface contribution K_S and volume contribution K_V [26]

$$K_{eff} = K_V + \frac{2K_S}{t}, \tag{1.7}$$

with t denoting the thickness of the magnetic layer. The contribution from a volume anisotropy is mainly attributed to dipolar fields; large numbers of dipoles in bulk create large dipolar fields, which lead to alignment along a surface. In contrast, the interface anisotropy stems from spin-orbit coupling and closely relates to the electronic structure of the layers.

A typical example of K_{eff} dependence done on Co/Pd multilayers with constant Pd layer thickness and varying Co layer thickness studied by den Broeder *et al.* [26] is shown in Fig. (1.5). Positive K_{eff} values represent perpendicular anisotropy, and negative ones represent parallel anisotropy. In this study, den Broeder *et al.* show that the K_{eff} strongly depends on what atoms constitute the non-magnetic interlayer spacers by replacing Pd with Pt, Au, Ir, and others. A helpful rule of thumb can be deduced from here, namely, that increasing the non-magnetic layer thickness favors the interfacial anisotropy, thus increasing the magnetic layer transition thickness from perpendicular to in-plane anisotropy.

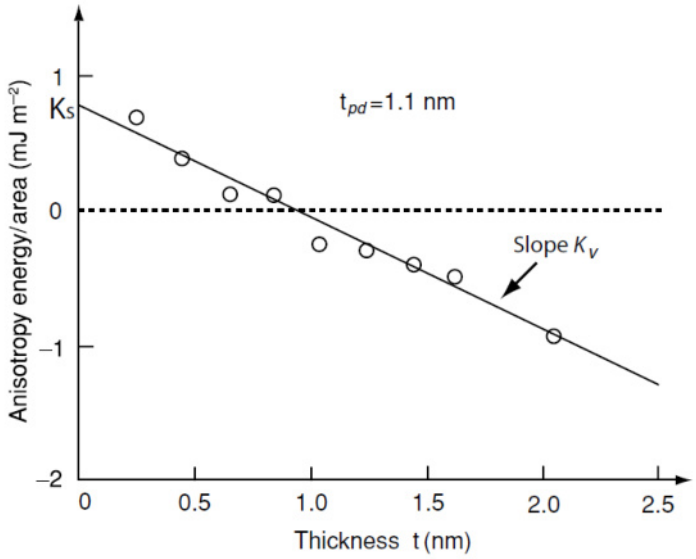

Figure 1.5.: Dependence of the effective magnetic anisotropy energy per unit area on the thickness of the Co layer in Co/Pd multilayers with constant Pd thickness. Positive values of the anisotropy energy reflect the existence of PMA, whereas negative values correspond to the easy-plane anisotropy case. Taken from Ref. 13.

Another critical aspect of multilayers is the domain size. Various applications may require various shapes or sizes of domains. The thicknesses of magnetic and non-magnetic layers in a

stack and the number of repetitions must be tuned precisely to achieve the intended properties. Typically, a single stack with constant thicknesses and guaranteed PMA is chosen. The number of repetitions is then optimized for a particular application. For instance, in a study conducted by Hellwig *et al.* [27], they show that in a given $[\mathrm{Co/Pt}]_N$ multilayer system, starting with a low number of repetitions ($N = 5$) results in a relatively low number of large domains, increasing the repetitions ($N = 20$) leads to a drop of mean domain size and increases their count, further increase causes arguably a linear increase of domain size and decrease in their count. The described dependence and corresponding domain images are illustrated in Fig. (1.6). The domains appearing in multilayers with higher repetitions are usually referred to as *maze patterns* or *stripe domains*. In contrast, the larger domains in low-repetition multilayers are called *bubble domains*.

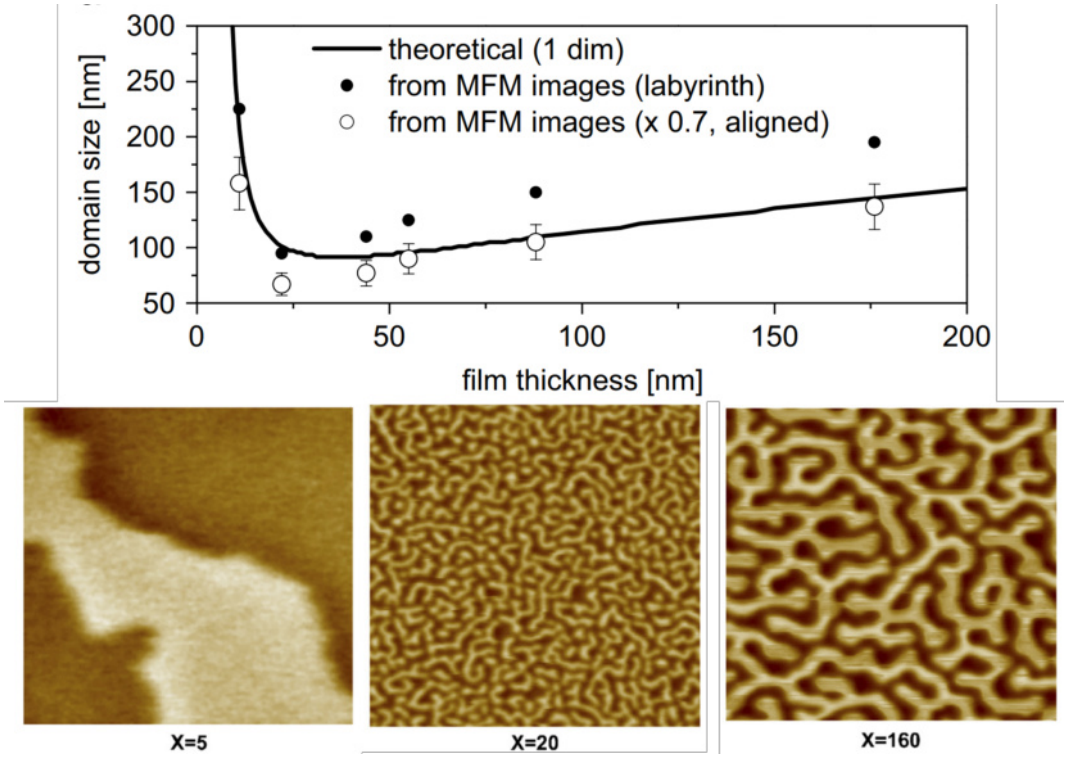

Figure 1.6.: Top panel: dependence of the mean magnetic domain size in $[\mathrm{Co/Pt}]_X$ multilayers on the total Co thickness in the stack. Bottom panel: typical magnetic domain images for multilayer samples with X repetitions, measured by magnetic force microscopy. Adapted from Ref. 27.

A. **Stripe domains**

Stripe domains usually occur in samples that are highly susceptible to magnetic fields. This susceptibility means the domain structure may be easily magnetized while applying a magnetic field along the easy axis. However, it also means that the domains can be strongly affected also by a magnetic field applied perpendicular to the hard axis. Similarly, as in the $180°$ in-plane domains, the out-of-plane magnetized domains can have either a Bloch or a Néel wall. Since stripe domains are relatively narrow, a relatively large proportion of the domain configuration comprises DWs. As a result, applying a low in-plane and out-of-plane magnetic field simultaneously leads to "organizing" the initially arbitrary maze pattern, as shown in Fig. (1.7). Increasing the in-plane magnetic field component leads to thinning of the stripe domains,

which eventually break into a bubble lattice. Applying the magnetic field solely in the in-plane direction then leaves us with mixture domains, simply the coexistence of stripe domains and bubble lattice. Interestingly enough, all these domain states are eventually metastable states, which are stable even after removing the external magnetic field. Such occurrence and stability of the metastable states is a typical feature of domain configurations in systems with perpendicular anisotropy.

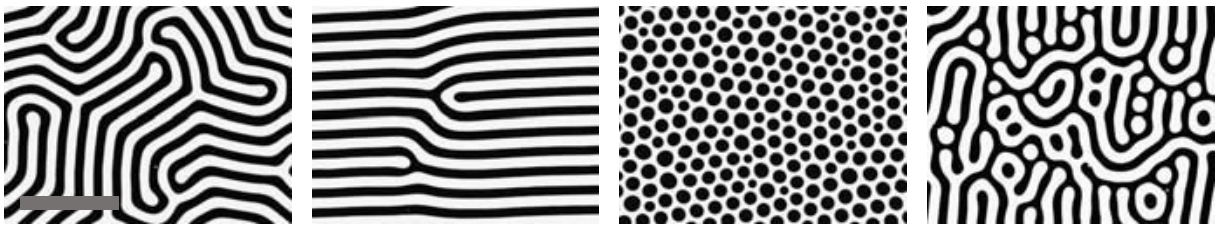

Figure 1.7.: Stripe domains in bubble garnet film with PMA. Remanent magnetization states after saturating the sample at an angle of a) 90°, b) 20°, c) 1°, and d) 0° from the sample plane. The scale bar in a) is 25 μm. Taken from Ref. 9.

B. **Bubble domains**

As discussed earlier, in contrast with the maze-pattern-systems, bubble domains typically appear in multilayer systems with low repetitions; they as well appear in very thin films or garnets. This can also be explained using bubble theory [9], which shows that periodic domains are not energetically favorable in magnetic systems with magnetic layer thicknesses lower than the characteristic length.

Such bubble domains' characteristic is a high DW mobility. Because these types of domains possess global non-equilibrium character, their nucleation is a thermally activated process. Hence, they often nucleate around defects or similar local irregularities since the local dipolar fields tend to be enhanced in their vicinity. The high DW mobility then causes it to be more favorable to expand the existing domains rather than nucleate new ones.

Even though the DW energy cost contributes largely to the total energy of a system, different DW types do not influence a static bubble shape. However, suppose we apply a magnetic field on a nucleated bubble and go to a dynamic regime. In that case, the internal DW structure starts playing a role in how the bubble domain expands. If the magnetic field is applied along the easy axis, nothing too unexpected happens; the bubble expands symmetrically in all directions. However, if we add a field component applied along the hard axis, the system's symmetry is broken, and thus the bubble will expand asymmetrically. The effect of the in-plane magnetic field on bubble domain expansion is depicted in Fig. (1.8). The explanation for this behavior lies in the internal structure of the wall. While the in-plane magnetic field is parallel to magnetization on one side of the bubble and thus favors its expansion, the opposite side experiences an antiparallel in-plane field, resulting in less favorable expansion. Changing the in-plane field amplitude and tracking the expanding bubble velocities along different directions can give us insight into the DW's internal structure. This methodology is now known as the *asymmetrical bubble domain expansion.*

The asymmetrical bubble domain expansion method is often used to distinguish between Bloch or Néel walls. In the case of a bubble with a Néel wall, the asymmetrical expansion is visible in the direction of the applied in-plane field. Increasing the in-plane field will lead

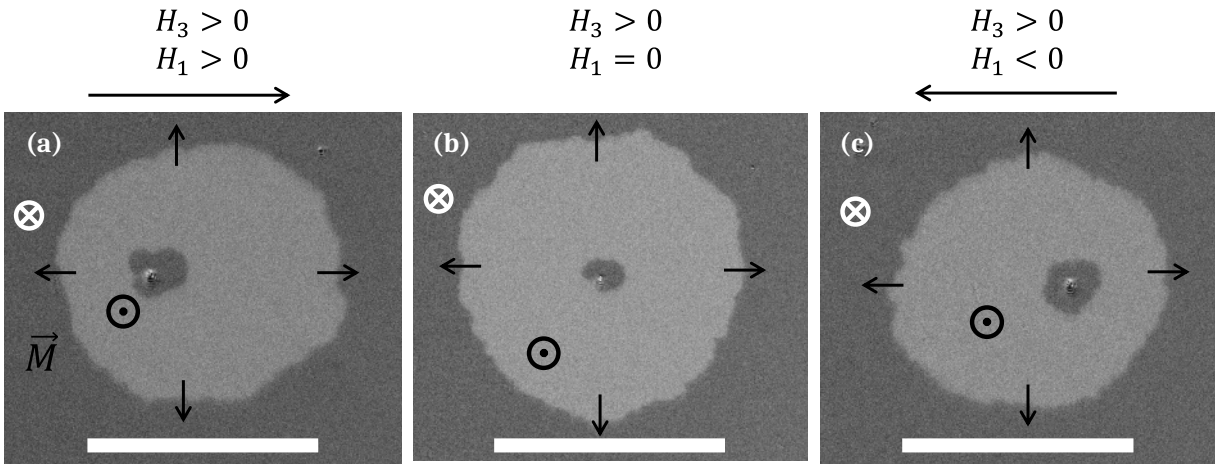

Figure 1.8.: The effect of crossed external magnetic field on the expansion of a bubble domain with a Néel wall, causing its asymmetrical lateral expansion (own measurement via polar Kerr microscopy). Magnetic fields are applied a) both out-of-plane and in-plane, b) only out-of-plane, c) out-of-plane and in-plane in the opposite direction. H_1 and H_3 are the in-plane and out-plane fields, respectively.

to a more pronounced expansion of the favorable wall. However, when a bubble possesses a Bloch wall, the bubble expands symmetrically along the applied field direction. Even though this method may, in most cases, provide an understanding of the DW type, in general, multiple factors unrelated to magnetism can also contribute to bubble expansion, such as surface topography, DW pinning sites, and the quality of a sample's interfaces [28].

So far, we have only stated explicitly when domains with perpendicular anisotropy have a Bloch or a Néel wall. Whether the system has one or the other DW type is frequently governed by the presence of the *Dzyaloshinskii-Moriya interaction*. The following section will discuss this other energy term and its consequences.

1.3. Chiral and achiral magnetic domain walls

While DWs in in-plane magnetized systems had been vastly studied thanks to their relatively large sizes, those in out-of-plane magnetized systems were, for a long time, out of the scope of detailed investigations due to their small sizes. Therefore, the consensus, from a theoretical perspective, had been that these domains possess only Bloch walls.

However, relatively recent research has shown that the presence of an additional magnetic interaction can tip the balance between preferential Bloch or Néel walls in magnetic multilayers with PMA [29]. The additional energy term was found to be the less explored antisymmetric exchange or *Dzyaloshinskii-Moriya interaction* (DMI) [30, 31], described as

$$E_{\mathrm{DM}} = \sum_{ij} \vec{D}_{ij} \cdot \vec{S}_i \times \vec{S}_j, \tag{1.8}$$

where $\vec{D}_{ij}$ is the DMI vector whose magnitude denotes the DMI strength. Given the cross-product in the DMI equation, the adjacent spins find it more energetically advantageous to be perpendicular to each other. The perpendicular spins alignment acts directly in contrast to the Heisenberg exchange interaction. In ferromagnetic materials, the exchange interaction is

usually much stronger than the DMI; hence the collinear spin alignment prevails. Yet, even though usually relatively weak in ferromagnets, DMI influences the DW's internal structure. Of course, the DMI can modulate even the magnetic structure of antiferromagnets, as was shown by Bode *et al.* [32], where its strength was even comparable to that of the exchange interaction.

The origin of DMI lies in the spin-orbit scattering of electrons in an inversion-asymmetric crystal structure [30, 31]. At the interface of a magnetic and non-magnetic layer, the electrons of a magnetic layer couple via the spin-orbit interaction with the non-magnetic metallic atoms. The coupling strength typically rises with the atomic number of the non-magnetic elements; for this reason, usually heavy metals are used. In a symmetrical case, where the magnetic layer is sandwiched between two non-magnetic symmetrical layers, one interface creates a certain coupling, while the other interface creates an inverse coupling, thus effectively canceling the effect of DMI. Let us remove one of the interfaces; now, the system lacks structural inversion symmetry, the spin-orbit coupling is not canceled, and thus, the system retains the DMI. To be more exact, the DMI arising under the described interfacial conditions classifies as *interfacial DMI*. There are also other ways to break the structural symmetry, for instance, curving the magnetic material in a particular way [33], which falls under a whole increasingly promising field of magnetism: curvilinear magnetism [34]. For our purposes, only the interfacial DMI is of importance; hence we will address it simply as a general DMI and forget about DMI induced otherwise.

Until now, we were concerned only about one characteristic of DMI, its strength. However, by no means the less important feature is the chirality – the spin-rotation sense. In out-of-plane magnetized systems with no DMI, hence with Bloch wall, left- and right-handed rotation of spins within the DW are energetically degenerate states. Since both rotational senses cause the same energy contribution, thus none is generally preferential. Nevertheless, one of the two has to appear, which rotational sense is chosen is thermally driven. In a macroscopic view, the number of left- and right-hand rotation walls is compensated; because of this, the Bloch walls are often called *achiral walls*, as they do not present any specific chirality.

In contrast, in continuous films with DMI, the DWs are of Néel type. The sign of the DMI vector indicates the sense of spin rotation, the chirality. Since the DMI is present globally along the whole interface, DWs in such a system have one particular chirality; thus, they are usually described as *homochiral walls*.

The strength, as well as the DMI sign, depends vastly on what atoms constitute the interface. As the interaction is more prominent when heavy metals are present in one of the boundaries, the most commonly used elements are Pt, Ir, Au, W, and Cu. Given the interfacial character of the DMI, it is possible to greatly influence its effect by adjusting the structural asymmetry. For example, Chen *et al.* [29] showed that Fe(2.5)/Ni(2) bilayers (with thicknesses in monolayers, ML) grown on Cu(001) crystal had right-handed chirality. In contrast, the observed chirality was left-handed when they switched the bilayer order. Furthermore, in another study [35], Chen *et al.* also showed that in a Ni(2 ML)/[Co(1 ML)/Ni(2 ML)]$_2$/Ir(t_{Ir})/Pt(111) system changing the Ir layer thickness leads to complete inversion of chirality. Namely, starting at $t_{\mathrm{Ir}} = 0$ ML, right-handed chirality prevailed, and increasing the thickness to 2.5 ML resulted in Bloch walls. Further increasing above 3 ML was considered as a bulk Ir mode completed the transition to left-handed wall chirality. Similar results were accomplished in a system with a single Co film, done by Hrabec *et al.* [36].

1.4. Complex nanoscale textures

In this section, we will cover other types of magnetic textures, textures whose overall sizes are comparable to DW widths, which, together with their high mobility capabilities, make them promising subjects of technological applications [37]. Among the most prominent are magnetic random-access memories and magnetic sensors. One of the topics that have caught huge attention in nanomagnetism circles is the so-called *magnetic skyrmions*. Essentially, skyrmions are local chiral swirls of magnetization, which, at first sight, resemble small magnetic bubbles. Similarly to bubbles, skyrmions can be of Bloch or Néel type; see illustration in Fig. (1.9). The crucial difference between a bubble and a skyrmion is the chirality. Most commonly, the chirality is achieved by the DMI, already discussed in the previous section. In contrast with bubbles, which usually expand after applying an external magnetic field [38] or passing an electric current [39], skyrmions move as though they were magnetic particles – for that matter, skyrmions are often described as *magnetic solitons*.

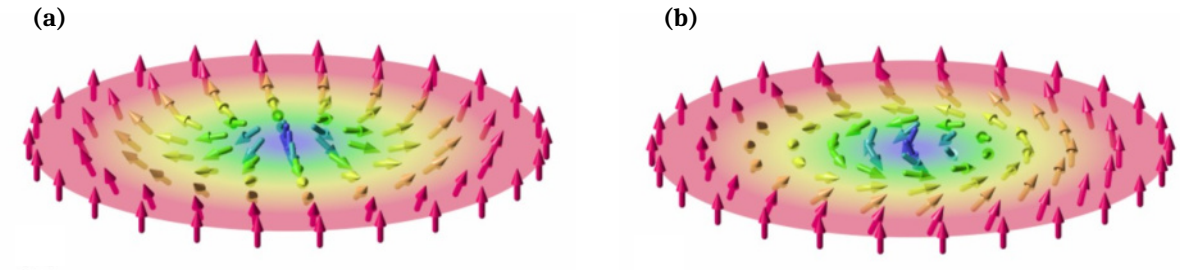

Figure 1.9.: Representation skyrmions, topologically protected hedgehog-like nanoscale spin configurations. a) Néel type, and b) Bloch type skyrmion. Taken from Ref. 40.

The self-localized wave packets or solitons, can be found virtually in any non-linear media. One of their great advantages is that they can travel over long distances without changing shape because their dispersion is countered by constituent non-linear phenomena. Solitons are a general concept and thus appear in a surprisingly wide range of branches of physics, from non-linear optics and particle physics, through molecular biology, to astrophysics and oceanography [41]. Of course, magnetism is among those fields; hence we have the skyrmions. Furthermore, skyrmions are topologically protected objects, which can be imagined as a knot in a rope; skyrmions cannot be simply "unwound" into a uniform magnetic state [42]. The energy barrier suppressing the "unwinding" of the skyrmion is caused mainly by the exchange interaction.

To this day, multiple approaches have been attempted to nucleate skyrmions. One of the successfully predicted and later experimentally confirmed was by a method called "skyrmion blowing". The method utilizes patterned magnetic micro-wires connected via a narrow neck. Stripe domains are nucleated in one of the wires, then passing a current will push the domains through the neck, and as they enter the second wire, the stripe domains effectively split into skyrmions [43]. Another technique to nucleate skyrmions is using out-of-plane magnetic field pulses [44]. The magnetic field pulses break the individual stripes into skyrmions, forming a skyrmion lattice. Even though the mentioned methods lead to multiple skyrmion nucleation, nucleating a single skyrmion at room temperature, essentially a goal of the skyrmion research enabling the said technological applications, remains a challenge.

As aforementioned, skyrmions possess high mobility. So far, using current-driven motion, the maximum velocities can reach up to lower hundreds of meters per second [39]. However, an unwanted effect comes in. Passing a current through a wire with skyrmions results not

only in their longitudinal displacement but also in a transverse displacement caused by the skyrmion Hall effect [45]. The skyrmion's topological charge causes this undesired deviation.

Nevertheless, there is another rather exotic class of magnetic solitons with no topological charge; hence their current-driven motion is axial. This class covers 3D magnetic solitons with a non-trivial knot-like magnetic texture called *hopfions*, illustrated in Fig. (1.10). Potentially, hopfions could be superior to skyrmions as information carriers; however, their properties are predominantly studied theoretically, as their nucleation and observation are still open challenges to overcome [46].

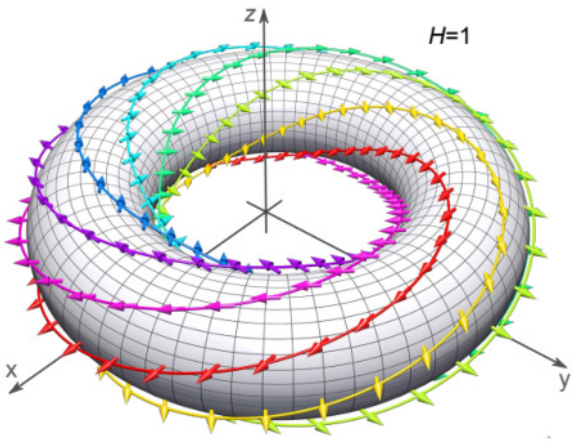

Figure 1.10.: Schematic of the complex topological knot-like three-dimensional spin configuration known as hopfion. Taken from Ref. 46.

Until now, we discussed the magnetic domains, the boundaries within them or DWs, and some examples of rather special magnetic textures. We described their basic properties, in which materials, and under which conditions they appear. In order to understand the magnetic configurations more and thus be capable of developing materials with particular properties, we must be able to observe them. The following section gives an overview of magnetic microscopy methods and their underlying principles.

2. Microscopy of magnetic textures

In the past, within the magnetism research era of the beginning of the 20th century, magnetic properties could only be studied non-locally and in bulk-like materials. Even though a lot could be said about a magnetic material from its bulk properties, the magnetic microstructure, which directly influences the magnetization behavior of the materials, could not be probed anyhow. The magnetic domain concept was generally accepted, yet no convincing experimental evidence existed. It was not until 1931 that Francis Bitter provided images of non-uniformly magnetized separate regions that changed shape after applying an external magnetic field, finally proving that the magnetic domains concept is actually correct. In the decades following this discovery, more and more magnetic microscopy techniques emerged, such as scanning probe microscopies, electron microscopy, or even polarized light microscopy. Each has its limitations and benefits. They also vary in how the magnetization is retrieved, if it is direct magnetization observation, or if it observes the dipolar fields. Thus, the magnetization has to be often reconstructed indirectly.

The following sections contain a brief review of the main magnetic microscopy techniques that are most widely employed within nanomagnetism research. Special emphasis is given to the capability of the technique to image nanoscale spin textures (e.g., magnetic DWs). A more detailed account of these methods may be found in Refs. 9, 10.

2.1. Bitter method

Bitter introduced a powder pattern imaging technique that is now commonly known as the *Bitter method*. He applied a colloidal solution of magnetic particles on the surface of a Co crystal [14]. Magnetic particles, attracted by the dipolar fields, accumulated in places where the dipolar field gradient was the strongest, i.e., at magnetic DWs. A regular optical microscope was sufficient to observe the surface on which the DWs were highlighted. See the original Bitter method patterns in Fig. (2.1). The Bitter method is a simple technique that does not require complex equipment; it remains a valid and important method for domain observation to this day.

One of the advantages of the Bitter method is that it does not require virtually any surface treatment; however, the sensitivity and resolution increase if the surface is polished finely. Another indisputable advantage is that it is equally well suited for rough and irregular surfaces (e.g., the magnetic band of credit cards) [9]. The Bitter method locates the boundaries between microscale magnetic domains, but does not offer any information about their character.

2.2. Scanning probe microscopies

Magnetic force microscopy (MFM)

MFM is basically a modification of the well-known *atomic force microscope* (AFM). In AFM, an atomically sharp tip on a free end of a cantilever is brought above a surface under investigation. The cantilever deflects as its tip atoms feel the presence of surface atoms. We can measure this deflection and then let the cantilever scan over the sample surface; like this, it is possible to reconstruct the sample morphology. Usually, the cantilever deflection is measured by shining a laser beam at the back side of the cantilever, from which the beam is reflected onto a quadrant

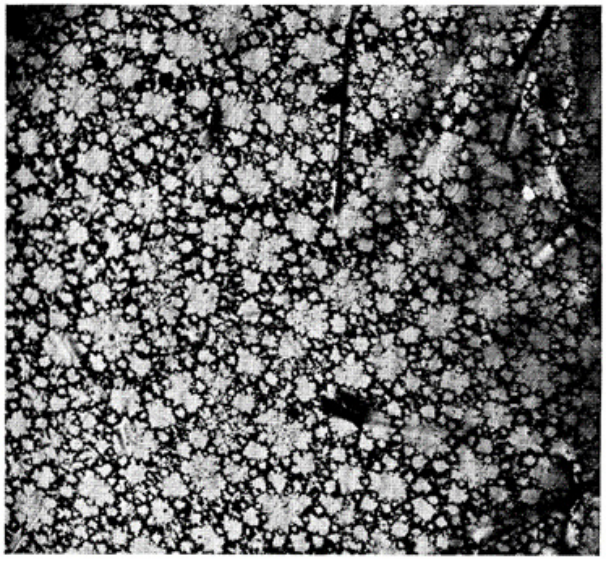

Figure 2.1.: Imaging of magnetic domains in polished hexagonal Co crystal via the Bitter method. The approximate magnification is 70×. Taken from Ref. 14.

detector. This method is called contact mode; in this mode, the tip is usually closer to the surface. There is also another mode called tapping mode, in which the cantilever is further from the surface, and we force it to vibrate at its resonance frequency. As the deflecting forces act upon the tip, the cantilever vibration slightly changes; the amplitude or phase change is then again used to obtain the surface morphology.

Including magnetic field effects is analogous to inserting an additional contribution to the string stiffness of the cantilever. Thus, MFM can measure dipolar fields above the sample surface. However, how can we separate it from the other forces if we add another force contribution to the equation? At first, the surface is scanned at a closer distance. After that, the scan is performed a second time with a larger surface-to-tip distance. The two scans are subtracted, the information about surface morphology cancels out, and we get purely a magnetic field response [9].

Since specimens with PMA have relatively large dipolar fields originating from the domains, MFM is a particularly well-suited method to image them. Even so, DWs are very small in those systems and produce insignificant dipolar fields compared to those stemming from domains. Eventually, for those reasons, imaging DWs in perpendicularly magnetized systems is a challenging process [47]. On the contrary, in in-plane magnetized films, domains themselves do not generally create significant dipolar fields that exit the in-plane film geometry. Therefore, they cannot be directly visualized. For in-plane magnetized films, DWs are responsible for the largest dipolar fields exiting the sample and hence for the MFM image contrast. The lacking domain contrast makes it easier to study the wall's internal structure, and makes it possible to distinguish between Bloch and Néel wall types [48].

One of the most crucial features of MFM is tip preparation. The tip is commonly made from a Si crystal etched into an atomically sharp tip. Having an as sharp tip as possible is of general interest for achieving higher spatial resolution. However, for magnetic imaging, the tip must be coated with a proper magnetic film.

In general, no coating can be applied in all specimens with appropriate sensitivity, where the coating selection is hindered mainly by the tip's stray field influencing surface magnetization and vice versa. The surface-tip magnetic interactions are negligible if the sample surface

is magnetically soft and the tip is hard, producing weak dipolar fields. Consequently, the resulting image can be understood as a magnetic charge distribution rather than a magnetization distribution [49]; for this matter, it is usually referred to as a charge contrast mechanism. This eventuality can be especially well visible in the case of in-plane flux closure domains, where the domain wall is Néel-type.

In most cases, the tip and sample magnetization configurations cannot be considered completely rigid. If the interactions are fairly weak, the surface dipolar fields cause slight magnetization rotation in the tip or vice versa. The first case happens particularly if a magnetically susceptible tip scans a hard magnetic material. The magnetization rotation is a subtle and, most importantly, reversible effect. Finally, the weak rotation manifests as a disruptive background signal, the so-called susceptibility contrast. In reality, the charge and susceptibility contrasts are measured simultaneously, yet they can be separated upon combining the data retrieved in two scans with opposite magnetization orientations of the tip. Hence, if we sum the two scans, we obtain pure charge contrast, whereas if we calculate a difference, the susceptibility contrast is isolated [50].

Lastly, if the stray field from the tip is too strong, magnetic configurations at the sample can be modified irreversibly. The artifacts resulting from these irreversible processes are the so-called hysteresis effects and are connected to DW motion. In the scanned image, DW displacements are relatively easily recognizable as discontinuities. Alternatively, DWs can be "dragged" by the dipolar field of the tip in every pass of the scan, resulting in blurry distortions of the DW area. Sometimes, such DW dragging can be utilized to move the walls into particular positions or even to stimulate skyrmion nucleation and motion [51].

MFM is, compared to other techniques, quite slow. Hence in a regular domain observation, it may not always be the first method of choice. Nevertheless, MFM is a relatively simple and accessible imaging technique that is valued for its high spatial resolution (typically $\sim$ 30 nm [9]) and lack of surface preparation requirement. In Fig. (2.2), exemplary MFM data are shown where the possibility of visualizing DWs is explored.

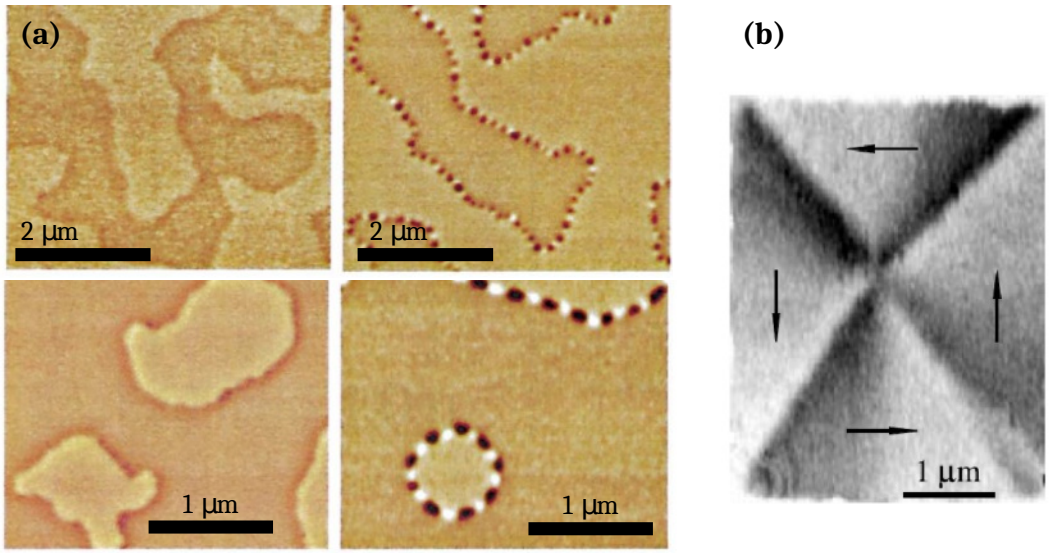

Figure 2.2.: MFM imaging of DWs in a) antiferromagnetically coupled magnetic multilayers with PMA [52], and b) an in-plane Landau pattern [53].

Nitrogen-vacancy (NV) magnetometry

Another technique that may be considered as a pinnacle among scanning probe microscopies for magnetic imaging is NV magnetometry, which essentially utilizes a probing tip finished with a single electron spin [54]. The diamond probe consists of a single point defect in the lattice, whose nearest neighbor is substituted with a nitrogen atom. Ultimately, the nitrogen atom and the neighboring vacancy form a pair in which an uncompensated spin may occur. By scanning the tip over a sample surface and by optically detecting magnetic interaction sensed by the spin at the NV defect, this novel microscopy technique allows for magnetic imaging with very high spatial resolution ($\sim$ 1–10 nm) [55]. It has been recently shown that NV magnetometry is capable of obtaining information on the internal DW structure of ultrathin ferromagnetic films, distinguishing Bloch and Néel wall types as well as their chiralities. In addition, it can also determine the magnetization tilting of the DW with an angular resolution of $\sim 1°$.

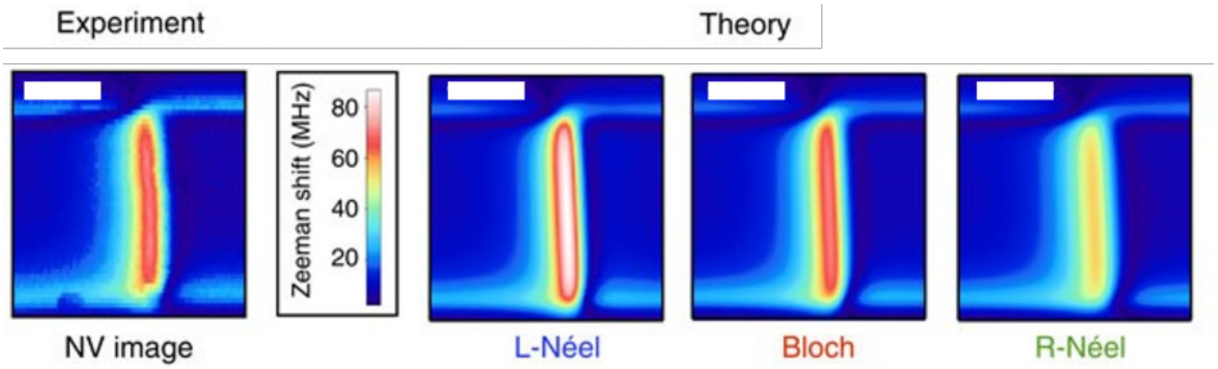

Figure 2.3.: Comparison of NV imaging of a domain wall in PMA sample with simulation corresponding to left-hand chirality Néel wall, Bloch wall, and right-hand chirality Néel wall. Edited from Ref. 55.

2.3. Electron microscopies

Nowadays, electron microscopy is one of the most extensively utilized methods for microscopic specimen analysis. We find its applications in a broad spectrum of scientific fields. There are several branches of electron microscopy, which differ based on what type of signal they measure. But what all electron microscopes have in common is the following functioning principle: an electron gun, i.e., the electron source, generates a beam of electrons that is sent toward the investigated sample. The electrons in the beam, called primary electrons, interact with the sample; the primary electrons can collide with electrons bound to the sample's atoms and force those electrons out of the sample, called secondary electrons. The primary electrons can also be elastically scattered from the sample atoms' nuclei; these electrons are referred to as backscattered electrons. If the investigated specimen is thin enough, the primary electrons can pass through the sample, known as transmitted electrons.

Apart from secondary, backscattered, and transmitted electrons, plenty of other interactions can happen; however, the techniques we will describe only utilize those three types. These electrons are then detected, and each type contains different information about the specimen. While the transmitted electrons can be detected simply by putting a detector from the back side of the electron beam illumination, the other two electron types can be distinguished mainly

by their energies. Since backscattered electrons scatter elastically, they do not lose energy, whereas the secondary electrons have much lower energies.

Nevertheless, performing magnetic imaging requires adjustments to standard electron microscopy equipment. In particular, we cover magnetic imaging via *scanning electron microscopy* (SEM), *low-energy electron microscopy* (LEEM), and *transmission electron microscopy* (TEM).

Scanning electron microscopy with polarization analysis (SEM-PA)

SEM is an electron microscope in which the electron beam is focused on the specimen surface to make the smallest spot possible. Electromagnetic deflectors then scan with the electron beam over the specimen surface, and the detector counts the yield of secondary electrons detected at each spot of the scan. This way, an image is formed, each pixel containing information about how many secondary electrons have been collected.

In the general case, the emitted secondary electrons have spin, of course, but its direction is arbitrary. However, if we scan over like this a ferromagnetic sample, the secondary electrons keep a certain preferential spin orientation corresponding to the domain magnetization from which they were forced out. The speciality of *SEM with polarization analysis* (SEM-PA) is that it uses a spin detector, called a Mott detector, which enables determining the spin orientation of the collected secondary electrons.

SEM-PA is a complex experimental technique since it needs an ultra-high vacuum and a very high degree of cleanliness at the specimen's surface. One of the limitations is that the total yield of secondary electrons, which keep their spins, is very low; furthermore, if they collide with other particles on their way to the detector, their spin orientation changes. As a result, SEM-PA is sensitive only to the top nanometer of the sample surface [9]; hence, the surface must be well cleaned. Due to the low yield, high exposure times are required, which adds another challenge to the system's overall stability. On the other hand, if all conditions are set properly, SEM-PA can provide an excellent spatial resolution up to 3 nm [56], and is also able to recover a full surface magnetization orientation. Given its resolution, it is possible to observe magnetization directly at the DW [57]. In Fig. (2.4) see results of SEMPA imaging.

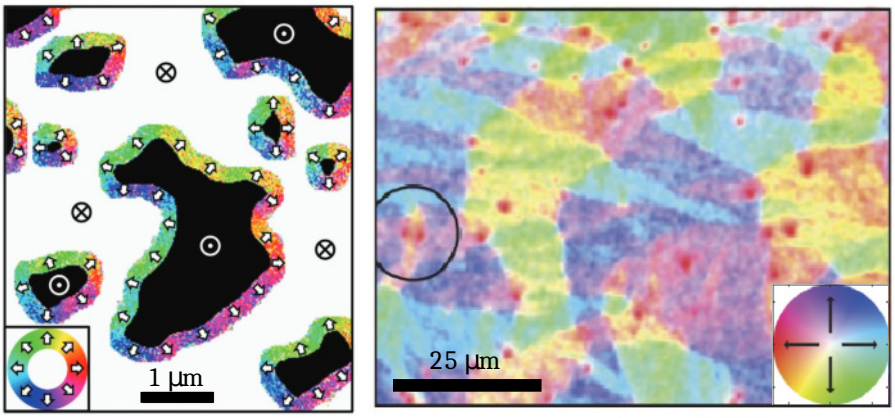

(a) **(b)**

Figure 2.4.: SEMPA imaging of a) DWs in out-of-plane domains [58], b) in-plane magnetized domains [59].

Spin-polarized low-energy electron microscopy (SP-LEEM)

LEEM is one of the most recognized in situ techniques for surface structure or morphology studies. In contrast to the conventional SEM, LEEM is a so-called cathode lens electron microscopy technique, meaning that the sample itself serves as a source emitting electrons to the objective lens. Generally, multiple accounts can stimulate electron emission using electrons, photons, ions, or other means. Another difference between with SEM-type microscopies is that LEEM is not a scanning technique. The imaged sample surface is stimulated simultaneously; hence the image can be acquired in real-time. For our purposes, we will focus solely on the case of stimulation by electrons. The low energy electrons, illuminating the surface, scatter inelastically from the topmost atoms of the surface. In crystalline samples, this scattering is accompanied by diffraction, from which LEEM also benefits to provide additional information on the sample's lattice or the surface's lattice reconstruction. The final contrast in the image is formed by the directionality of the electron scattering [60].

Nevertheless, regular LEEM is not generally able to visualize visualize magnetic domains. In order to do so, an electron gun emitting well-defined spin-polarized electrons needs to be implemented instead of a common electron gun, hence the name *spin-polarized LEEM* (SP-LEEM). Once the electrons leave the gun, they pass through magnetic rotators, which rotate their spin-axis orientation $\vec{P}$. Electrons then scatter asymmetrically from the ferromagnetic surface with a particular magnetization configuration $\vec{M}$, which gives a contrast proportional to $\vec{P} \cdot \vec{M}$. The difference in scattering from oppositely oriented magnetizations is mostly attributed to the exchange interaction [61].

The most significant SP-LEEM advantage and limitation at the same time is its surface sensitivity. Connected with high surface sensitivity is the necessity of ultra-high vacuum. Also, given the surface sensitivity, it is not commonly possible to visualize the surface of a sample prepared outside the vacuum chamber. Similarly to SEM-PA, the surface needs to be well-prepared and cleaned. Nevertheless, SP-LEEM is capable of excellent magnetic imaging with a best lateral resolution of 2 nm [62], which makes it possible to visualize even DWs conveniently. Magnetic imaging is, however, limited to static imaging with no, or very weak, external magnetic fields, since their presence would deflect the electron beam originating from the sample, precluding magnetic imaging. See examples of imaging in Fig. (2.5).

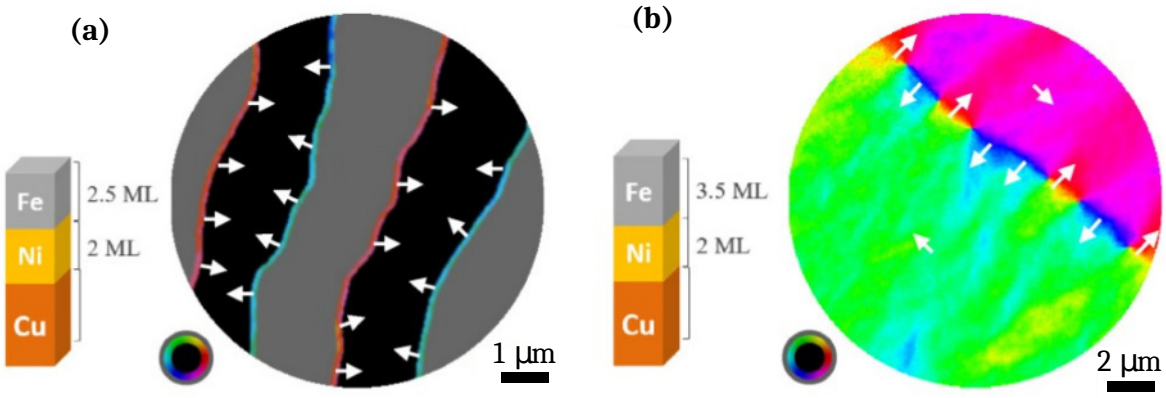

Figure 2.5.: SP-LEEM imaging of a) DWs in magnetic multilayer with PMA and b) for a sample with in-plane domains. Taken from Ref. 63.

Lorentz transmission electron microscopy (L-TEM)

So far, we have described magnetic imaging methods via electron microscopy utilizing secondary and backscattered electrons. This last electron microscopy technique, TEM, uses the scattering of the high-energy primary electrons from the specimen nuclei, which pass through the whole specimen cross-section.

Nevertheless, the transmitted electrons scattered on the nuclei in magnetic specimens do not contribute to a magnetic signal. The deflection of the primary electrons causes the magnetic signal in TEM due to a magnetic field within the specimen. The driving factor for the deflection is the Lorentz force

$$\vec{F}_L = -e\vec{v} \times \vec{B}, \tag{2.1}$$

where e is the electron charge, $\vec{v}$ is its velocity, and $\vec{B}$ is the magnetic field exerted by the sample on the traveling electron. Note that only $\vec{B}$ components perpendicular to $\vec{v}$ contribute to the electron deflection [9]. Due to its physical origin, this technique is called the *Lorentz-TEM* (L-TEM).

We distinguish two L-TEM imaging modes. First is termed as the *Fresnel mode*, in which an objective aperture is centered, and the objective lens is defocused. This way, opposite magnetic domains deflect the primary electrons centrosymmetrically; therefore, they do not contribute to a magnetic signal when projected into an image plane. Nevertheless, since magnetizations on both sides of the DW deflect electrons in opposite directions, the electrons have to be deflected either into or away from the DW [64]. Consequently, the Fresnel mode can image DWs [65]. The second L-TEM imaging mode is the *Foucault mode*. Oppositely to the Fresnel mode, the objective lens is focused in Foucault mode, whereas the aperture is displaced. The aperture displacement breaks the centrosymmetry, and thus electrons deflected from one domain get through the aperture, whereas the electrons deflected from an opposite domain are blocked. As a result, a domain image can be formed [64].

L-TEM is another formidable technique with a very high magnetic imaging resolution of 2 nm [64]. Even though regular TEM reaches even higher sub-angstrom resolution [66], this is not achievable for L-TEM methods. Using a high magnification lens in magnetic materials is limited because the strong lens magnetic field can reach lower units of teslas, eventually erasing any magnetic configuration. Compared to other magnetic imaging techniques, a unique limitation of L-TEM is the sample preparation. The sample has to be sufficiently thin, up to hundreds of nanometers, for the electron beam to shine through it. Commonly, it is also challenging to apply external magnetic fields and do the imaging at the same time. Whereas with the Fresnel mode, it is impossible to image domains, the lateral resolution and contrast are excellent, the Foucault mode brings limitations to the spatial resolution and can directly visualize individual domains. The major constraint accompanying all mentioned electron microscopy techniques is the overall high cost of the equipment [9]. See the examples of L-TEM imaging in Fig. (2.6).

2.4. Magneto-optical microscopy

Last but certainly not least is a method of probing magnetic configurations using polarized light, i.e., magneto-optics. In general, magneto-optics tracks the slight rotation of incident light polarization state caused by the interaction of light with the sample's magnetization. One of the magneto-optical microscopy categorizations is based on scanning versus parallel

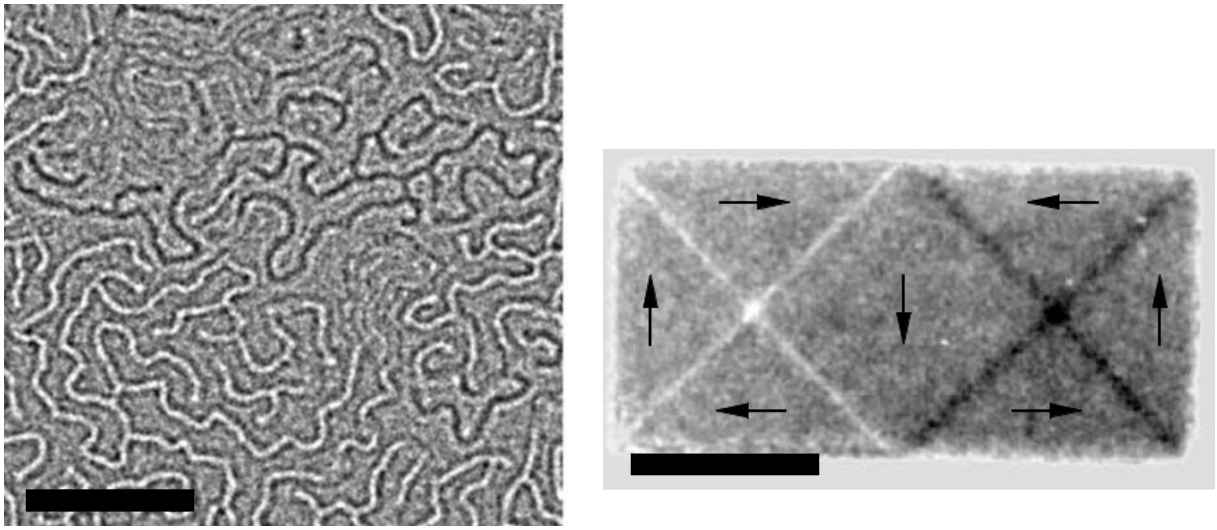

(a) **(b)**

Figure 2.6.: L-TEM imaging of a) an out-of-plane magnetized system with Bloch walls [67] and b) an in-plane magnetized patterned film sustaining a Landau pattern [9].

(i.e., wide-field) imaging. Given its utility, versatility, and accessibility, wide-field magneto-optical microscopy is arguably the most common technique used for magnetic domain imaging. Another distinction is rooted in whether we detect transmitted or reflected light. While the effect associated with the rotation of polarized light upon transmission is called the *Faraday effect*, it is feasible only in transparent specimens, making it inapplicable for optically thick magnetic materials, despite being highly reflective. The reflected light geometry, however, is advantageous for domain observation in such specimens and, for this reason, is our target of interest. The so-called *magneto-optical Kerr effect* exploits reflected light intensity variations upon the polarization state change of light. Nevertheless, the Kerr effect and other more nuanced magneto-optical effects will be discussed in more detail in chapter 3.

The wide-field magneto-optical technique in reflection is typically performed in a so-called *Kerr microscope*. The Kerr microscope is basically a modified polarization microscope that enables high spatial resolution with high magnification [68]. In a typical Kerr microscope, unpolarized light from a visible part of the spectrum passes through a linear polarizer; the well-defined linear polarization state is modified as the light reflects from a magnetic specimen. The reflected light then passes through another linear polarizer, called an analyzer, whose polarization axis is nearly perpendicular to that of the polarizer. As a result, the unchanged polarization component is blocked, and only the polarization component that changed due to Kerr effect gets to the detector. In real measurements, the reflected light also acquires ellipticity, which needs to be removed to increase contrast conditions. Typically, a rotatable phase retarder is placed between the sample and analyzer; therefore, only linearly polarized light gets to the analyzer [10]. See a simplified Kerr microscope schematic in Fig. (2.7).

As said beforehand, a visible light source is most commonly utilized in Kerr microscopy. However, magneto-optics may be performed even at much shorter wavelengths. Magneto-optics in the X-ray spectrum of the electromagnetic radiation constitutes very different phenomena than visible light magneto-optics, which comes with more methods of magnetic analysis, but complications as well. For this reason, X-ray magneto-optics could be considered a field of study on its own and thus would require a separate section [9].

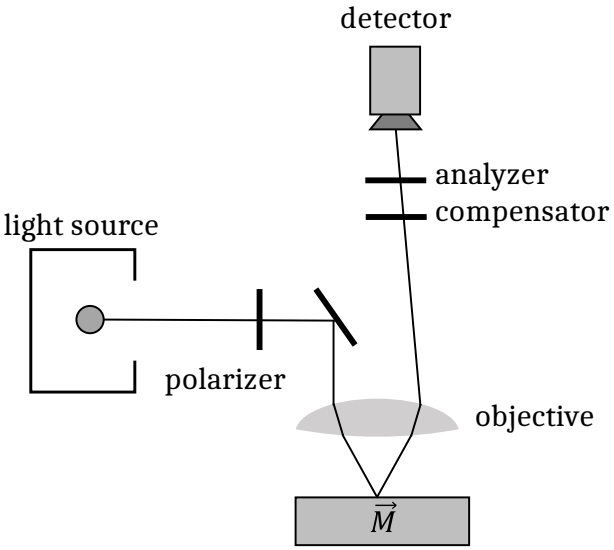

Figure 2.7.: Schematic of the Kerr microscope illustrating a single light beam path to the detector after being polarized, reflected from a sample, and passing through the compensator and analyzer before reaching the detector camera.

Possibly one of the most prominent advantages of Kerr microscopy is the high performance for little initial investment. Compared to other magnetic imaging techniques, dynamic processes may be observed at high speeds in Kerr microscopy. The sample might be manipulated with magnetic fields, mechanical stresses or temperature variations during observation. Also, the observations can be done in ambient conditions; thus, no vacuum systems are generally needed. On the other hand, the investigated specimens must be reasonably flat and smooth, at least on the scale of the attempted imaging resolution. Since it is a light microscopy technique, it can hardly compete with electron microscopy or scanning probe microscopy techniques in terms of spatial resolution, which is limited to about 300 nm in the best case scenario [68].

X-ray magnetic dichroism

In typical magneto-optical microscopy, a visible light source is utilized. However, the magnetic properties of materials may be exceptionally well studied using soft X-ray radiation. The use of X-rays involves wholly different areas of physics compared to most common magneto-optics. The most dominant interactions of X-rays with the material are through atomic resonances and photoabsorption. By measuring the absorption rates of X-rays spectroscopically, it is possible to probe the inner electronic shells of materials [69]. Since the presence of magnetic moments in material causes energy splitting of electronic states, the absorption edges also shift. And it is this difference of absorption (i.e., dichroism) in areas with opposite magnetic moments that allows performing magnetic imaging.

Analogically to the Kerr and Faraday effects, it is possible to observe ferromagnetic domains through a mechanism called *X-ray magnetic circular dichroism* (XMCD). In the XMCD mechanism, oppositely oriented magnetic moments absorb circular polarizations at different rates. Moreover, for ferromagnetic domain imaging, we can also observe a mechanism called *X-ray magnetic linear dichroism* (XMLD), which can image antiferromagnetic domains. In contrast to XMCD, in XMLD, perpendicularly oriented magnetic moments absorb the incident linear polarizations differently.

XMCD/XMLD imaging is implemented either in the photoemission electron microscopy mode or, alternatively, in scanning transmission geometry. While both approaches can lead to the best resolution of about ~ 10 nm, typical spatial resolutions are of the order of a few tens of nm. More complete specifications of X-ray magnetic dichroism mechanisms may be found in Refs. 70, 71.

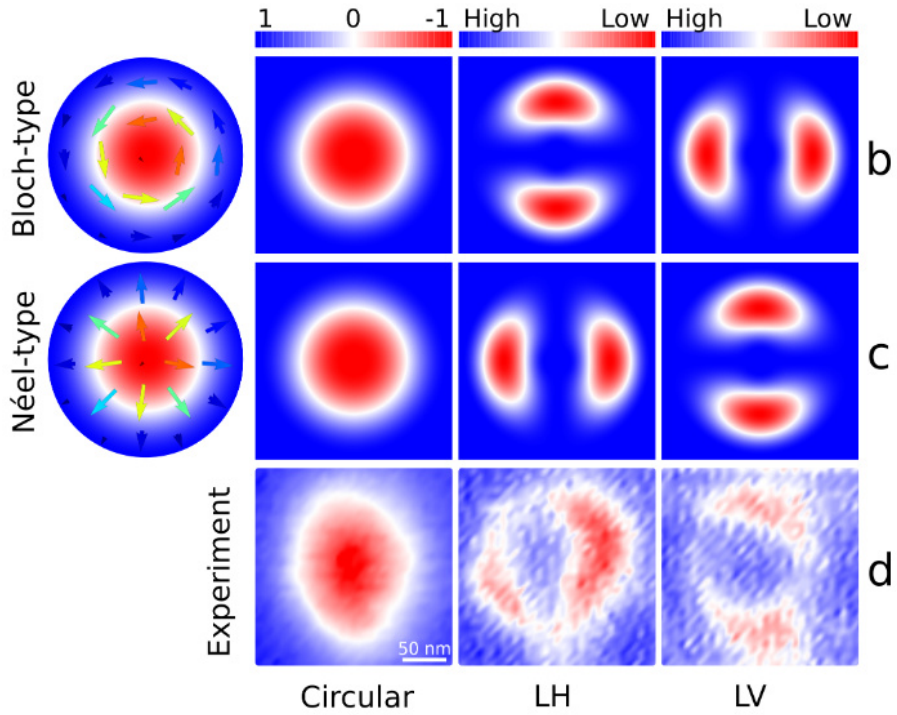

Figure 2.8.: Identification of magnetic DW type for a skyrmion in a $DyCo_3$ film. It is concluded that the skyrmion boundary consists of a Néel wall by comparing simulations and XMCD/XMLD microscopy measurements using circular, linear horizontal (LH) and linear vertical (LH) incident X-rays. Taken from Luo *et al.* [72].

In general, XMCD/XMLD related measurements cannot resolve the internal magnetic structure of nanoscale textures such as magnetic DWs. However, a very recent study presents an approach based on the combination of XMCD and XMLD microscopy, which together with simulations, permits identifying the DW type in sub-micron skyrmions in a ferrimagnetic thin film (see Fig. 2.8) [72].

3. Magneto-optical effects dependent on magnetization and its gradient

Nowadays, magneto-optics is a very common yet powerful tool for studying magnetic domain configurations in the solid-state magnetism community. However, magneto-optics has its roots way back to the times of Michael Faraday, who, in 1846, conducted an experiment in which he saw that linearly polarized light changed its polarization plane after passing through a glass rod (with magnetic particles) upon which a magnetic field was applied. Another very similar phenomenon had not waited for discovery for too long. In 1875, John Kerr observed the same, yet weaker, behavior after reflection of the polarized light on the surface of a polished magnet. Today, the two effects are known as the Faraday and Kerr effects, respectively, and are the most widely used magneto-optical effects. As the Faraday effect is most accessible only in transparent materials, the magneto-optical Kerr effect has become more relevant in opaque specimens (e.g., metallic films and multilayers). A partial drawback of the Kerr is that it is a relatively weak effect.

Furthermore, only bulk specimens with excellent surface treatment could have been studied by the Kerr effect. These limitations were dramatically reduced by the development of computers and digital processing, mainly by introducing the digital image difference technique, which allowed to subtract a non-magnetic background signal from the magnetic one and thus rapidly increased the magneto-optical contrast level. Even though the Kerr effect has been most relevant for the research and development of magnetic materials and phenomena, it also had an important period in the consumer market. The magneto-optical recording discs used as a digital storage medium were introduced in 1983 and they held the metaphorical torch for some time; however, in the late 2000s, they fell into disuse as the development of compact discs and digital video discs took over the lead.

Over the course of time, scientists wanted to understand magneto-optical effects more in-depth and were able to discover additional effects that are manifested in reflection. The Kerr effect is an effect linear in magnetization, which means that the sense of polarization rotation reverts if the magnetization is inverted. However, a quadratic effect in magnetization was found, now called the *Voigt effect*. Most importantly for this thesis, an effect containing a magnetization-gradient dependency was discovered in 1990, an effect now known as the *gradient effect*, sometimes called the *Schäfer-Hubert effect*. Each of these magneto-optical effects displays its characteristic symmetry with respect to polarization and illumination geometry, and has their own set of advantages.

The following section will provide a more detailed description of magneto-optical effects. A more phenomenological explanation of Kerr effects will be presented, on which an overview of the most notable gradient effect studies will connect.

3.1. The dielectric permittivity tensor

First, let us assume an electromagnetic wave propagating in vacuum toward the yet unspecified medium. The incident electric field component $\vec{E}$ will induce the dielectric displacement

vector $\vec{D}$ within the medium. From material relations, we write that both electric fields are, in general, connected via the dielectric permittivity tensor

$$\vec{D} = \epsilon_0 \hat{\epsilon} \vec{E}, \tag{3.1}$$

where ϵ_0 is the permittivity of free space. Similarly, this can be done for the magnetic fields, where the incident $\vec{B}$-field, written as $\mu_0 \vec{H}$, induces a magnetic field in the medium. This relation is expressed as

$$\vec{B} = \mu_0 \hat{\mu} \vec{H}, \tag{3.2}$$

where μ_0 is the permeability of free space. Nevertheless, we usually assume $\hat{\mu}$ to be a unity tensor. The usual argument is that it is unitary only in a non-magnetic matter; however, Landau and Lifshitz have shown that it stays unitary at optical and near-infrared frequencies even in magnetic matter [17]. Thus we concern ourselves only with the dielectric permittivity tensor $\hat{\epsilon}$.

Generally, we can use Maxwell's equations to derive the wave equation for $\vec{E}$, which after assuming a solution in the form of plane waves $\vec{E}(\vec{r}, t) = \vec{E_0} \exp\Big[i(\vec{k} \cdot \vec{r} - \omega t)\Big]$, for a component E_j acquires the form

$$-k_j \sum_i k_i \cdot E_i / k_0^2 + n^2 E_j + \sum_i \epsilon_{ij} \cdot E_i = 0. \tag{3.3}$$

In which $\vec{r}$, t are space and time coordinates, and ω, $\vec{k}$ are the corresponding temporal frequency and wave vector, respectively. Lastly, $n = k^2/k_0^2$ is the refractive index, and k_0 is the wave vector in vacuum. The determinant has to vanish to find solutions for the set of those linear equations of E_i. Furthermore, this gives us a solution for the refractive index n_i, corresponding to E_i, as a function of the dielectric tensor components.

Further, we specify what form the permittivity tensor takes in different materials. Firstly, in the case of a non-magnetic crystal, the permittivity can be described as [10]

$$\hat{\epsilon}_{\text{cryst}} = \hat{\epsilon}^0 + \hat{\epsilon}_{\text{br}} + \hat{\epsilon}_{\text{oa}}, \; \hat{\epsilon}^0 = \begin{pmatrix} \epsilon_{\text{iso}} & 0 & 0 \\ 0 & \epsilon_{\text{iso}} & 0 \\ 0 & 0 & \epsilon_{\text{iso}} \end{pmatrix}, \tag{3.4}$$

The listed components stand for the diagonal isotropic tensor $\epsilon^0_{ii} = \epsilon_{\text{iso}}$, where $\epsilon_{\text{iso}} = n^2$ is the regular isotropic permittivity, crystalline birefringence $\hat{\epsilon}_{\text{br}}$, and optical activity $\hat{\epsilon}_{\text{oa}}$. If only the diagonal components of the permittivity tensor are present, the $\vec{D}$ vector keeps the same orientation as the incident $\vec{E}$ vector. However, if the tensor has non-zero off-diagonal components, the light interacts with the matter by rotating the $\vec{E}$ vector polarization plane.

In addition to the $\hat{\epsilon}^0$ tensor, it has been found experimentally that light interacts with matter differently if we apply some magnetic field $\vec{B}$, which implies that the $\vec{B}$-field has to be somehow incorporated in the total permittivity tensor $\hat{\epsilon}_{\text{tot}}$. Nevertheless, it has been found that the permittivity tensor of ferromagnetic materials rather depends on the material's magnetization $\vec{M}$ than on the $\vec{B}$-field [73]. In metallic materials, we can usually neglect crystalline birefringence and optical activity. Hence, for the total permittivity tensor, we can write

$$\hat{\epsilon}_{\text{tot}} = \hat{\epsilon}^0 + \Delta\hat{\epsilon}(\vec{M}), \tag{3.5}$$

where $\Delta\hat{\epsilon}(\vec{M})$ is the $\vec{M}$-dependent permittivity tensor, which is usually very subtle compared to $\hat{\epsilon}^0$, hence $\Delta\epsilon_{ij}(\vec{M}) << \epsilon^0_{ij}$.

With no harm in generality, we can split $\Delta\hat{\epsilon}$ into the Hermitian component $\Delta\epsilon_{ij}^{H}$, with $(\Delta\epsilon_{ij}^{H})^{\star} = \Delta\epsilon_{ji}^{H}$ and '$\star$' denoting the complex conjugate, and the anti-Hermitian $\Delta\epsilon_{ij}^{A}$ components, with $(\Delta\epsilon_{ij}^{A})^{\star} = -\Delta\epsilon_{ji}^{A}$, which are both complex. Moreover, $\Delta\hat{\epsilon}$ abides by the so-called Onsager relation [17]

$$\Delta\epsilon_{ij}(\vec{M}) = \Delta\epsilon_{ji}(-\vec{M}). \tag{3.6}$$

Given that the $\Delta\hat{\epsilon}(\vec{M})$ is rather weak, we can expand it into a power series of $\vec{M}$ while neglecting higher than quadratic terms. We can find power series coefficients and use them to get both linear and quadratic permittivity tensors for cubic symmetry [74]. Finally, the tensors can be rewritten compactly as [10]

$$\hat{\epsilon} = \hat{\epsilon}^{\mathrm{K}} + \hat{\epsilon}^{\mathrm{V}} = \epsilon_{\mathrm{iso}} \begin{pmatrix} 1 & -iQ_V m_3 & iQ_V m_2 \\ iQ_V m_3 & 1 & -iQ_V m_1 \\ -iQ_V m_2 & iQ_V m_1 & 1 \end{pmatrix} + \begin{pmatrix} B_1 m_1^2 & B_2 m_1 m_2 & B_2 m_1 m_3 \\ B_2 m_1 m_2 & B_1 m_2^2 & B_2 m_2 m_3 \\ B_2 m_1 m_3 & B_2 m_2 m_3 & B_1 m_3^2 \end{pmatrix} \tag{3.7}$$

The tensor $\hat{\epsilon}^{\mathrm{K}}$ linear in $\vec{m}$ corresponds to the Kerr effect, where m_i are the magnetization $\vec{M}$ cosines, and Q_V is a material parameter – Voigt constant – denoting the strength of the Kerr effect. The quadratic-magnetization tensor $\hat{\epsilon}^{\mathrm{V}}$ is the Voigt effect, where B_1 and B_2 are corresponding material parameters. A more thorough derivation of the two magneto-optical effects' permittivity tensors may be found in Ref. 75.

3.2. Magneto-optical effects' geometries

Now that we have a precise form of the magnetization-dependent permittivity tensor, we can solve the system of equations (3.3). Essentially, it is a highly complex mathematical problem if attempted to solve for the general form of (3.7). Therefore, we make some assumptions about the experiment geometry to simplify the calculations.

The simplest case is the one in which we consider a general linearly polarized light at normal incidence, thus $|\vec{k}| = k_z = k_3$ and perpendicular magnetization $|\vec{m}| = m_z = m_3 = 1$. This geometry is referred to as the *polar Kerr effect*. Solving the set of equations (3.3) with simplified $\hat{\epsilon}^{\mathrm{K}}$ leaves us with allowed modes in the medium, described by the wave vector [10]

$$k_z \approx \pm k_0 \sqrt{\epsilon_{\mathrm{iso}}}(1 \pm Q_V/2). \tag{3.8}$$

The approximate result was obtained after assuming $|Q_V| << 1$. The further solution gives us

$$E_y^0 = \pm i E_x^0, \tag{3.9}$$

where $\pm$ signs correspond to the *left-* and *right-circularly polarized light*. The first $\pm$ signs in the equation (3.8) represent forward and backward propagating waves. From (3.8), we can explicitly extract the modes' corresponding refractive indices as $k_z = nk_0$, hence

$$n_{\pm} = \sqrt{\epsilon_{iso}}(1 \pm Q_V/2). \tag{3.10}$$

In the end, we obtain four light propagation modes in the medium: two forward and two backward propagating and both propagation directions have the two circular polarization modes. These eventually account for light reflection and refraction in the medium.

Notably, the two circular polarizations' refractive indices will differ if the medium is magnetic (i.e., $Q_V \neq 0$). Furthermore, if the medium is absorptive, $n_\pm$ will be complex numbers $n_\pm = n'_\pm + in''_\pm$. This means the two polarizations will have different phase velocities $v_\pm = c/n_\pm$, leading to an optical path difference $d(n_+ - n_-)$ while travelling the distance d. Eventually, as the two modes leave the medium, they combine back to the linearly polarized state; however, the plane of polarization will be rotated due to the modes' phase retardation. In general, the modes will also be absorbed at different rates, leading to slight elliptical polarization. Assuming incident light polarized along the x-axis, we can calculate the polarization rotation θ upon reflection as $\theta \approx tan(\theta) = E_y^{\text{refl}}/E_x^{\text{refl}}$ since the polarization rotations are small. The rotation angle is complex (in absorbing media) and is known as *complex Kerr rotation* $\theta_K^C = \theta_K + i\xi_K$, where the real part θ_K describes the actual polarization rotation angle and the imaginary part ξ_K the ellipticity. In the polar Kerr effect geometry, the complex Kerr rotation takes the form [10]

$$\theta_K^C = -i\frac{\bar{n}Q_V}{1-\bar{n}^2}, \tag{3.11}$$

where $\bar{n} = (n_+ + n_-)/2$.

So far, we have clarified only the normal incidence and out-of-plane magnetization case. Similarly, we could calculate the eigenmodes for oblique incidence and in-plane magnetization. Within this specification, we can distinguish between two geometries. In the first geometry, the in-plane magnetization lies in the plane of incidence (denoted by the incident light and surface normal); this geometry is known as the *longitudinal Kerr effect*. The other geometry applies when the magnetization is perpendicular to the plane of incidence, hence called the *transversal Kerr effect*. Eventually, these two Kerr effects are phenomenologically identical to the polar Kerr effect. Even though it is possible to obtain analytically the corresponding modes, refractive indices and thus complex Kerr angles, it is much less clear than for the polar Kerr effect. For more detailed and structured derivations we refer the reader, for instance, to the derivations done by Višňovský [76].

Another way of viewing the Kerr effect more qualitatively is to take the permittivity tensor, insert it into the dielectric law (3.1) and express the terms in vectorial form. The dielectric displacement is then

$$\vec{D} = \epsilon_0\epsilon_{iso}[\vec{E} + iQ_V(\vec{m} \times \vec{E})]. \tag{3.12}$$

This formulation is called the *Lorentz concept*, where the equation's right-side vectors act as Lorentz force vectors displacing electrons at the surface. The displacement vector may be considered a field corresponding to the oscillatory motion of those affected electrons. The incident polarized-light $\vec{E}$ vector is a source of electrons' primary motion so that the electrons will oscillate along the light polarization plane. However, due to the presence of magnetization, a secondary electron motion corresponding to $-(\vec{m} \times \vec{E})$ will contribute to transverse oscillations. As electric dipoles, the oscillating electrons then radiate polarized light that is rotated with respect to the incident polarization. Which, in the end, reveals the gyrotropic nature of Kerr effects. In Fig. (3.1) the Lorentz concept is depicted for different experiment scenarios.

Typically, we can use the dielectric displacement to predict the magnetization dependence of the reflected light. For instance, let us assume the incident light polarized along the x-axis $\vec{E}^{\text{inc}} = (E_x^{\text{inc}}, 0, 0)$. The E_x^{inc} excites the Lorentzian motion of electrons, creating the dielectric displacement field $\vec{D}$, which in turn radiates the slightly rotated polarization $\vec{E}^{\text{refl}}$. However, since the analyzer is in crossed position, only E_y^{refl} will reach to the detector, resulting

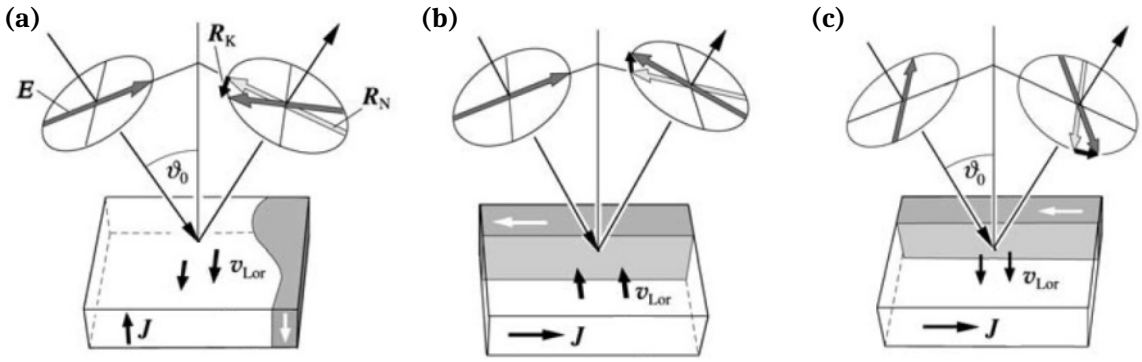

Figure 3.1.: Illustration of the Lorentz concept, the induction of secondary motion of electrons due to the presence of magnetization ($\vec{J}$) and incident polarization in a) polar Kerr effect mode (out-of-plane magnetization), b) longitudinal Kerr effect mode (in-plane magnetization) and incident p-polarization, and c) longitudinal Kerr effect with incident s-polarization. Adapted from Ref. 9.

in intensity I_{detect}. Nevertheless, there is a direct connection between $\vec{D}$ and $\vec{E}^{\text{refl}}$; hence, $E_x^{\text{inc}} \sim D_y \sim E_y^{\text{refl}} \sim I_{\text{detect}}$.

To summarize, in polar Kerr effect geometry, the light incident propagation is normal to the surface, and only out-of-plane magnetization causes polarization rotation. Additionally, opposite domains create opposite secondary electron motions, resulting in opposite Kerr rotations. For measuring the signals related to the longitudinal Kerr effect, light incidence has to be oblique. The Kerr rotation is caused by the magnetization component lying in the plane of the light incidence. Furthermore, note that in this geometry, even out-of-plane magnetization causes a certain Kerr rotation since some normal incidence component of the wave vector of light is present. Again, it is an odd effect in magnetization; also, reversing the angle of incidence inverts in-plane magnetizations' Kerr rotations. Nevertheless, reversing the angle of incidence does not change the normal component; hence, the Kerr rotation linked to the out-of-plane magnetization component remains the same. Again, the transverse Kerr effect is present at oblique incidence; the magnetization has to be in-plane and normal to the plane of incidence.

In contrast to the other two Kerr effects, where the incident polarization could be arbitrary, for the transverse Kerr effect to cause any rotation, the incident polarization cannot be s nor p. In the case of p-polarization, the secondary electron motion coincides with the primary motion, whereas in the case of s-polarization, the whole cross product vanishes. However, any other polarization angle between the two results in light polarization rotation associated with the transverse Kerr effect, while the strongest rotation is at $45°$ with respect to the plane of incidence.

Lastly, the quadratic (Voigt) magneto-optical effect geometry is mentioned. Whereas the Kerr effect amplitude is weak compared to the regularly reflected light amplitude, the Voigt effect is even weaker. It is observable only at (near) normal incidence and in-plane magnetization [10]. Due to its quadratic nature, the opposite magnetizations cause the same polarization rotation. However, an opposite polarization rotation is caused instead by perpendicularly oriented magnetizations. Furthermore, more than perpendicular magnetizations are required for the opposite polarization rotations. The symmetry of the Voigt effect requires that the projection of the perpendicular magnetizations to the polarization plane has to be the same, meaning that the magnetizations are oriented $45°$ with respect to the incident polarization plane. On the

contrary, having one magnetization parallel and one perpendicular to the polarization plane results in the same polarization rotations.

Most commonly, Kerr effects are utilized the most in magnetic domain diagnostics within magneto-optics, arguably even among all magnetic microscopy techniques. Furthermore, they provide a direct and linear connection to the surface magnetization. The Voigt effect, on the other hand, is typically not the first choice when aiming at domain imaging, as resolving the exact magnetization configuration by its sole means can be tricky. An interesting outlook of Voigt effect microscopy is the possibility to image regions with different spin axis orientations in antiferromagnets, where magnetic imaging cannot rely on linear Kerr effects. Voigt-like microscopy measurements were already successfully conducted on antiferromagnetic oxides like NiO [77] and CoO [78]. However, it is argued that the imaging contrast here arises from optical birefringence linked to the large magnetoelasticity, which generates a an optical signal possessing the same symmetry as the Voigt effect.

Due to the linearity of Maxwell's equations, we could split the dielectric permittivity tensor into multiple contributions (crystal, birefringence) and (Kerr, Voigt) and treat them individually. In actual experiments, this separation is not so straightforward. In fact, in actual experiments, we detect the contribution of all effects at once; hence, all the diagonal and off-diagonal elements of the permittivity tensors must be considered. Nonetheless, some contributions may outweigh others, which may be caused by specific material parameters or by cleverly setting the experiment geometry to exploit the symmetries of the desired effects. Eventually, some effects thus might be "hidden" by others and cannot be observed. This was precisely the case for a new magneto-optical effect found by Schäfer and Hubert in 1990 called the magneto-optical gradient effect.

3.3. Overview of the magneto-optical gradient effect experiments in the literature

In one of the pioneering works on the magneto-optical gradient effect from 1990 [79], Schäfer and Hubert found an unexpected domain boundary contrast that appeared when the stronger signal from the nearby domains was removed. The domain signal was removed by adequately adjusting the optical components. Furthermore, they deduced that any other already known magneto-optical effect could not explain this contrast originating from domain boundaries.

The investigated material in the original paper was a SiFe crystal known to have in-plane domains with regular $90°$ DWs as well as $180°$ walls and V-lines. Once they removed the domain signal, which was especially possible when introducing the compensator, a residual contrast at boundaries was observed; see the anomalous contrast in Fig. (3.2a). The type of contrast they observed was either a black or white homogeneous line along the whole boundary, we call this contrast the *single contrast*. The structure of the V-line may suggest that the boundary contrast might have been a polar Kerr contrast from the buried out-of-plane domains. However, a decisive discovery was that this boundary contrast switched signs after azimuthally rotating the specimen by $90°$, which meant it could not be attributed to the polar Kerr effect; see Fig. (3.2b).

Further, they investigated the possibility of utilizing this single contrast to obtain the characteristic width of the DW. They compared the integrated wall contrast acquired from the single contrast with the longitudinal Kerr effect contrast. Eventually, they made this comparison in multiple materials with different wall widths and ended up with a linear dependency,

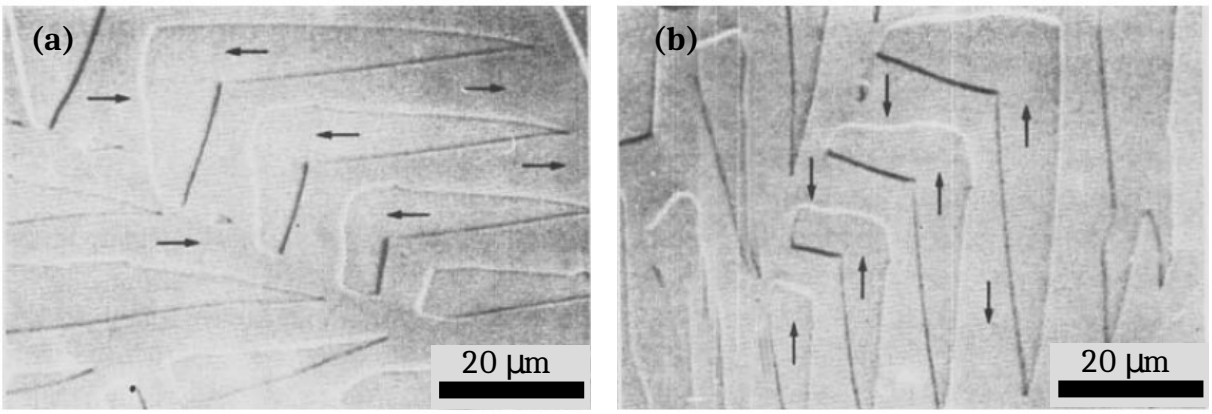

Figure 3.2.: Magneto-optical gradient effect images of V-line domains taken at perpendicular incidence, a) before, b) after sample rotation by 90°, showing the switching of the gradient effect polarity. Taken from Ref. 79.

meaning that the two integrated wall contrasts are equivalent. Thus, they could not obtain a direct estimate for the DW width below the spatial resolution, concluding that the observed effect should be called domain "boundary" instead of DW contrast.

Another key finding was acquired after observation of the same $180°$ domains with V-lines using longitudinal Kerr contrast and the boundary contrast consecutively. Since DWs in this system are relatively large (≈ 250 nm [80]), it is possible to find their chirality by the longitudinal Kerr effect at oblique incidence, as it is visible from Fig. (3.3a). The boundary contrast, measured at normal incidence, then showed only an alternating single contrast, which did not correlate to the particular wall chirality; see Fig. (3.3b). These measurements found that the observed single contrast contains no information about the DW chirality whatsoever.

Finally, Schäfer and Hubert put all the symmetries together and empirically derived the dielectric permittivity tensor, in which the boundary contrast was represented by magnetization gradient. The permittivity tensor took the form

$$\begin{aligned}\hat{\epsilon}^{\mathrm{gr}} &= \begin{pmatrix} -P(\frac{\partial m_2}{\partial x_1}+\frac{\partial m_1}{\partial x_2}) & P(\frac{\partial m_1}{\partial x_1}-\frac{\partial m_2}{\partial x_2}) & -P'(\frac{\partial m_3}{\partial x_2}+\frac{\partial m_2}{\partial x_3}) \\ P(\frac{\partial m_1}{\partial x_1}-\frac{\partial m_2}{\partial x_2}) & P(\frac{\partial m_2}{\partial x_1}+\frac{\partial m_1}{\partial x_2}) & P'(\frac{\partial m_3}{\partial x_1}+\frac{\partial m_1}{\partial x_3}) \\ -P'(\frac{\partial m_3}{\partial x_2}+\frac{\partial m_2}{\partial x_3}) & P'(\frac{\partial m_3}{\partial x_1}+\frac{\partial m_1}{\partial x_3}) & 0 \end{pmatrix} = \\ &= \begin{pmatrix} -2PS_{21} & P(S_{11}-S_{22}) & -2P'S_{32} \\ P(S_{11}-S_{22}) & 2PS_{21} & 2P'S_{31} \\ -2P'S_{32} & 2P'S_{31} & 0 \end{pmatrix}\end{aligned} \tag{3.13}$$

where P is a material parameter denoting the strength of the effect, whereas P' is introduced as an additional material parameter whose relevance needed to be tested; possibly, they could coincide (i.e., $P = P'$), and S_{ij} would therefore turn into a symmetric gradient tensor defined as $S_{ij} = 1/2(\partial m_i/\partial x_j + \partial m_j/\partial x_i)$.

For completeness, the presence of this gradient effect was also briefly discussed for the perpendicularly magnetized system. Using the polar Kerr effect, the authors observed a maze-like domain pattern in a TbFeCo film. Again, they compared it with the same domain state imaged under oblique illumination after suppressing the Kerr effect, leaving only the alternating black and white single contrast at the boundaries; see Fig. (3.2c). This led to another outcome: the gradient effect depends on both the planar and polar magnetization gradients [79].

Intriguingly enough, they also observed that the boundary contrast does not only have a form of a single contrast [79]. At some conditions, a dipolar contrast may appear in which

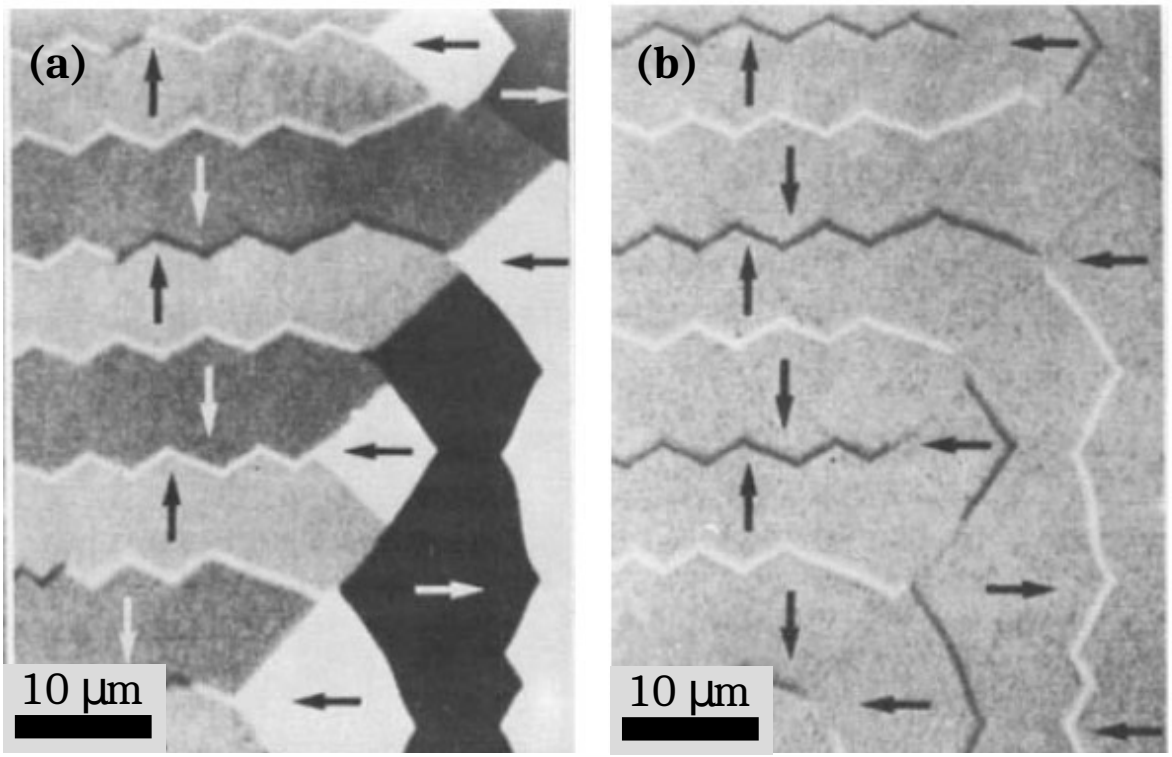

Figure 3.3.: V-line domain images acquired under a) oblique incidence – showing dominantly the Kerr effect, and b) normal incidence – primarily showing the gradient effect signal and its independence on the domain wall chirality. Taken from Ref. 79.

the boundary contrast changes sign across the transition between domains. We refer to this contrast as the *double contrast*. The single and double contrasts could appear simultaneously at certain boundaries, making them challenging to analyze separately. Ultimately, the authors decided to focus solely on the single contrast, as the double contrast usually appeared to be much weaker.

However, a more in-depth investigation of the gradient effect-related dielectric tensor was necessary to describe the difference between the gradient effect contrast at different experiment geometries, including the angle of incidence. This issue was addressed in Ref. 81, where a similar approach was applied, as in the original work [79]. The new derivation was again semi-empirical and included an implementation of the incident light wave vector $\vec{k}$. After a rather complicated tensor analysis, the permittivity tensor was obtained. However, its form is relatively hard to grasp; therefore, we instead write the corresponding dielectric displacement component D_1

$$\begin{aligned} D_1^{\mathrm{gr}} =& P\{2[S_{31}k_2 - S_{21}k_3]E_1 \\ &+ [-S_{31}k_1 + S_{32}k_2 + (S_{11} - S_{22})k_3]E_2 \\ &+ [S_{21}k_1 + (S_{33} - S_{11})k_2 - S_{32}k_3]E_3\}, \end{aligned} \tag{3.14}$$

whereas the other dielectric displacement components can be obtained via cyclic permutation.

By comparing this dielectric law to the one previously derived, we can spot that the permittivity in (3.13), under condition $P = P'$, can be considered the special case of (3.14) with

$\vec{k} = (0, 0, k_3)$. Note that the present wave vector is normalized; thus, its components denote the direction cosines.

In the end, the authors admit that the proposed dielectric law (3.14) is the simplest possible description of the gradient effect as it contains only a single material parameter and is partially based on experiments. Even though it was possible to derive such a dielectric law, the physical origin of the gradient effect still remained yet to be discovered; therefore, more complex relations could not be excluded.

Eventually, an explanation in the form of the diffraction theory was proposed. In Ref. 82, Kamberský used a systematic diffraction of polarized light waves caused by magnetization gradients and was able to derive the symmetries of the experimentally measured effects. The derived symmetries were in agreement with the dielectric tensor model (3.14); moreover, this approach allowed for a more complex and detailed analysis of the gradient effect. More studies on this magneto-optical diffraction analysis were conducted, incorporating depth sensitivity and interference effects; among the most prominent are the works in Refs. 83–86.

Another vital study [80] in this series of rather experimentally focused papers investigated the often weak double contrast in more detail than the previous works. In this study, the authors again observe FeSi crystal with in-plane flux closure patterns with $180°$ Néel walls.

The procedure was to characterize a domain pattern using the longitudinal Kerr effect (i.e., oblique incidence). Since the surface DW widths were, again, relatively large ($\approx$ 270 nm), they could identify the walls' chiralities. Afterwards, they imaged the same domain state under perpendicular incidence. Thus they were able to see the gradient effect. However, they realized that the Voigt effect could be seen under the perpendicular illumination. With the knowledge of the magnetization profile along the Néel wall, they could analytically obtain the dielectric displacement of the Voigt and the gradient effects. The authors found that both effects correspond to a dipolar profile leading to the double contrast. Since the two effects have different symmetries, the double contrast's polarity differs depending on the chirality of the wall. This eventually means that depending on the chirality of the DW, the double contrasts may either add or subtract. Furthermore, the authors eventually succeeded in seeing this complete double contrast subtraction in alternating $180°$ domains, as seen in Fig. (3.4a).

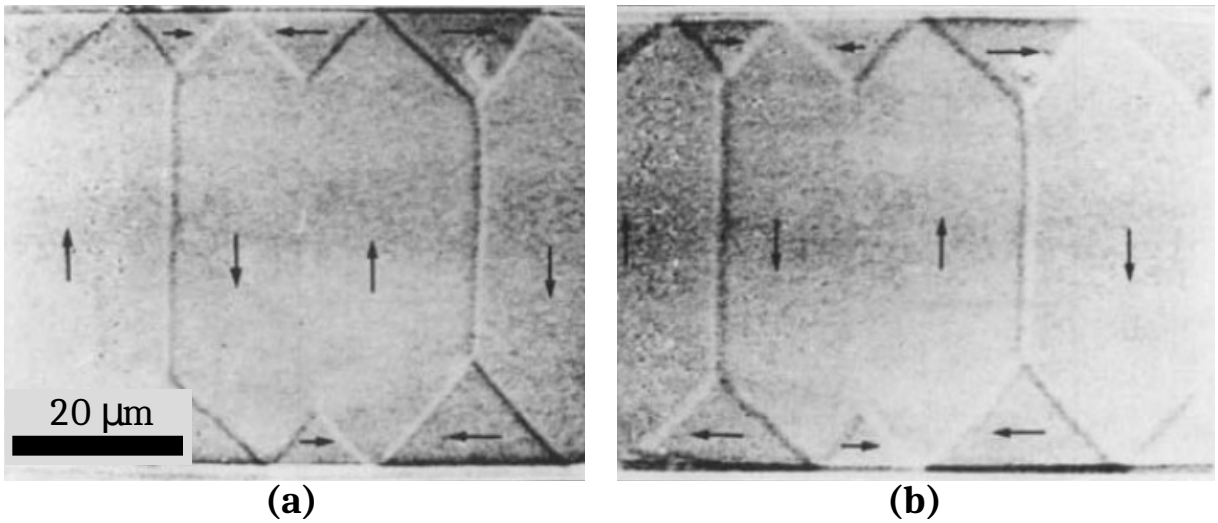

Figure 3.4.: Addition and subtraction of the gradient and Voigt effect contributions at the $180°$ domain boundary in a) an in-focus image, b) defocused image, showing no switching of contrast due to diffractive effects [80].

Further, the authors discuss the diffractive character of the gradient effect shortly by comparing an image taken at perpendicular incidence focused precisely at the surface with a slightly off-focus image. Diffraction effects could possibly change the boundary contrast polarity; however, they reported only a broadening of the boundary contrast, not its polarity switching. For comparison, see the in-focus image in Fig. (3.4a) and the defocused image in Fig. (3.4b).

One of the most recent studies on the gradient effect finally demonstrated experimentally how the boundary contrast behaves in case of the absence of the subsurface domains in V-line domains [20]. They fabricated a system with stripe-like head-on domains by magnetically coupling a thin layer of a magnetically soft NiFe film with an antiferromagnetic IrMn layer on top. The exchange bias field from the coupled antiferromagnetic layer forces the otherwise highly energetically unfavorable head-on arrangement of domains. The observed gradient effect then could be attributed only to in-plane gradients. The authors report an agreement of a theoretical prediction by the diffractive theory with the corresponding experiments.

All the pioneering works devoted to the gradient effect observation [20, 79, 81] claim that the magnetization difference between neighboring domains is the most dominant contribution of the boundary contrast, not the internal DW structure itself. However, the study conducted in Ref. 80 focusing on the weak residual double contrast showed that the boundary contrast corresponding to the internal DW structure could be explained by the gradient effect.

Even though predominantly in-plane domains were investigated using the gradient effect in the relevant literature, out-of-plane domain investigations need to be brought into more detail. Furthermore, state-of-the-art research focused mainly on the dominant single contrast, and the weaker double contrast was mostly disregarded. The following chapters focus on filling those experimental gaps in out-of-plane magnetized systems and analyzing the residual double contrast.

4. Sample fabrication and characterization

In regard to sample fabrication, our primary goal was to prepare magnetic multilayers with PMA. Additionally, we aimed at having preferably large (several tens of μm) and well-separated bubble domains so that the domain boundaries are sufficiently distant and thus recognizable. In some multilayer designs, we implemented heavy metal layers (e.g., Pt) asymmetrically with respect to magnetic layers to induce the DMI and, thus, stabilize Néel walls. We also followed the assumption of having a heavy metal layer symmetrically placed on both sides of a ferromagnetic layer, aiming toward canceling the DMI and the sample resulting into achiral Bloch walls. A most commonly practiced method to confirm the presence of the DMI indirectly is the method utilizing an asymmetrical bubble domain expansion (see Fig. (1.8)).

4.1. Experimental methods

The samples were fabricated using a direct-current magnetron sputtering system (BESTEC), with a base pressure better than 5×10^{-8} mbar. All depositions were performed at room temperature and using an Ar pressure of 2.5×10^{-3} mbar (flow 30 sccm). Initially, we used a quartz crystal microbalance to obtain deposition rates of individual sputtered materials. We deposited single films of individual materials of certain nominal thicknesses using the specific deposition rates. The exact deposition rate was then calculated by measuring the thickness of the deposited calibration films via X-ray reflectometry in a Rigaku SmartLab 9kW X-ray diffractometer.

Further, we used a Kerr microscope from Evico magnetics with a $50\times$ magnification objective for magneto-optical imaging and magnetic hysteresis loop characterization. The microscope utilizes a set of eight white light-emitting diodes organized into a cross to access oblique illumination from all four directions. To achieve normal incidence illumination, we manually moved one of the light sources to the center of the back focal plane. Further, for external out-of-plane magnetic fields, we used a custom electromagnet providing applied fields up to ± 100 mT and placed on top of a custom-adapted dual-axis goniometer, which is crucial for correcting slight sample tilts and achieving a homogeneous objective focus over an extended field of view (~ 200 μm).

4.2. Magnetic characterization

We deposited the layered systems on either Si or glass (fused silica) 5×5 mm^2 substrates. The multilayer structure of the samples that were used in this thesis are

1. **Co/Gd**: Si(subs.)/Pt(3)/Co(1)/Gd(3)/Pt(2)
2. **[Co/Pt]**: glass(subs.)/Ta(5)/Pt(3)/$[\text{Co}(0.4)/\text{Pt}(0.7)]_{\times 3}$/Pt(2.3)
3. **[Co/Ni]**: glass(subs.)/Ta(5)/Pt(3)/$[\text{Co}(0.2)/\text{Ni}(0.6)]_{\times 2}$/Co(0.5)/Pt(2)
4. **[Fe/Gd]**: Si(subs.)/Ta(3)/$[\text{Fe}(0.58)/\text{Gd}(0.48)]_{\times 20}$/Ta(6)

with the layers' thicknesses in nm, together with a label on how we will further refer to the individual samples in the thesis.

After fabrication, PMA was tested employing Kerr microscopy, by which we characterized individual samples by measuring hysteresis loops in an out-of-plane magnetic field. Since all the hysteresis loops had a square-like shape, PMA was confirmed in all samples. See the corresponding hysteresis loops plotted in Fig. (4.1).

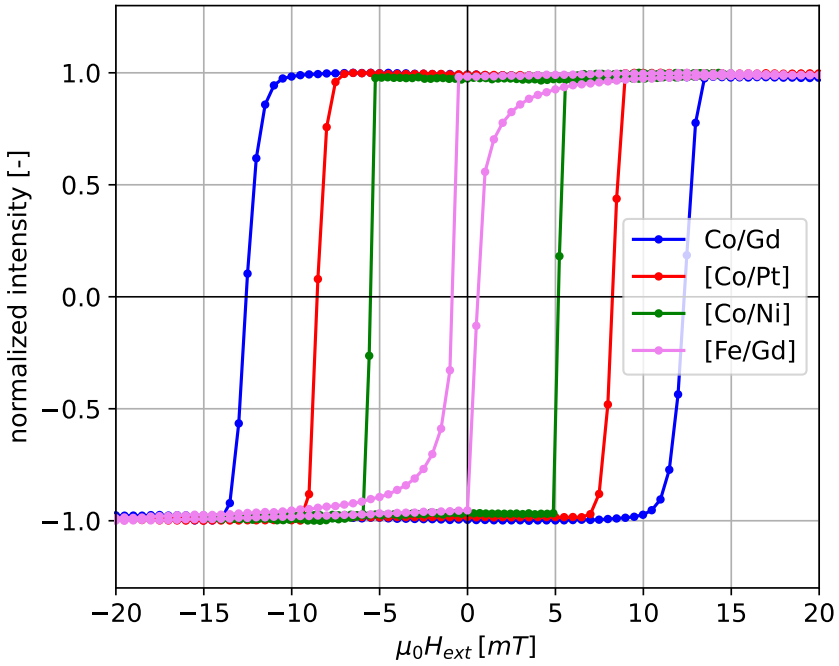

Figure 4.1.: Hysteresis loops measured in our-of-plane external magnetic field in Kerr microscopy. Their square-like appearance confirms that all samples have PMA.

4.3. Domain wall type determination

In the next step, we meant to characterize the DW type present in the individual samples. First, we analyzed the Co/Gd sample, which is a synthetic ferrimagnet, using the bubble expansion method. Even though typical domains in this sample are reasonably isolated (see Fig. (4.2)a), we saw that applying the crossed external magnetic field connected neighboring domains and thus measuring asymmetric bubble expansion was not plausible. However, Co/Gd layered systems are well-known to have strong DMI at the interface with Pt [87]; thus, we expected the presence of Néel walls.

Afterwards, we characterized the DW type of the [Co/Pt] sample. We performed the bubble expansion experiments and found that in this sample, the bubble expanded very symmetrically. The opposite sides of the bubble propagate at almost exactly the same velocities as the bubble domain elongates along the in-plane field direction. See a graph plotting the bubble displacement on the propagation angle over time and domain images taken in the process in Fig. (4.3). Hence, we assumed the DW in this sample to be of Bloch type, as we would suppose from its symmetrical magnet-heavy metal stacking.

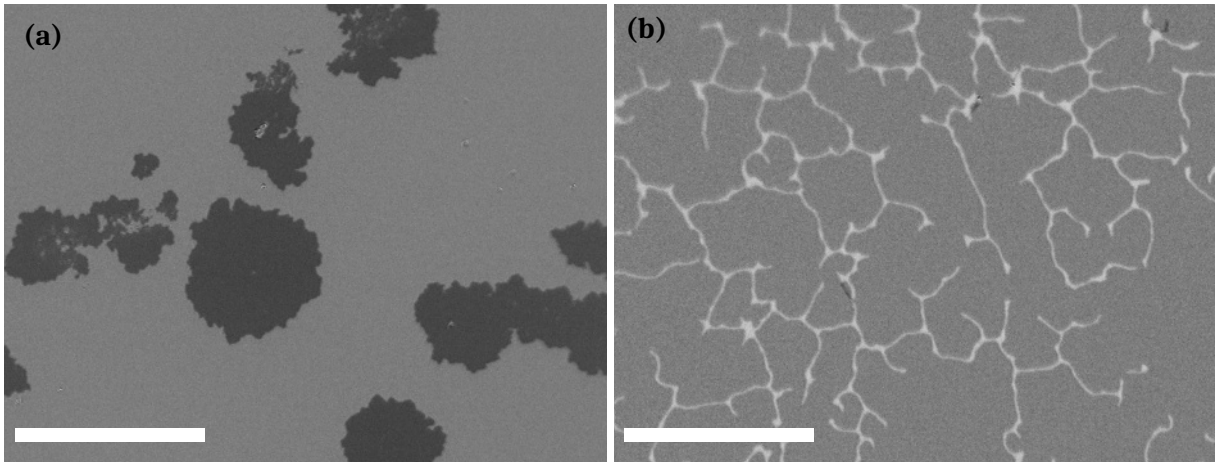

Figure 4.2.: a) Typical bubble domains in the Co/Gd sample and b) the so-called Voronoi networks in the [Co/Ni] sample appearing due to strong magnetic charges at domain walls. The scale bar corresponds to 50 μm.

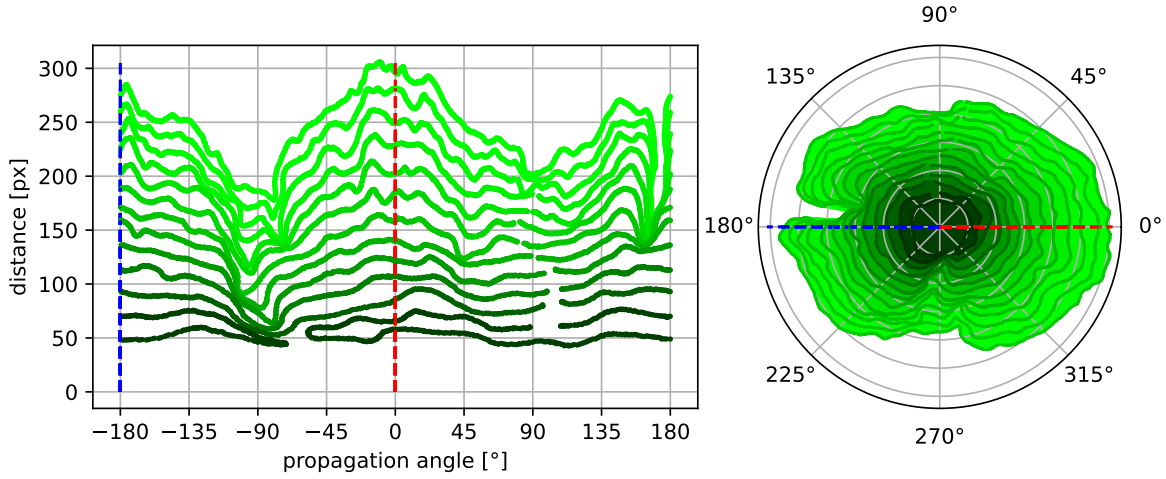

Figure 4.3.: Asymmetrical bubble domain expansion experiment done in the [Co/Pt] sample taken at 12 mT out-of-plane and 100 mT in-plane external magnetic field. Graph on the left shows the dependence of the bubble displacement on the propagation angle with respect to the domain center, while plot on right shows corresponding domain images. Brighter color represents the bubble expansion development over time.

The analysis of the DW structure of [Co/Ni] was rather straightforward. We have not measured the bubble expansions; instead, we saw that the domains in this sample form structures reminding of “Voronoi networks”. Typically, two bubble-like magnetic domains with the same magnetization orientation merge as they come into contact at the end ”during expansion”. However, it can happen that as two bubble domains approach, they avoid merging and form a gap between them. The system of these gaps is known as the Voronoi networks; see Fig. (4.2b). Furthermore, they appear because the present walls are of Néel type with the same chi-

rality; hence, as the two opposing Néel walls come near, the strong dipolar fields repel. And therefore we deduced that this system has Néel walls.

Nevertheless, since so far, our conclusions about the types of walls in our samples were acquired from indirect methods, we wanted to confirm these ideas using a direct method, like imaging. A technique with great precision that was available to us is L-TEM. We deposited the same multilayer structures on commercially available SiN membranes (30 nm thickness). Using the methodology described in [65], we accurately determined the DW types. We found that, unfortunately, we could not obtain any magnetic signal from the DWs of the Co/Gd sample; the reason might be that the total magnetic field was too small since Co/Gd is a ferrimagnet. In the second multilayer sample, [Co/Pt], we eventually saw a magnetic contrast. In contrast to our assumptions, the L-TEM measurements revealed that the DWs in this sample were Néel type; see the acquired images in Fig. (4.4a), which gives rise to doubts about the reliability of the bubble expansion method to assign a wall type in case of samples with low DMI, which is already debated in the community. Lastly, we confirmed that the [Co/Ni] sample indeed has Néel walls; see the L-TEM image in Fig. (2.6b). L-TEM measurements were kindly performed by Ing. Jan Hajduček using an FEI Titan Themis 60-300 cubed TEM operated at 300 kV.

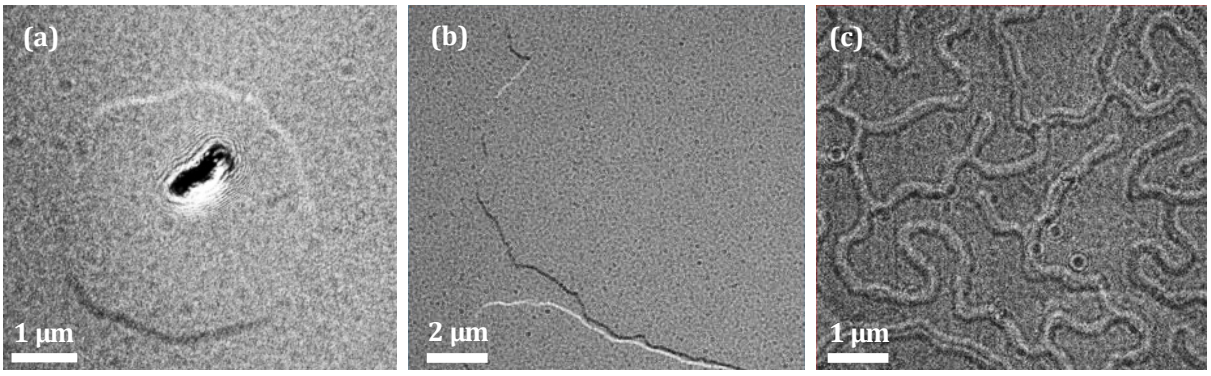

Figure 4.4.: L-TEM measurements of a) [Co/Pt], b) [Co/Ni], and c) [Fe/Gd] showing that only [Fe/Gd] has Bloch walls, while [Co/Pt] and [Co/Ni] have Néel walls.

As a result, we ended up with all samples having Néel walls. Further, we used the [Fe/Gd] sample, kindly provided by Dr. Iryna Lukiienko. From L-TEM measurements, we knew that the sample possesses Bloch walls; see the L-TEM images in Fig. (4.4c). Nevertheless, a major drawback of this sample was its extremely low coercivity, meaning that domains formed maze-like structures. Furthermore, the domains were relatively unstable due to thermal fluctuations, meaning that they were displaced by the order of micrometers in seconds.

Later in the thesis, we perform simulations of the magneto-optical gradient effect and compare it to measurements. For the simulations, we need to know the optical properties of the materials used in the fabricated samples, such as the refractive index n and Voigt constant Q_V; see Table (A.1) in Appendix A for the employed optical constant values.

5. Magneto-optical gradient effect imaging and simulation

5.1. Can magnetic domain walls be imaged via the longitudinal Kerr effect?

The longitudinal Kerr effect is sensitive to in-plane magnetization components; thus, naturally, a question arises: is it possible to use it for imaging the internal structure of a magnetic DW?

Nowadays, DW imaging may be considered a relatively common practice in in-plane magnetized systems. By aligning the plane of light incidence perpendicularly to the wall axis, the domain contrast vanishes, and it is possible to retrieve the wall type and its chirality. Such imaging was heavily utilized in [20, 79–81]. However, a mere change of plane of incidence does not suffice to remove the polar Kerr signal. Therefore, we have to use other means to get information about the in-plane magnetization component at the DW.

Typically, in magneto-optical microscopy, we detect multiple magneto-optical effects simultaneously. For instance, looking more closely into the classical longitudinal Kerr effect, we find that it is sensitive to the in-plane as well as the out-of-plane magnetization component. Because we usually work with strictly in-plane or out-of-plane magnetized systems, this duality does not pose too much of a difficulty. However, if we want to observe the in-plane magnetization within the DW, we must separate the two contributions. In principle, separating the two Kerr effects is relatively straightforward. We take advantage of the fact that the longitudinal Kerr effect switches sign with the inversion of the angle of incidence, whereas the polar Kerr effect sign remains the same. Then, we can extract the so-called pure longitudinal Kerr effect by taking two images (I_1 and I_2) of the same domain state upon the angle of incidence inversion and digitally subtracting them.

We performed this pure longitudinal Kerr effect imaging with the plane of incidence along the vertical axis on an out-of-plane bubble domain stabilized for the [Co/Pt], and we found that the contrast, indeed, reminded a type of signal corresponding to the in-plane magnetization at the site of the DW; see Fig. (5.1a). However, we found that the objective was incorrectly focused slightly above the surface. After changing the focus slightly below the surface, we obtained somewhat puzzling results. We saw that the polarity of contrast was reversed, and, moreover, an additional fairly dim contrast appeared at the bubble edges; see Fig. (5.1b). By adjusting the focusing height accordingly, we found a sweet spot where the polarity-inverting contrast vanished utterly, and we saw a black-white signal on both sides of the bubble; see Fig. (5.1c). A similar wave-like magneto-optical signal at the domain boundary has been obtained in [88], where they studied this activity by means of magneto-optical diffraction theory simulations via Fourier optics.

The dependence on focusing height and the unexpected black-white contrast occurrence could not be attributed to the longitudinal Kerr effect. This eventually means that there has to be another magneto-optical effect dominating over the Kerr effect. Our hypothesis is that given the diffractive character of the phenomenon, the dominant effect we observed was the magneto-optical gradient effect, which is diffractive in nature.

The following section discusses the theoretical background behind the manifestation of the gradient effect in perpendicularly magnetized bubble domains, which will be followed by practical implications for the observations under different experimental geometries.

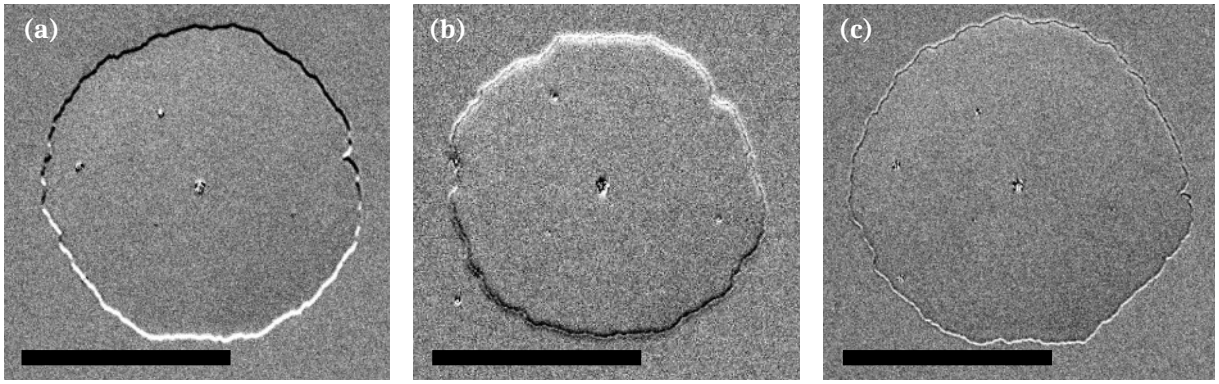

Focus **above** surface | Focus **below** surface | Focus **on** surface

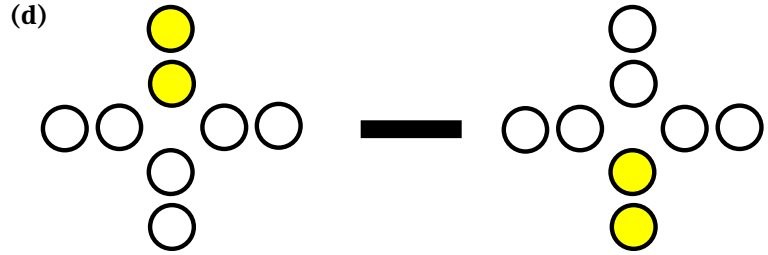

Figure 5.1.: Images taken in the pure longitudinal Kerr effect geometry (vertical sensitivity) for a bubble domain in the [Co/Pt] sample, with the illumination shown schematically in d). The boundary contrast shown with a) slight focus above the surface, b) slight focus below the surface, c) focus on surface. The scale bar is 50μm.

5.2. Gradient effect dielectric displacement in out-of-plane magnetic domains

We commented earlier that, in most usual cases, samples with PMA prefer to stabilize the Bloch wall. However, suppose a sample possesses sufficiently strong DMI. In that case, it is no longer energetically beneficial for magnetic moments in domain boundaries to stay in Bloch configuration, and thus the moments favor a more stable Néel wall of a particular chirality, depending on the sign of the DMI interaction. Since the two DW configurations have different internal magnetization structures, their magnetization gradients also differ, giving rise to the possibility of differentiating between them using the gradient effect.

This section will focus on utilizing the gradient effect-dielectric displacement (3.14) and how the change of inherent parameters changes the resulting image. Hence it is worthwhile to describe the equation thoroughly.

Firstly, the parameters in equation (3.14) are of two types: 1) material dependent – P, S_{ij} ($S_{ij} = 1/2(\partial m_i/\partial x_j + \partial m_j/\partial x_i)$) and 2) incident light property-dependent – k_i, E_i. The incident light properties can be easily changed and are well-known in each experimental geometry. In our case, material parameter P is not very important because it only scales the strength of the effect, and we are not interested in its absolute value; only relative intensity comparison is sufficient. However, the individual gradient tensor components S_{ij} contain information about the magnetization change. In our out-of-plane magnetized samples, the only change in magnetization occurs at domain boundaries.

Suppose a bubble domain with a Néel wall in a sample with PMA. Now, let us assume the S_{31} gradient tensor component, which we write as $S_{ij} = \frac{1}{2}(\frac{\partial m_3}{\partial x_1} + \frac{\partial m_1}{\partial x_3}) \approx \frac{1}{2}\frac{\partial m_3}{\partial x_1}$, where we omitted the dependence on the derivative of x_3 since we do not consider any magnetization change along the out-of-plane orientation. Taking the S_{31} component of the supposed bubble domain, it is clear that along the x_1-axis, the m_3 component changes such that the one side of the bubble has a positive gradient. In contrast, the opposite side has a negative gradient. Creating a crescent, i.e., single contrast, on each side of the bubble, see Fig. (5.2).

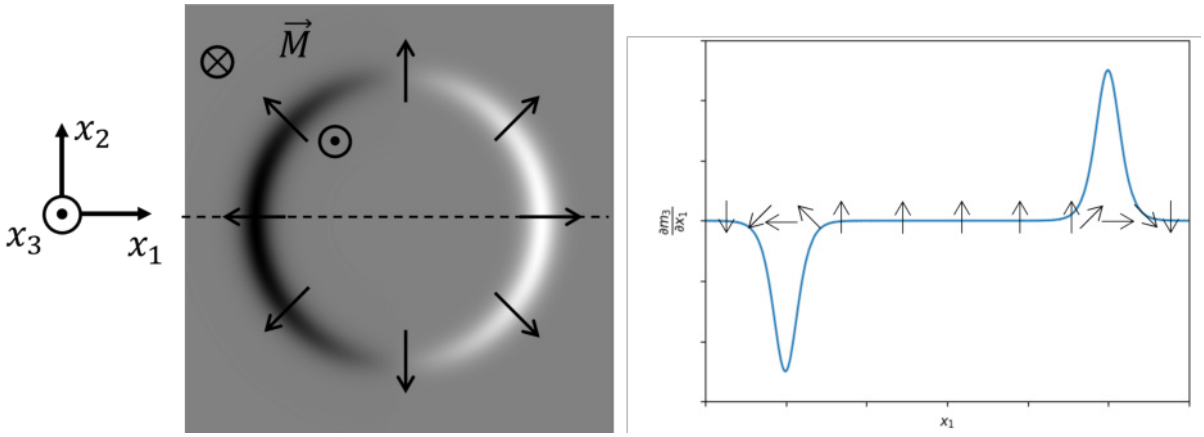

Figure 5.2.: Calculated S_{31} magnetization gradient tensor component for a bubble domain and a corresponding x_1-axis line scan.

This single contrast is present regardless of the DW type (i.e., for S_{31} same contrast appears in the Bloch and Néel walls). In the case of the S_{32} component, the arguments remain the same, and a single contrast is visible along the x_2-axis.

Another component, S_{11}, describes the change of m_1 along the x_1-axis, which for our assumed bubble domain, means that across a Néel wall, m_1 first drops and then increases (or vice versa) with increasing x_1. This scenario is shown in Fig. (5.3), where the S_{11} component causes a double contrast on each side of the bubble. Similarly, the same arguments apply to the S_{22} component, with the only difference being the change of m_2 along the x_2-axis, meaning the sensitivity axis is x_2.

In the last scenario, the gradient tensor component S_{21} combines the change of m_2 with x_1 and the change of m_1 with x_2. For the case of the Néel wall, S_{21} results in no change along the principal axes; instead, the gradient is present along the diagonals forming alternating double contrast, see Fig. (5.4).

Next, let us suppose a bubble domain with Bloch-type walls. In contrast to the Néel wall, the S_{11} component in the Bloch wall manifests itself as an alternating double contrast again along the two diagonals. The S_{22} component is essentially the same as the S_{11} component, only with the opposite sign; see the two cases in Fig. (5.5).

Lastly, the S_{21} component results in alternating double contrast along the two main axes, similar to the S_{11} and S_{22} components combined in the case of the Néel wall; see the S_{21} component shown in Fig. (5.6).

All discussed S_{ij} components' expressions and contrast influences on both Bloch and Néel walls are summarized in Fig. (5.7).

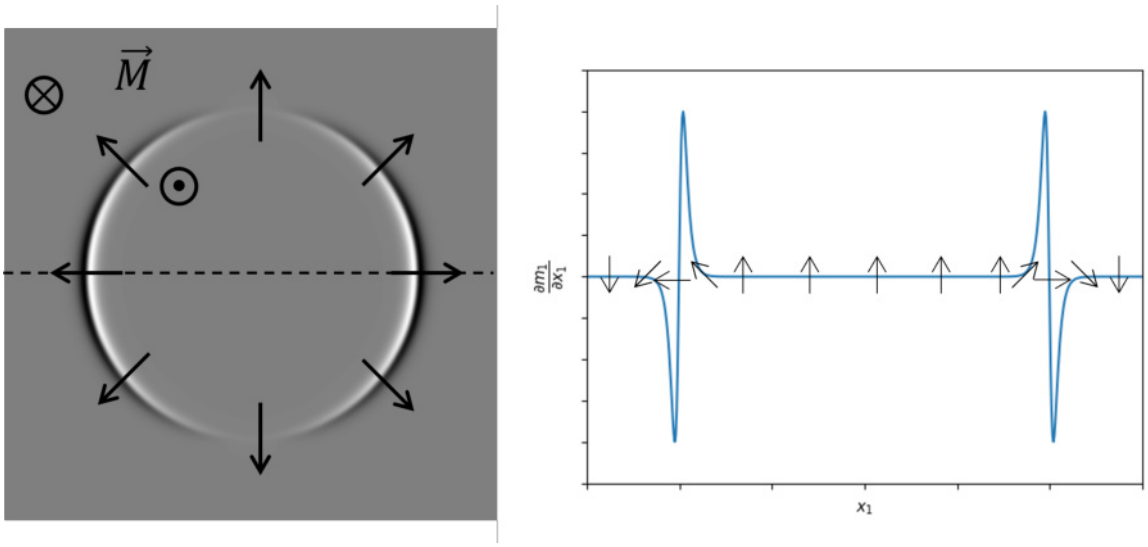

Figure 5.3.: The S_{11} magnetization gradient tensor component, calculated for Néel DW and a corresponding line scan.

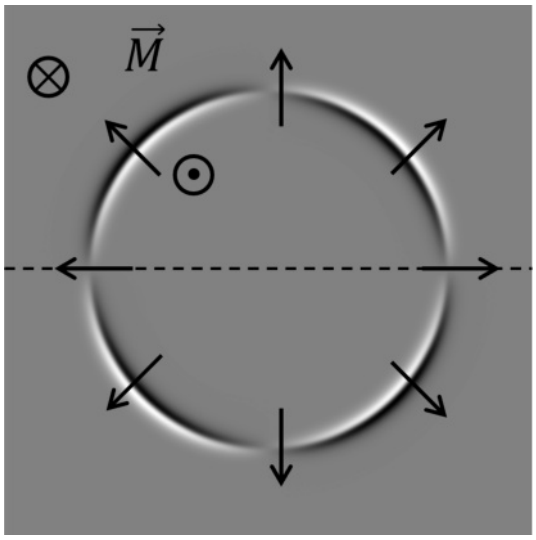

Figure 5.4.: The S_{21} magnetization gradient tensor component for a Néel wall.

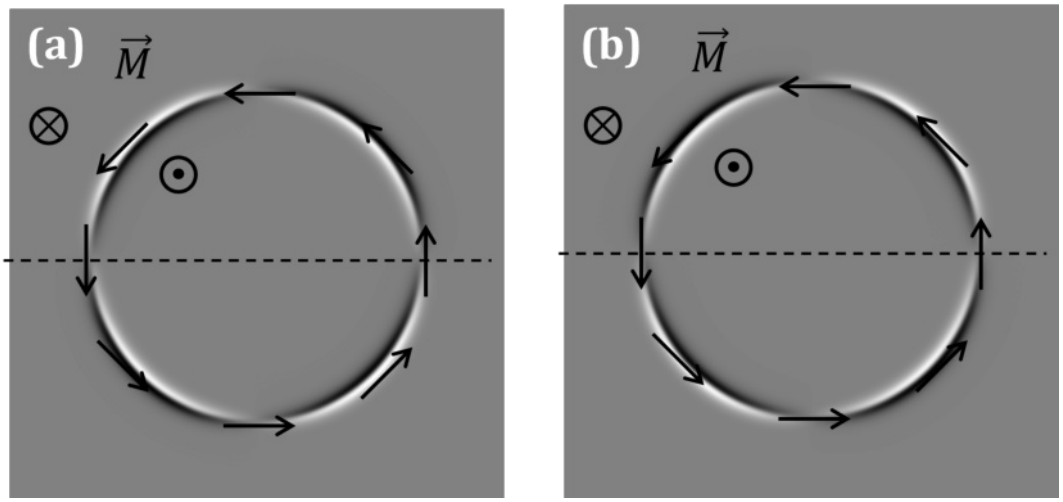

Figure 5.5.: a) S_{11} and b) S_{22} magnetization gradient components calculated for Bloch wall.

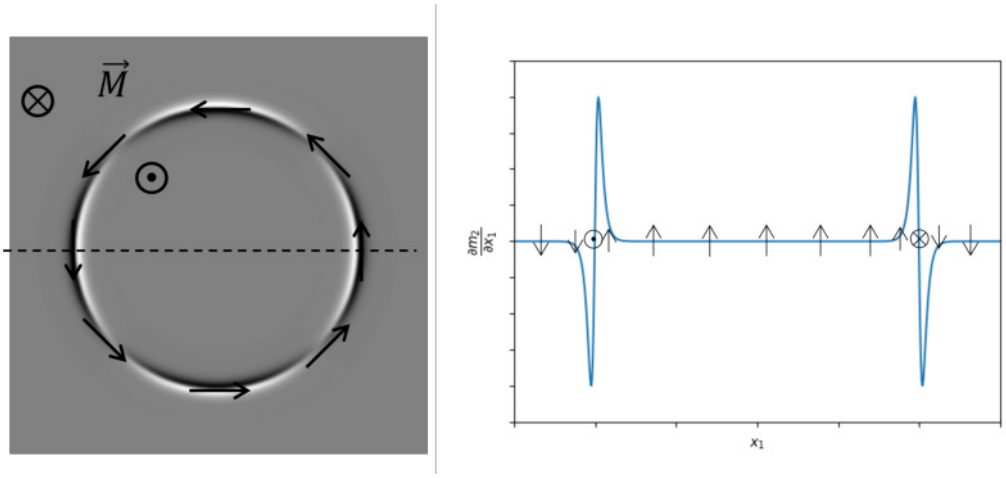

Figure 5.6.: The S_{21} magnetization gradient tensor component for Bloch wall.

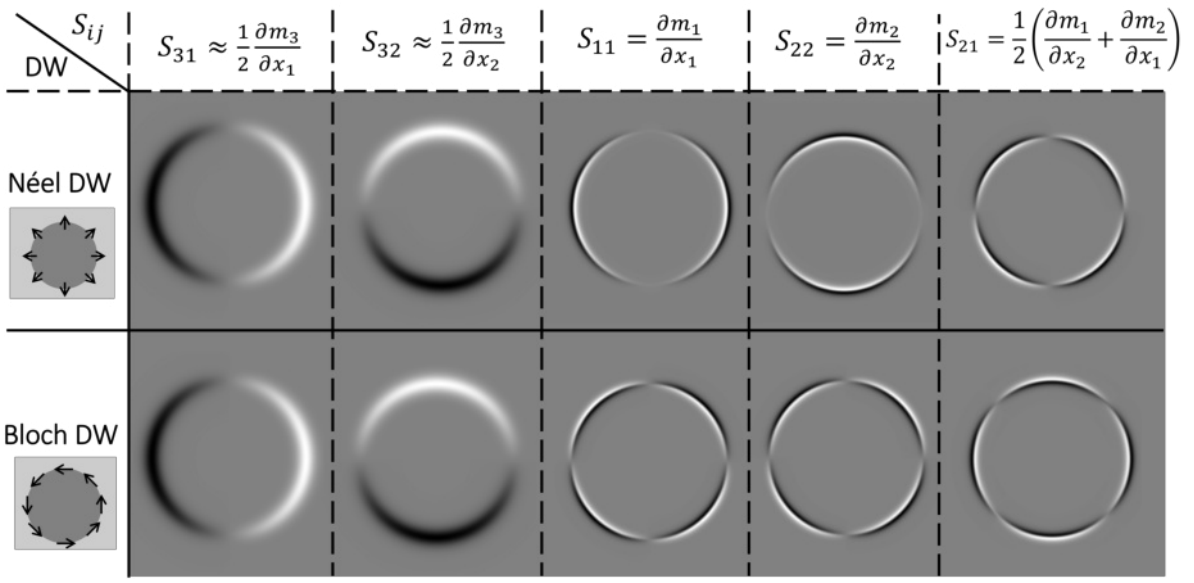

Figure 5.7.: Table of the discussed magnetization gradient tensor components S_{ij} calculated for Néel and Bloch walls.

5.3. Magneto-optical effects separation

Similarly, as we can separate the polar and longitudinal Kerr effects, we can separate the Kerr effects from the gradient effect by using the effects' symmetries. As commented earlier in chapter 3, one does not simply measure the gradient effect in the regular imaging setting, even less so in systems with PMA. The main difficulty is that the Kerr effects are typically much more prominent than the other magneto-optical effects, with the polar Kerr being the most prominent one.

In principle, two options exist for separating the dominant polar Kerr effect from the other magneto-optical effects: 1) proper optics setting and 2) the effects' symmetries exploitation. By varying the incident light polarization, it is possible to invert the Kerr rotation coming from opposite domains. Since its inversion is smooth, finding a specific position where the opposite domains' Kerr rotations vanish is possible. By adjusting the other optical components accordingly, we can remove the polar Kerr contribution while enhancing the gradient effect contribution, which is the approach done in the pioneering work by Schäfer *et al.* [79].

Furthermore, it is advantageous to use the compensator to enhance the gradient effect strength. The utilization of the compensator plays a vital role in both methods because it has been shown that the gradient effect is notably phase-shifted from the Kerr effects [89].

When we look critically at the applicability of the gradient effect, one might argue that the imaging of DWs could be done simply by the Kerr effects since we can separate them relatively conveniently. Moreover, for this reason, some did not deem the gradient effect handy. However, imaging the DWs is only accessible by the Kerr effects if the walls are sufficiently thick (i.e., $> 10^2$ nm). In typical out-of-plane magnetized systems, the width of the walls can be as small as ~ 10 nm, which is when the diffractive phenomena start to prevail at the expense of the classical gyrotropic interactions. Moreover, it is at this stage that the gradient effect could be utilized.

In order to confirm this claim, we now attempt to theoretically describe the experiments in the pure longitudinal Kerr effect geometry conducted in Fig. (5.1). Firstly, we set the incident light propagation along the x_2-axis $\vec{k}_{\pm} = (0, \pm k_2, -k_3)$ (angle of incidence $\approx 35°$), p-polarization along x_2 - $\vec{E} = (0, E_2, \pm E_3)$, and analyzer nearly crossed - sensitive just to D_1. Given the argument that dielectric displacement is proportional to the detected intensity in the image, we may take the first image as $I_1 \sim D_1(\vec{E}, \vec{k}_+)$ and the second image $I_2 \sim D_1(\vec{E}, \vec{k}_-)$, where the $\pm$ sign symbolizes the change of the incident light angle. Under these conditions, we assume the total dielectric displacement as a sum of the Kerr effect (3.7) and the gradient effect (3.14) contributions. We can write the total dielectric displacement following the angle of incidence inversion as

$$\begin{aligned} D_1^{\text{tot},\pm} = D_1^K + D_1^{\text{gr},\pm} = \epsilon_{\text{iso}}(-iQ_V m_3 E_2 \pm iQ_V m_2 E_3) + \\ P\{[\pm S_{32}k_2 - (S_{11} - S_{22})k_3]E_2 + [(S_{33} - S_{11}) + S_{32}k_3]E_3\}. \end{aligned} \tag{5.1}$$

Since the Kerr effect does not explicitly depend on $\vec{k}$, subtracting the two removes the Kerr effect and leaves us with proportionality

$$D_1^{\text{tot,-}} - D_1^{\text{tot,+}} = -iQ_V m_2 E_3 - 2P(S_{32}k_2 E_2 + S_{32}k_3 E_3), \tag{5.2}$$

i.e., the longitudinal Kerr contrast proportional m_2 and a sum of the S_{32} gradient tensor components, all manifesting as the as single contrasts along the x_2 dimension of the DW. Even though the experimental data seem to fit the predicted relation based on the geometry, we cannot distinguish the Kerr and gradient effect contributions from the presented theory perspective.

Besides changing the angle of incidence, another way of exploiting the symmetries of the effects is to change the light polarization state. In a typical magneto-optical microscope measurement, it is not necessary to separate the magneto-optical effects, and even when it is, the angle of incidence inversion is the most convenient way. However, comparing images taken at changed polarization states and thus separating individual components of the gradient effect tensor has not been done in the literature so far. Further, we show different experimental geometries that enable us to systematically explore the magneto-optical response at domain boundaries.

5.4. Gradient effect experiments

In this section, we assemble experimental findings acquired in various optical settings that enable us to probe the gradient effect's symmetries and phenomenology. We discuss the importance of using the compensator, elaborate more on the focusing dependent contrast change and finally show how the boundary contrast changes upon systematic change of the probing polarized light.

5.4.1. Phenomenology of the gradient effect

First, let us start with a nomenclature regarding the polarization-optics components for all measurements. In our measurements, we define the polarization axis angle θ_{pol} of the polarizer as deviation from the x_2-axis, and the analyzer polarization axis θ_{an} and compensator slow axis θ_{comp} angles as deviations from the x_1-axis; see Fig. (5.8). Hence, in this notation, the

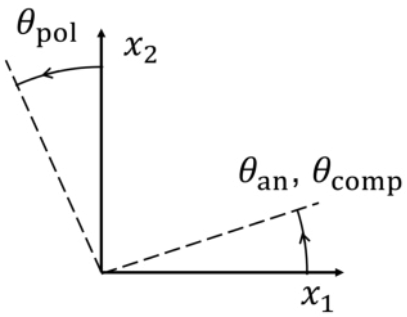

Figure 5.8.: Definition of polarizer, compensator and analyzer rotation angles with respect to our coordinate system.

maximum extinction position is when $\theta_{pol} = \theta_{an} = \theta_{comp} = 0°$. In our experiments, we only use the incident light polarization near the vertical axis up to $\sim 12°$.

The Kerr microscope images presented further are acquired using a standard differential imaging method commonly used in magneto-optical microscopy. This method serves as a way to enhance magneto-optical effects, which are much weaker than the regular non-magnetization effects. In the first step, we take a digital image of a saturated magnetization state (background image), then apply an external magnetic field and thus nucleate particular domains, of which we take a second digital image. The two images are then subtracted; this way, the signal of non-magnetic origin is subtracted while the magnetic signal is amplified.

We mentioned earlier that due to the phase shift of the gradient with respect to the Kerr effect, using a compensator is highly recommended to increase the gradient effect signal. The demonstration is relatively straightforward. As an example, the [Co/Pt] sample was used. The maximum extinction position was found by adjusting the compensator and analyzer in a fixed $\theta_{pol} = 0°$ position and under oblique illumination along the x_2-axis. Afterwards, the polarizer was set to $\theta_{pol} = +2°$, and an out-of-plane field was applied to nucleate a $+M_z$ bubble domain; see the resulting image in Fig. (5.9a). Next, we erased the $+M_z$ bubble, opened the analyzer by $10°$, nucleated and imaged the $+M_z$ bubble domain again. See the double contrast homogeneously distributed along the whole bubble circumference in Fig. (5.9b). By comparing the two images, it is clear that the boundary contrast was massively enhanced while the domain signal remained qualitatively the same. We conducted the two measurements again; however, the polarizer was inverted, i.e., $\theta_{pol} = -2°$; the images are plotted in Fig. (5.9c,d). The first and the second pair of images have opposite domain contrasts; nevertheless, the boundary contrast remained unchanged, as seen in the plotted line scans. Even though we did not exactly rotate the compensator to enhance the boundary contrast, it is the relative analyzer-compensator position that effectively does the enhancement.

Now that we have shown that inverting polarizer does not change the boundary contrast but rather the domain's polarity, the next series of experiments reveal how the other components' inversion changes the contrast conditions. We took a set of four images of $+M_z$ domains under oblique x_2-illumination with the same incident polarization $\theta_{pol} = -4°$ and varied the compensator first to $\theta_{comp} = \pm 10°$ and then the analyzer to $\theta_{an} = \pm 10°$. The result was that the compensator inversion switched both the domain and boundary contrast polarity, whereas the analyzer inversion switched only the boundary contrast polarity; see Fig. (5.10). We repeated this series of experiments even for the Co/Gd sample. What we found was that this sample has the very same boundary contrast polarity in every configuration as the [Co/Pt] sample, while

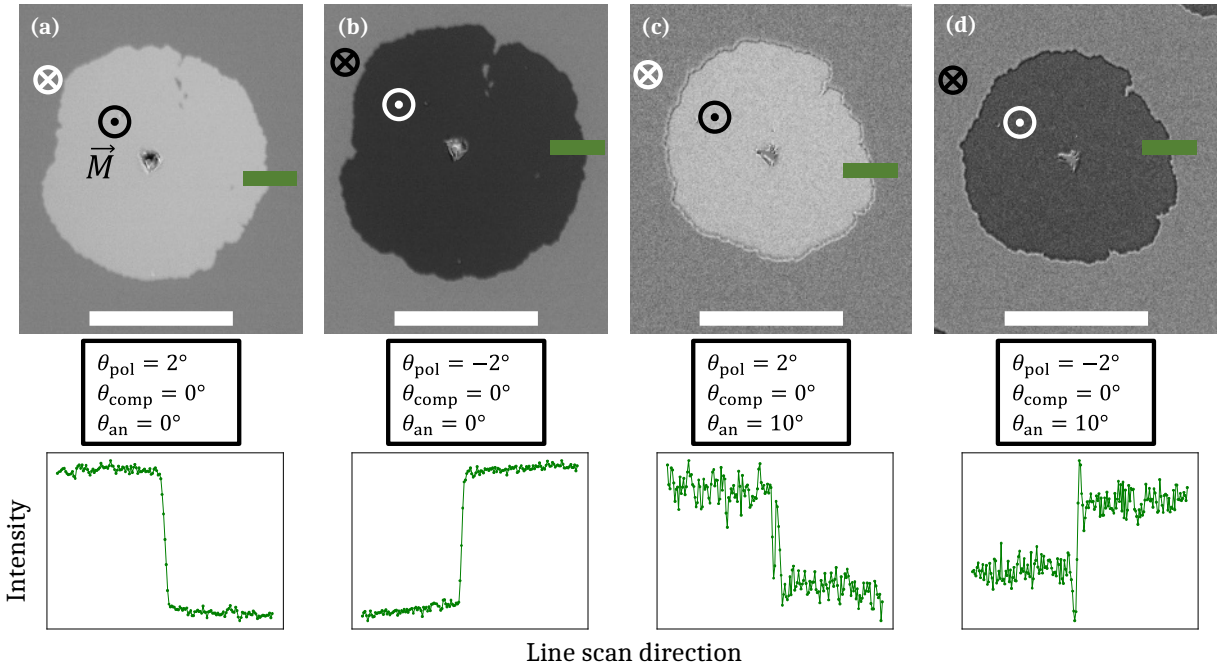

Figure 5.9.: Bubble domain images of [Co/Pt] taken in labeled experimental conditions. Images a) and b) are taken without a relative analyzer-compensator rotation, implementing this relative rotation c) and d) enhances the boundary contrast, as can be seen from the corresponding intensity profiles. The scale bars are 50 µm.

the domain contrast behaved oppositely. The domain contrast kept polarity upon compensator inversion and switched upon analyzer inversion. See the corresponding images in Fig. (5.11).

To conclude these observations, not surprisingly, the polar Kerr contrast is strongly dependent on a material's optical properties. In comparison, it might seem that the gradient effect signal remained the same regardless of the material used. This feature shall be discussed further in the thesis.

Another vital aspect influencing the boundary contrast behavior is the already briefly mentioned dependence on the objective focusing. The single contrast switched polarity upon changing the focusing in Fig. (5.1). This contrast switch might be well exposed if the sample is slightly tilted; therefore, the focusing height over the field of view is not uniform. See an image taken at this condition in Fig. (5.12) in the incident angle inversion geometry along the x_1-axis with constant polarizer position. The sample inclination is along the bottom-left to top-right diagonal. Looking specifically at the boundaries near these corners, we may see that the x_1-single contrast switched here from white to black (on the left side of the domains).

Moreover, we may notice, roughly around the first third of the diagonal, that as the single contrast smoothly transitions also, a double contrast appears. We may learn two main things from this measurement; first, the sample tilt must be very precisely adjusted in order to be as flat as possible and connected with that is a proper focus height adjustment; second, it is reasonable to presume that the double contrast, visible only in part of the image, was present over the whole field of view, however, was hidden under the dominant single contrast. Furthermore, if we manage to remove the single contrast contribution, we might be able to analyze the comparatively narrower double contrast.

In the following experiment, we examine the double contrast in the following geometry: we set the analyzer to $\theta_{an} = -10°$ (to increase the boundary contrast) and adjust the other

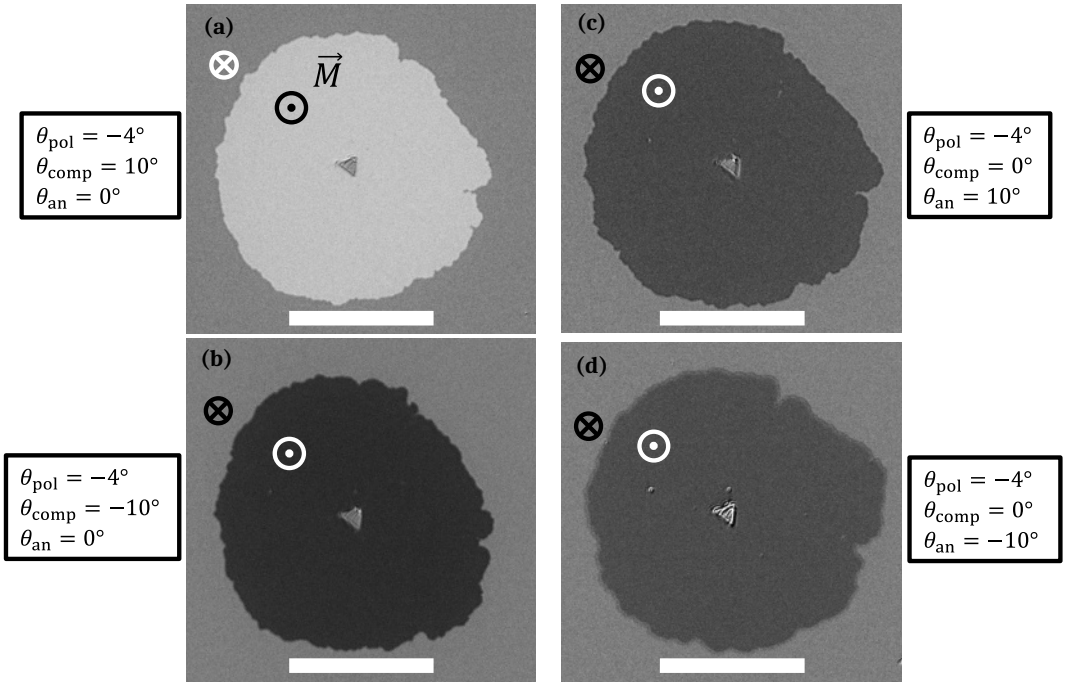

Figure 5.10.: [Co/Pt] domain images taken at labeled experimental conditions, indicating domain contrast switching upon compensator inversion - a) and b), and keeping the domain contrast upon analyzer inversion - c) and d). The scale bars are 50 µm.

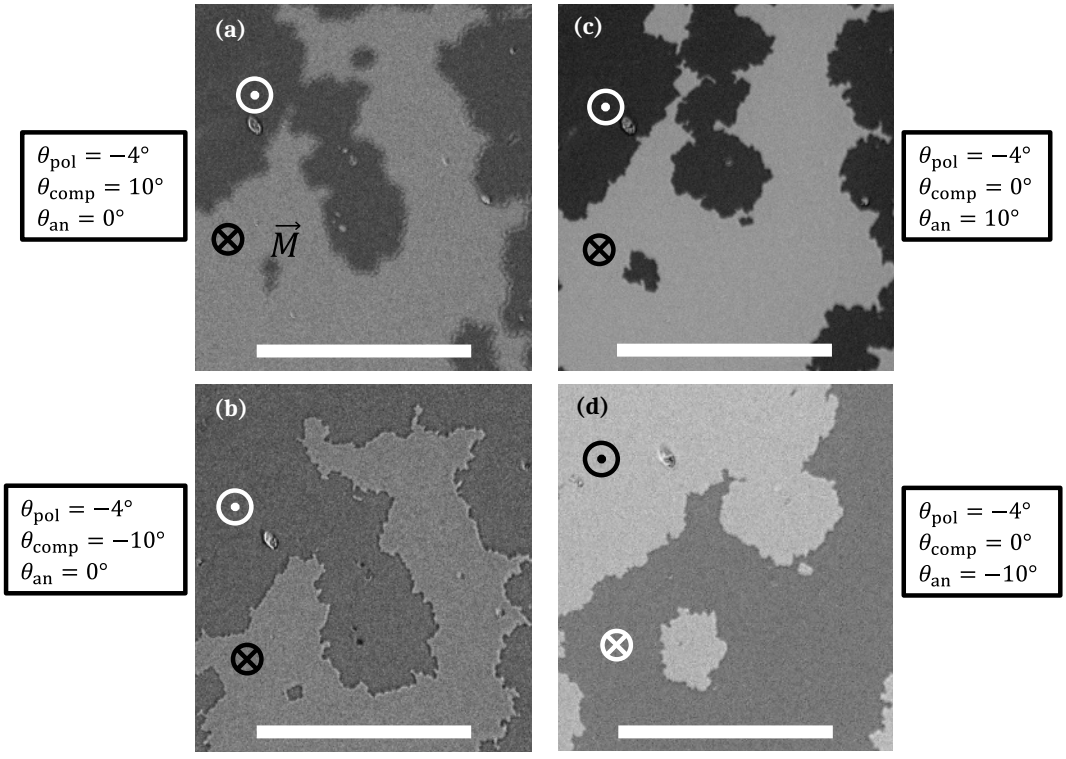

Figure 5.11.: Co/Gd domain images taken at labeled experimental conditions, domain contrast stays unchanged upon compensator inversion - a) and b), while it inverts upon analyzer inversion - c) and d). The scale bars are 50 µm.

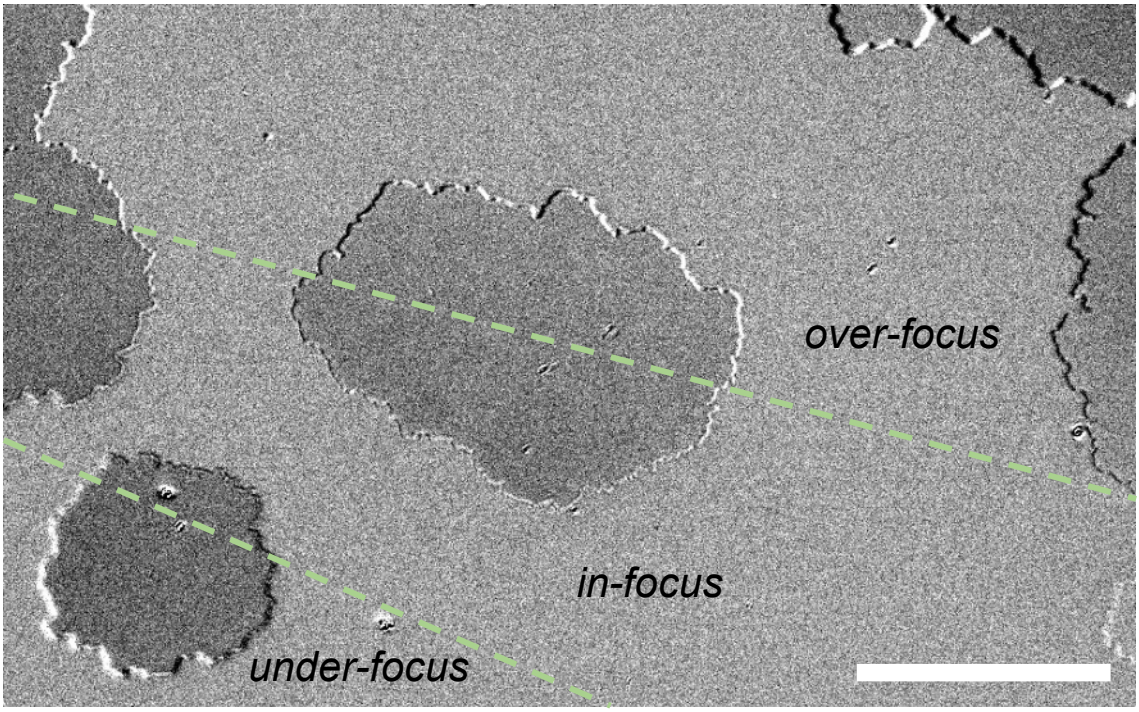

Figure 5.12.: Domain image of a significantly tilted Co/Gd sample eventually leading to single contrast inversion upon going from the under-focused to the over-focused area, whereas the area in-focus shows signs of double contrast. The scale bar is 50 µm.

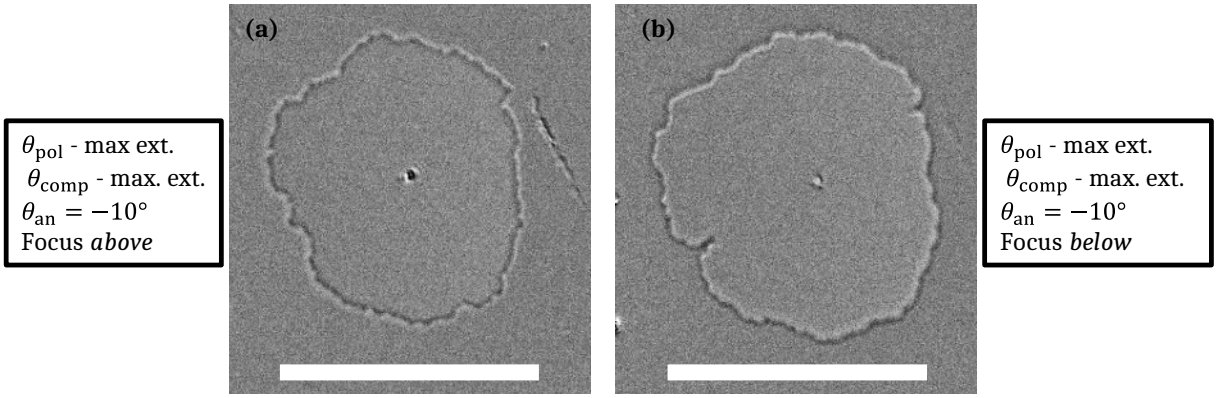

Figure 5.13.: Imaging of double contrast given an analyzer position and with the polarizer-compensator configuration adjusted to obtain maximum extinction of the domain signal. a) Slightly under-focused and b) over-focused images, where the inversion of the double contrast at the domain boundary is observed. Scale bars, 50 µm.

optical elements to annihilate the polar Kerr signal arising from the domains. Nucleating a bubble domain and taking the image under oblique illumination and a small defocus above the sample surface, we get the isolated double contrast; see Fig. (5.13a). If we change the focus height and focus slightly below the sample surface, we also get a double contrast; however, the contrast polarity is switched; the resultant image is plotted in Fig. (5.13b). Note that in order to demonstrate the contrast switching, it was necessary to defocus the objective slightly because focusing ideally on the surface is an exceptionally complex task. Moreover, even if we manage to do so well, the interpretation is a challenge. Mainly because as the double contrast polarity

transitions, we may even get something like a triple contrast, i.e., an ambiguous contrast that may hardly be explained within the scope of the tensor modeling approach we are utilizing.

5.4.2. Separation of the gradient effect components

In this section, we introduce the methodology allowing us to isolate the individual gradient effect components partially. We also suggest an explanation of the particular boundary contrasts through the gradient effect dielectric displacement approach. However, firstly, we comment on the procedure by which the experiments were conducted.

The procedure we use essentially consists of two consecutive differential images. The first differential image (image I_1) is taken in some particular illumination, polarizer, compensator, and analyzer settings. Next, we change the position of the mentioned optical components or even the incident illumination angle and perform a backward differential imaging procedure. Meaning that we save the image with a nucleated domain as a background image; by applying the magnetic field, we erase the domain, take the second image and subtract the two (image I_2). The procedure is schematically illustrated in Fig. (5.14).

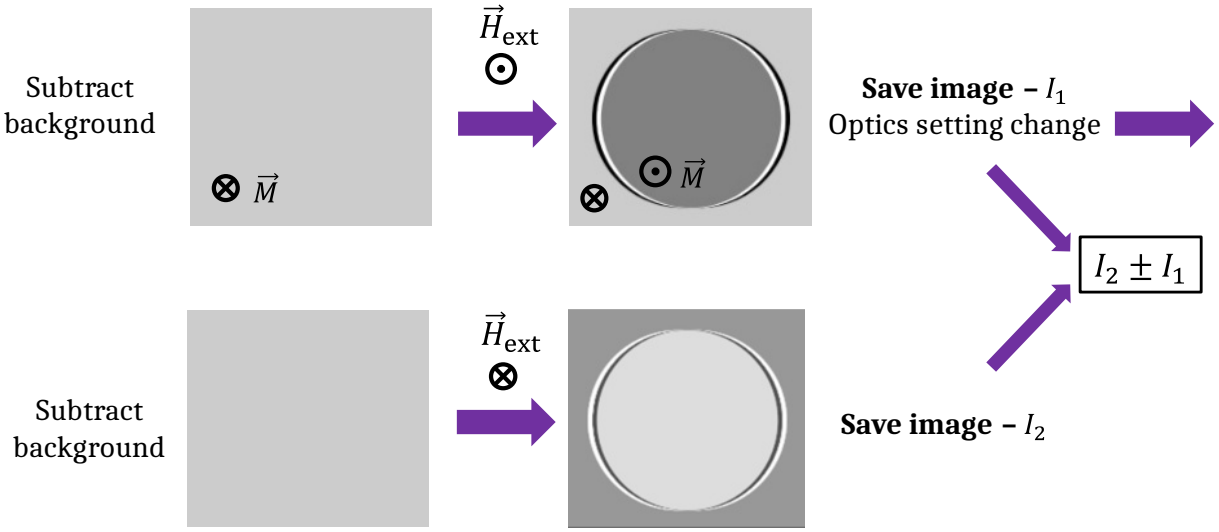

Figure 5.14.: Schematic depiction of a double differential imaging method which takes two images (I_1 and I_2) of the same magnetization state acquired in different optical configurations. Their subtraction or addition is then used to separate gradient effect contributions.

Earlier, we exposed the dielectric law for gradient effect in the pure longitudinal Kerr effect geometry, where we applied only the change of the angle of incidence. In further experiments, we keep the angle of incidence unchanged and work only with the polarization optics components. This means that the first image is, again, $I_1 \sim \vec{D}(\vec{E}, \vec{k})$ and the second image $I_2 \sim \vec{D}'(\vec{E}', \vec{k})$, where the $\vec{E}'$ corresponds to the changed incident polarization due to polarizer change and $\vec{D}'$ to the changed compensator or analyzer. Further, if we add or subtract the two images, I_1 and I_2, we can separate the individual gradient effect components of the dielectric law (3.14). Compared to the angle of incidence inversion, varying the polarization optics elements gives us many more possible geometries for the gradient effect component separation.

The first geometry we will describe is one in which we change only the polarizer. The incident p-polarized light parameters are $\vec{k} = (k_1, 0, -k_3)$ and $\vec{E}_{\pm} = (E_1, \pm\delta E_2, \delta E_3)$, whereas

here we detect only D_2. The corresponding optical elements angles are $\theta_{\text{pol}} = 90° \pm \delta\theta$, $\theta_{\text{comp}} = 90°$, and $\theta_{\text{an}} = 90°$. We write the first differential image as

$$\begin{aligned} D_2^{gr,1} = P\{&[-S_{31}k_1 + (S_{22} - S_{11})k_3]E_1 \\ &+2[-S_{23}k_1 - S_{21}k_3]\delta E_2 \\ &+[(S_{22} - S_{33})k_1 - S_{31}k_3]\delta E_3\}, \end{aligned} \tag{5.3}$$

and the second differential image as

$$\begin{aligned} D_2^{gr,2} = P\{&[-S_{31}k_1 + (S_{22} - S_{11})k_3]E_1 \\ &-2[-S_{23}k_1 - S_{21}k_3]\delta E_2 \\ &+[(S_{22} - S_{33})k_1 - S_{31}k_3]\delta E_3\}, \end{aligned} \tag{5.4}$$

See the corresponding images in Fig. (5.15a,b). Note that the second image is a negative image; therefore, we have to write $I_2 \sim -D_2^{gr,2}(\vec{E}', \vec{k})$. The data were measured in the Co/Gd sample with $\theta_{\text{pol}} = \pm 1°$. In order to remove the disturbing domain signal, we have to subtract the two images, which leaves us with

$$I_2 - I_1 \sim D_2^{gr,2} - D_2^{gr,1} = 2P[-S_{31}k_1 + (S_{22} - S_{11})k_3]E_1 + [(S_{22} - S_{33})k_1 - S_{31}k_3]E_3, \tag{5.5}$$

and the image corresponding to the subtraction is plotted in Fig. (5.15c).

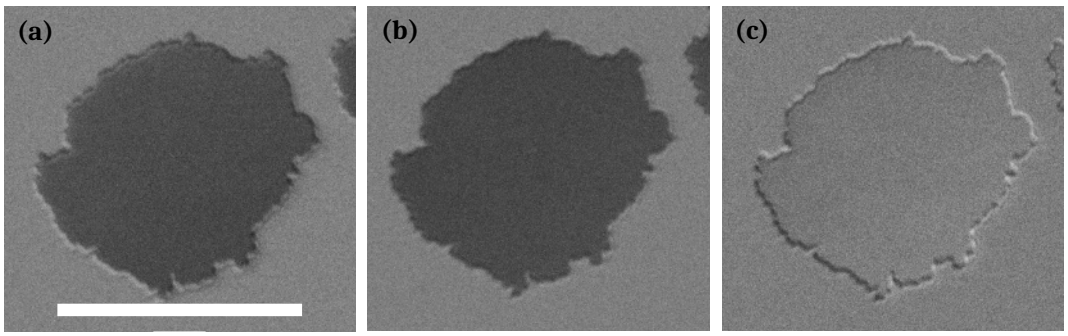

Figure 5.15.: Double differential imaging method used for domains in Co/Gd. a) corresponds to an image taken at $\theta_{\text{pol}} = +1°$, while b) to $\theta_{\text{pol}} = -1°$, The image in c) is the result of their subtraction. The scale bar is 50 µm.

In the subtraction image, we may notice two main features. First, there is a significant single contrast along the x_1-axis; second, there is also a significant x_2-double contrast. In the subtraction equation (above), the two features are represented by the S_{31} and S_{22} components, respectively. While the S_{22} component is even amplified as it occurs in both terms with E_1 and E_3, the S_{11} and S_{33} components were not detected. The presence of S_{33} was not simply detected because the polar component of magnetization does not change within the penetration depth of the light. Even if it was, it is questionable if we were able to measure that; hence, the S_{33} component will be omitted hereafter. Furthermore, the S_{11} component (i.e., x_1-double contrast) was not likely detected because it was overwhelmed by the x_1-single contrast.

The second of the more basic geometries uses a constant polarizer position; what we change is the detected dielectric displacement and thus work with the analyzer ($\theta_{\text{an}} = \pm 10°$). The first differential image thus will be proportional to $I_1 \sim (D_1^{gr}, \delta D_2^{gr}, 0)$, while the second

(negative) image will be $I_2 \sim -(D_1^{gr}, -\delta D_2^{gr}, 0)$. In the following experiment, we use oblique incidence along x_2 $\vec{k} = (0, k_2, -k_3)$ this time and again the p-polarization $\vec{E} = (0, E_2, \delta E_3)$. By subtracting the two dependencies, we obtain

$$I_2 - I_1 \sim -2D_1^{gr} = 2\{[S_{32}k_2(S_{22} - S_{11})k_3]E_2 + [-S_{11}k_2 + S_{32}k_3]\delta E_3\}, \tag{5.6}$$

while by summing, we get

$$I_2 + I_1 \sim 2\delta D_2^{gr} = 4\{-S_{21}k_3E_2 + [-S_{21}k_2 - S_{31}k_3]\delta E_3\}. \tag{5.7}$$

Now, in Fig. (5.10), we showed that in the [Co/Pt] sample, inverting the analyzer does not switch the domain signal contrast. Therefore, to remove the domain signal, we must sum the two corresponding images (since the second one is negative); see the sum image in Fig. (5.16a). The theory suggests that in the present case of a Néel wall, we should detect an x_1-single contrast and the diagonal double contrasts (from S_{21}). However, we detected neither of those; moreover, we detected the homogeneous double contrast. The double contrast explanation in this particular case still needs to be investigated more in detail, with more measurements using this sample.

Next, we examine the [Co/Ni] sample using the same analyzer-inversion geometry. Opposite to [Co/Pt], [Co/Ni] switches domain contrast upon analyzer inversion, meaning that the I_1 and I_2 must be subtracted to eliminate the polar Kerr signal. In this case, the corresponding proportionality is (5.7), and the image is plotted in Fig. (5.16b). Despite the theory suggestion, which says that we should see an x_2- and two times as intense x_1-double contrast (E_1 and E_3 contribution), here, the subtraction image appears as if there was solely an x_2-single contrast. Upon closer examination, the double contrast on the left and right sides of the bubble, where the x_2-single contrast transitions, vanishes; however, a weak x_2-double contrast can indeed be spotted.

Comparing the results discussed so far, we may notice a disparity between the individual gradient tensor components depending on the measured sample. The disagreement between the experiments and the predicted boundary contrasts may be massively influenced by the simplicity of the dielectric law (3.14) we use. Since we use only one material parameter, P, all gradient effect permittivity tensor components have the same weights. This limitation was aforementioned by Thiaville *et al.* in Ref. 81. The earlier derivation of $\hat{\epsilon}^{\text{gr}}$ (3.13) employed two material parameters: the P' parameter was present in components including S_{3i}, while the P parameter was in the rest. Therefore, assuming two material parameters, it might be the case for the result in (5.16) that $|P'| > |P|$ in [Co/Ni]. Additionally, since P' and P are generally complex quantities, there might even be some phase difference imposed by the two parameters depending on the incidence of light.

Another experimental geometry combines the two previous ones, i.e., simultaneous polarizer and analyzer inversion ($\theta_{\text{pol}} = \pm 2°$, $\theta_{\text{an}} = \pm 10°$). This time, we illuminated the [Co/Pt] (on glass) sample under normal incidence, hence $\vec{k} = (0, 0, -k_3)$ and used the polarization $\vec{E} = (\pm\delta E_1, E_2, 0)$. We can write the intensity proportionality in short form as $I_1 \sim (D_1^{gr}(+\delta E_1), \delta D_2^{gr}(+\delta E_1), 0)$ and $I_2 \sim (-D_1^{gr}(-\delta E_1), \delta D_2^{gr}(-\delta E_1), 0)$, where we do not write the E_2 dependence explicitly since it remains unchanged during the measurement. In this scenario, the subtraction operation suffices, and it gives us

$$I_2 - I_1 \sim (S_{22} - S_{11})k_3\delta E_1 + (S_{22} - S_{11})k_3E_2. \tag{5.8}$$

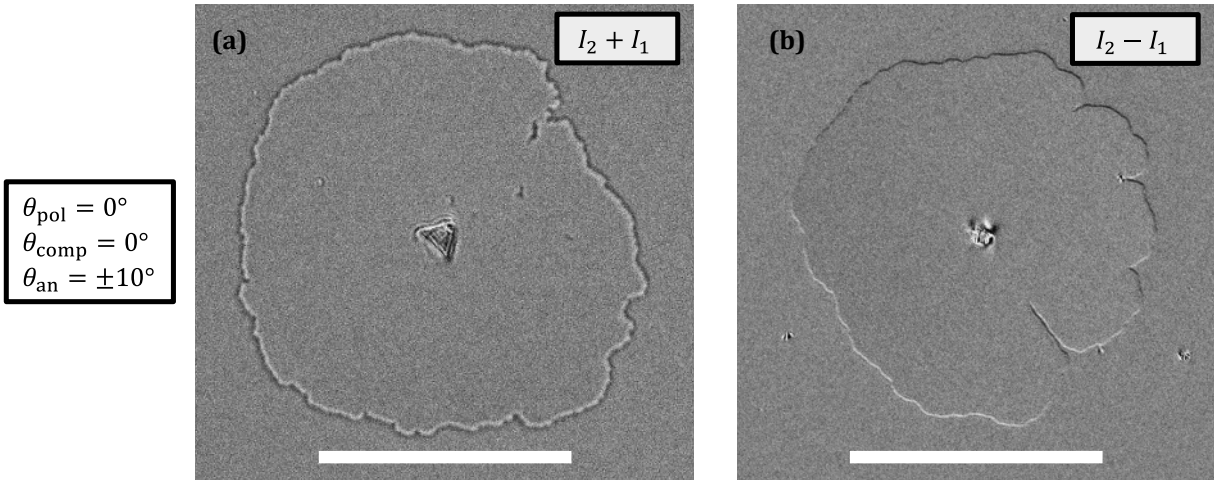

Figure 5.16.: Differential images taken in labeled experimental conditions. While in a) [Co/Pt], the domain contrast is not changed upon analyzer inversion, it has to be removed by summation, for b) [Co/Ni], the domain signal switches with analyzer inversion. Hence, the domain signal is removed upon subtraction. The scale bars are 50μm.

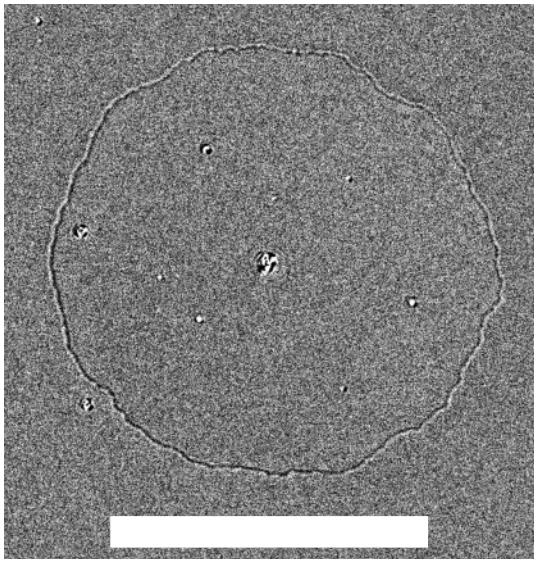

Figure 5.17.: Differential image of [Co/Pt] in $\theta_{pol} = \pm 2°$ and $\theta_{an} = \pm 10°$, resulting in homogeneous double contrast along the whole bubble circumference. The scale bar is 50 µm.

According to this dependence, the subtraction image should result in nothing more than a double contrast with opposite polarities along the x_1 and x_2-axes. However, instead, we see a highly homogeneous double contrast; the image is depicted in Fig. (5.17), and this double contrast behavior explanation is yet to be found.

Alternatively, we can measure in geometry with the analyzer starting position as negative, meaning $\theta_{pol} = \pm 2°$ and $\theta_{an} = \mp 10°$. In this modification, the images correspond to $I_1 \sim (D_1^{gr}(+\delta E_1), -\delta D_2^{gr}(+\delta E_1), 0)$ and $I_2 \sim (-D_1^{gr}(-\delta E_1), -D_2^{gr}(-\delta E_1), 0)$. The subtraction dependence is as follows

$$I_2 - I_1 \sim -(S_{22} - S_{11})k_3\delta E_1 + (S_{22} - S_{11})k_3 E_2. \tag{5.9}$$

In contrast to the previous equation (5.8), here, the two double contrast contributions oppose each other. Despite the sign difference, the double contrast should at least partially remain since $E_2 >> E_1$. Nevertheless, the subtraction image in this geometry apparently deletes the double contrast entirely and leaves us with only an x_2-single contrast; see Fig. (5.18). The proposed dependence (5.9) could not explain this utterly unexpected single contrast.

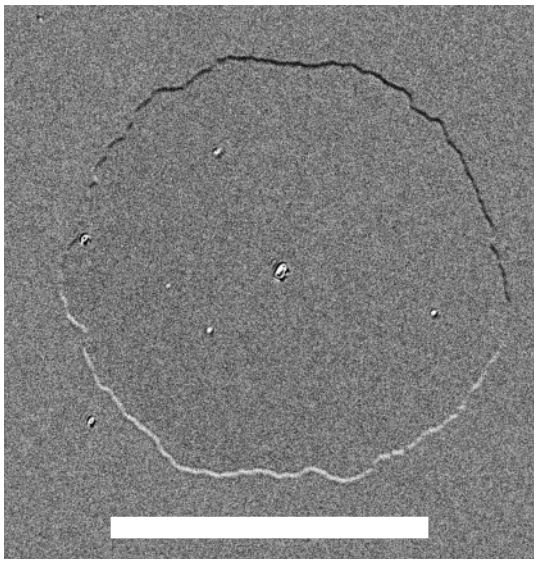

Figure 5.18.: Differential image of [Co/Pt] in $\theta_{\text{pol}} = \pm 2°$ and $\theta_{\text{an}} = \mp 10°$, resulting in ambiguous x_2-single contrast. The scale bar is 50 µm.

In order to determine whether the single contrast appearance in such geometry is a sample specification or a general rule, we repeated the experiment for the [Co/Ni] sample. Additionally, we increased the E_2/E_1 ratio by opening the polarizer more ($\theta_{\text{pol}} = \pm 10°$), hoping to influence the degree to which the two opposing double contrast contributions subtract. See the resulting subtraction image in Fig. (5.19a) taken under normal incidence. The single contrast remains here as well, supporting the independence of the structure of the examined specimen.

Furthermore, we examined this geometry using oblique illumination. A general dependence of the gradient effect in this geometry takes a rather complicated form

$$\begin{aligned} I_2 - I_1 \sim -[&S_{31}k_1 + S_{32}k_2 + (S_{22} - S_{11})k_3]\delta E_1 \\ [&-S_{31}k_1 + S_{32}k_2 + (S_{22} - S_{11})k_3]E_2 \\ [&S_{21}k_1 - S_{11}k_2 + S_{32}k_3]\delta E_3 \end{aligned} \tag{5.10}$$

Overall, we have done this experiment in five incident illumination configurations: normal and one oblique from all four directions, i.e., $\vec{k}_1 = (0, 0, -k_3)$, $\vec{k}_{2,3} = (\pm k_1, 0, -k_3)$, and $\vec{k}_{4,5} = (0, \pm k_2, -k_3)$. All the corresponding subtraction images are shown in Fig. (5.19). In conclusion, we may state that this x_2-single contrast remains unchanged regardless of the incident light illumination; therefore, it has to be sensitive only to the k_3 component since it is what all five configurations have in common. As this contrast does not adhere to the one determined by (5.10), we may have to find other ways of describing the measured boundary contrasts.

Last, we examined the [Fe/Gd] sample - the only multi-layered system with Bloch walls. By comparing this sample's measurements in the discussed geometries with the previous ones having Néel wall, we wanted to find whether or not the gradient tensor components manifest

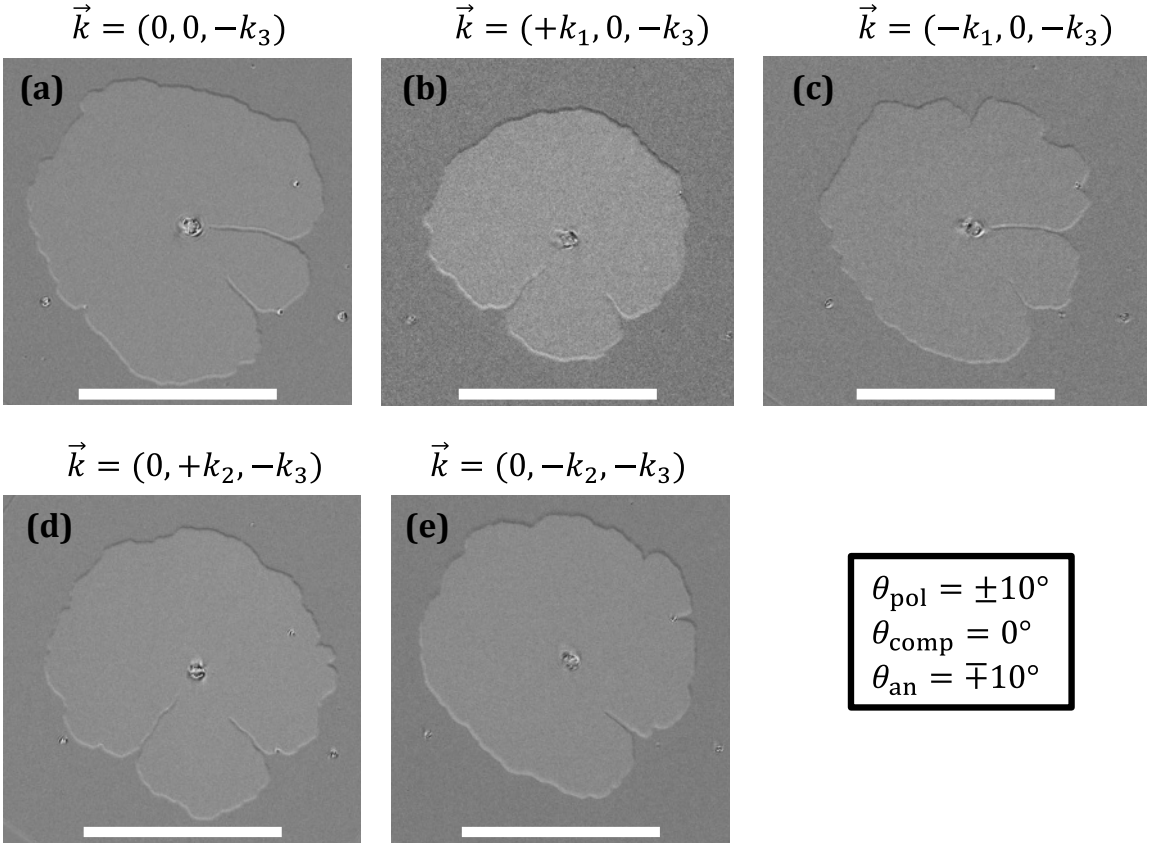

Figure 5.19.: Differential images of domains in [Co/Ni] sample in $\theta_{\text{pol}} = \pm 10°$ and $\theta_{\text{an}} = \mp 10°$ geometry under different incident illumination angles, all resulting in qualitatively same boundary contrast. The scale bars are 50 μm.

differently as predicted theoretically in Fig. (5.7). As shown earlier, this sample has very low coercivity; hence, the magnetic domains form a maze-like structure. In an effort to see the homogeneous double contrast observed in Fig. (5.17), we conducted an experiment at the corresponding geometry $\theta_{\text{pol}} = \pm 10°$ and $\theta_{\text{an}} = \pm 10°$, and the resulting image is captured in Fig. (5.20a). The low coercivity of the system caused the domains to move in order of micrometers throughout the measurement procedure. Eventually, the displacement resulted in a blurry and divisive boundary contrast, leading to a challenging interpretation of the results. Furthermore, we attempted imaging in the geometry characterized by the x_2-single contrast using $\theta_{\text{pol}} = \pm 10°$ and $\theta_{\text{an}} = \mp 10°$. We obtained a similar not-so-straightforward boundary contrast to clarify; see Fig. (5.20b).

The methodology we use is primarily qualitative rather than an exact description of the optical response of a system, just as for the Lorentz concept of the Kerr effect. Within this approach, we argue that the product $-\vec{m} \times \vec{E}$ is ultimately proportional to the domain signal. Nevertheless, this direct use of the dielectric law to describe the detected intensity does not consider the system's intrinsic properties or the phase shift aspects. A more complex and suitable approach is to obtain a Fresnel reflectivity matrix of the system and then use the Jones calculus to determine how the reflection affects the incident light polarization. The following section describes this more complex approach utilizing the *transfer matrix method* and Jones formalism.

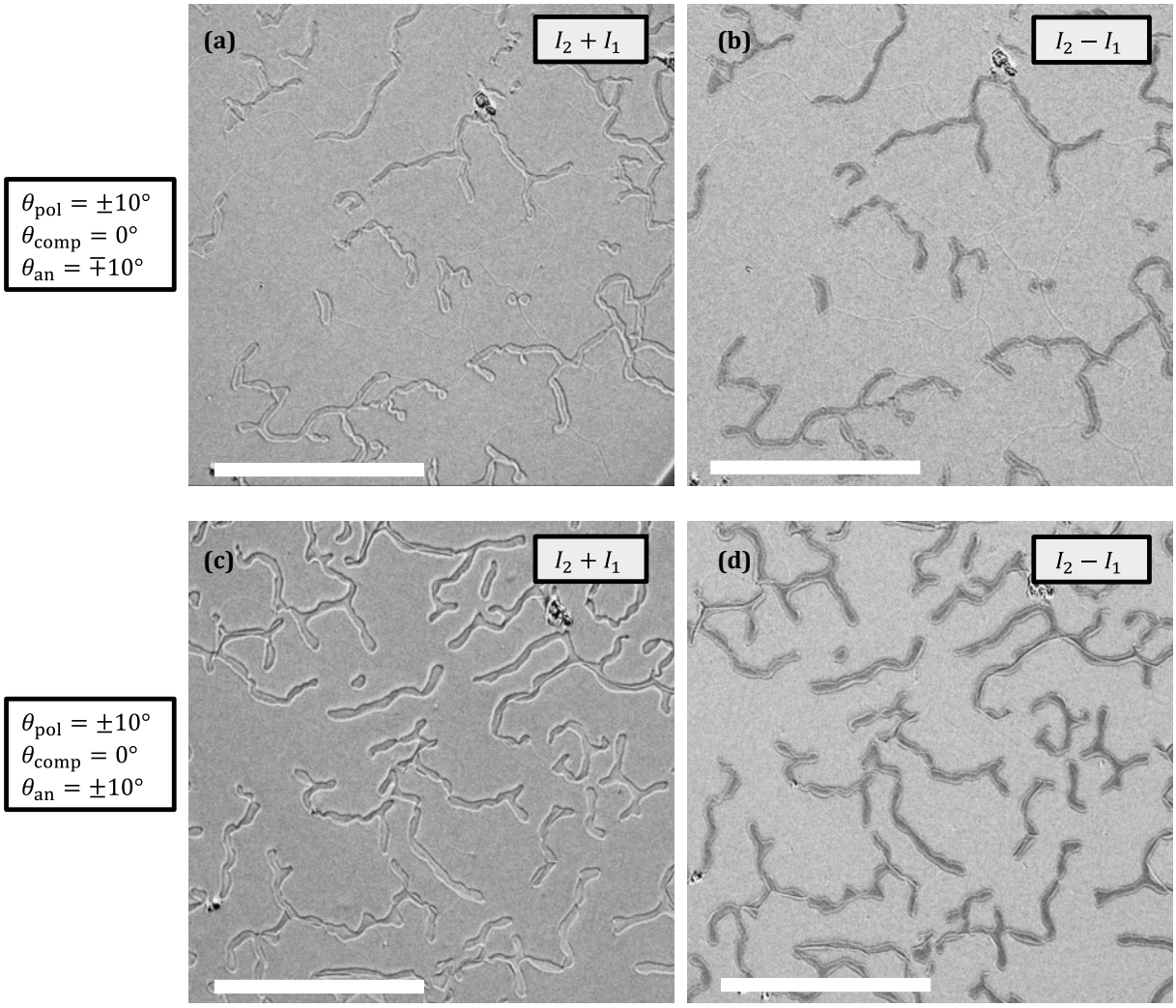

Figure 5.20.: [Fe/Gd] stripe domains images taken by differential imaging. Images a) and b) are addition and subtraction images taken in $\theta_{pol} = \pm 10°$ and $\theta_{an} = \mp 10°$ geometry, while c) an d) are taken in $\theta_{pol} = \pm 10°$ and $\theta_{an} = \pm 10°$ geometry. The scale bars are 50 µm.

5.5. Differential imaging simulations

The transfer matrix method is used to calculate light propagation in layered anisotropic media with a linear optical response. Based on the 4×4 differential matrix algorithm by Berreman and Yeh [90, 91], it utilizes such a transfer matrix to connect the incident polarization amplitudes with the reflected and transmitted ones. Since this transfer matrix describes the optical properties of the system, it is possible to find general solutions connecting the transfer matrix elements with Fresnel reflection coefficients.

We will not explain the calculus in this formalism itself in detail; we refer to Refs. 92–94. Ultimately, this method allows us to go from the arbitrary dielectric tensor of the system to its reflection matrix. We used the transfer matrix method and Jones formalism to simulate magneto-optical signals originating from the gradient effect. The principle is outlined in Appendix A.

We showed earlier that the dielectric law (3.14) and the Lorentz concept methodology could partially explain the observed gradient effect signal. Nevertheless, it only considered the distribution of magnetization, the properties of the incident light, and the detected dielectric displacement components. However, the description of the phenomenon not only depends on the system's magnetization but also on its intrinsic optical properties. Moreover, this approach does not account for the phase aspect of the reflected light; hence, the presence of the compensator was not properly represented. These shortcomings can partially be surpassed by using the aforementioned transfer matrix methodology.

Let us take the experiment geometry described by the equation (5.8) with the result plotted in Fig. (5.17a). Further, we expand our analysis by performing a series of experiments in this geometry with the sample [Co/Pt] sample, where we increase the opening angle of the polarizer. So the set of experiments is $\theta_{\text{pol}} = \pm 2°, \pm 4°, \pm 6°$, with $\theta_{\text{an}} = \pm 10°$ in all of them. The three cases are plotted in Fig. (5.21a,b,c).

We can immediately spot that the magneto-optical signal in all three cases differs significantly. Most notably, the image (5.21b) was the only one in which the domain contrast could not be removed by subtraction. The explanation is that roughly around this $\theta_{\text{pol}} = \pm 4°$ configuration, the opposite domains' Kerr rotations are almost equalized, and turning the analyzer to $\pm 10°$ does not switch the nearly-compensated domain contrast. Therefore, subtracting the two enhances the Kerr domain contrast since the second differential image is negative. Nevertheless, the domain contrast is not too overwhelming, and the boundary contrast is still apparent. Another changing feature is that whereas the $\theta_{\text{pol}} = \pm 2°$ image shows a homogeneous double contrast, the $\theta_{\text{pol}} = \pm 6°$ only shows a visible double contrast along the left bottom-right top diagonal with the double contrast along the perpendicular diagonal vanishing. Furthermore, the $\theta_{\text{pol}} = \pm 2°$ image double contrast has a black stripe on the inside of the bubble, whereas, in $\theta_{\text{pol}} = \pm 4°$ and $\theta_{\text{pol}} = \pm 6°$ images, the inner bubble-side stripe is white.

Next, we show this experimental geometry simulation in the corresponding optics configuration. See the normalized simulated intensities plotted images in Fig. (5.21d,e,f). First, we must say that the presented simulations do not entirely agree with the experimental data. However, some elements characterize the experiments well. Most notably, we notice that boundary contrast has indeed switched between $\theta_{\text{pol}} = \pm 4°$ and $\theta_{\text{pol}} = \pm 6°$ polarizer opening. Even though the boundary contrast polarity switches between $\theta_{\text{pol}} = \pm 2°$ and $\theta_{\text{pol}} = \pm 4°$ in the experiments, the switching does occur. This slight disagreement may be attributed to errors in the nominal thicknesses of the individual layers of the system, their intermixing or even to differences in the optical properties of the layers compared to the ones found in the literature. Another common aspect of the simulations is that they resemble a single contrast with accompanying x_1- and x_2-double contrasts along one diagonal and a vanishing signal along the other. Moreover, looking closer at the $\theta_{\text{pol}} = \pm 6°$ experimental data, the simulations correspond rather well. Despite using the more physically correct approach, compared to the Lorentz concept, we still could not replicate the homogeneous double contrast appearance and ended up with the alternating double contrast instead.

Now we focus on the other experimental geometry with the simultaneous polarizer and analyzer inversion, as in Fig. (5.18), where the optics setting was $\theta_{\text{pol}} = \pm 2°$ and $\theta_{\text{an}} = \mp 10°$. Similarly, as previously, we conduct a set of experiments with increasing polarizer angle $\theta_{\text{pol}} = \pm 2°, \pm 4°, \pm 6°$, and with $\theta_{\text{an}} = \mp 10°$ in all cases. The series is plotted in Fig. (5.22a,b,c). In contrast to the series in Fig. (5.21), we may notice no change in the boundary contrast, and the diagonal single contrast prevails.

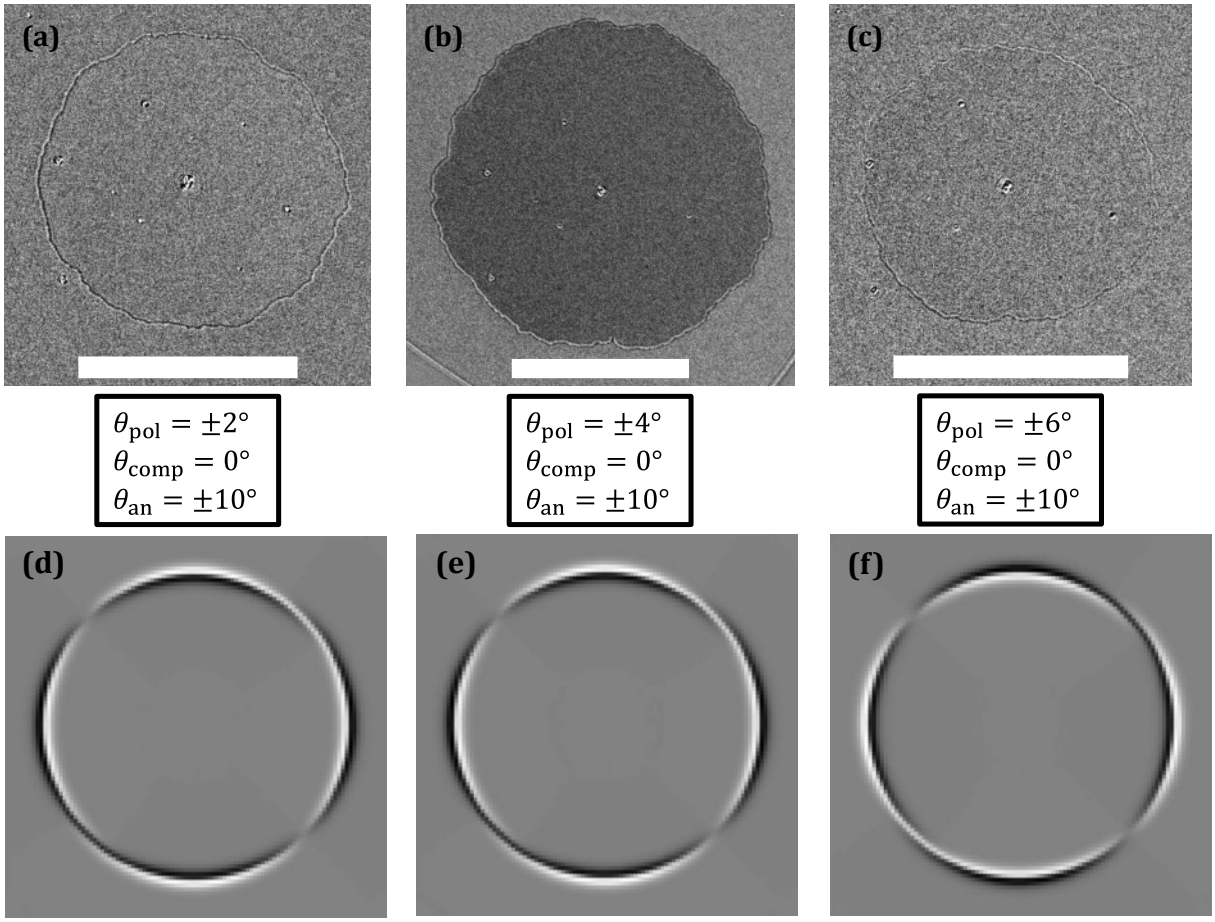

Figure 5.21.: Subtraction differential domain images in [Co/Pt] in experimental geometry with increasing polarizer opening angle a) $\theta_{pol} = \pm 2°$, b) $\pm 4°$, c) $\pm 6°$ and $\theta_{an} = \pm 10°$. Simulations of corresponding experiment geometries are plotted in d), e) and f). The scale bars are 50 µm.

Fig. (5.22d,e,f) shows the corresponding simulations in this geometry. Even though the simulations show double contrast along the x_1- and x_2-axes, the diagonal single contrast keeps its polarity across the series as it does in the experiments.

Since even in the transfer matrix method simulations, we use a single material parameter in the gradient effect permittivity tensor, all the gradient components bear the same weight. This simplification is eventually projected into a possible inaccuracy for all simulations; despite that, the simulations at least allow us to get a glimpse of the gradient effect symmetries.

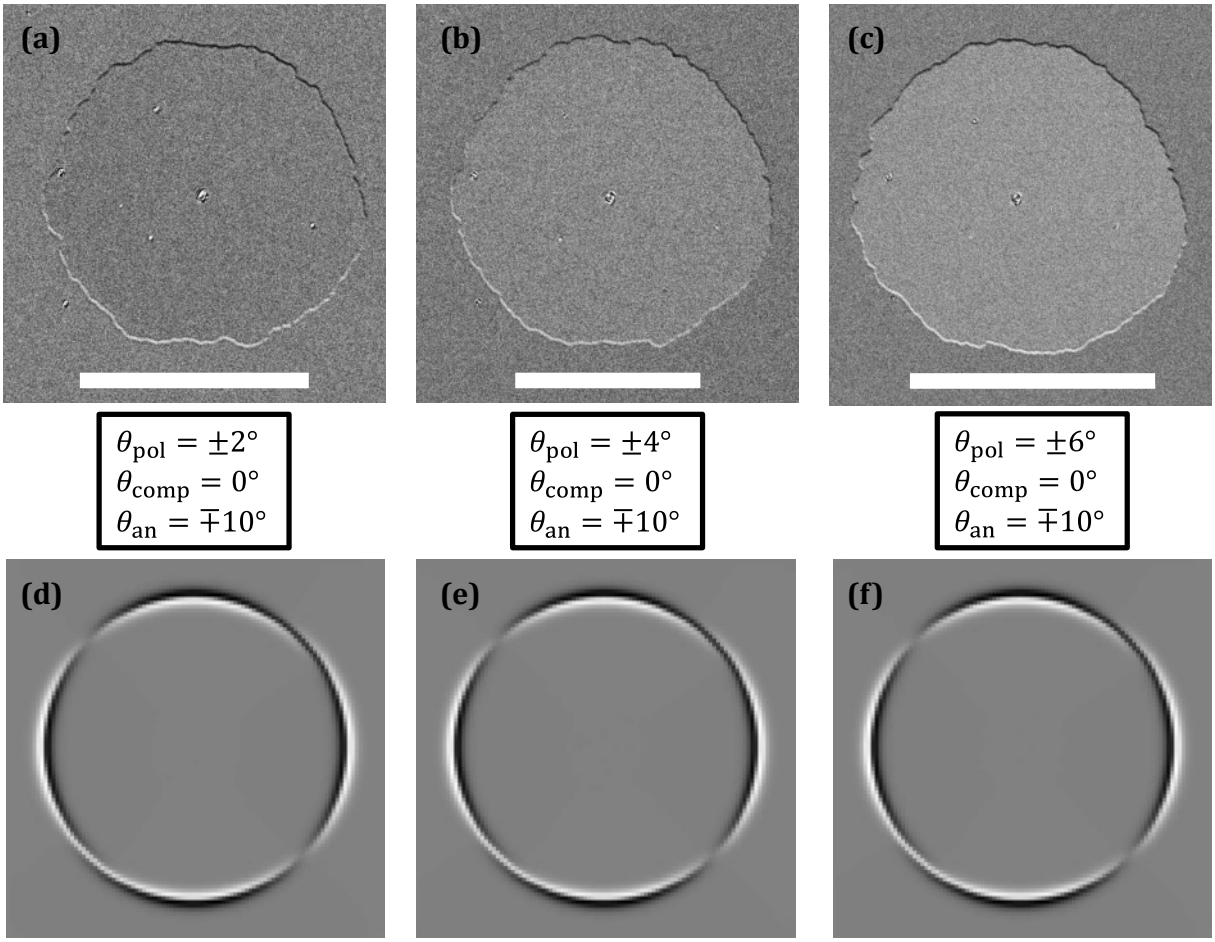

Figure 5.22.: Differential domain images in [Co/Pt] in experimental geometry upon subtraction with increasing polarizer opening angle a) $\theta_{pol} = \pm 2°$, b) $\pm 4°$, c) $\pm 6°$ and $\theta_{an} = \mp 10°$. Simulations of corresponding experiment geometries are plotted in d), e) and f). The scale bars are 50 µm.

6. Proposal for optical imaging of domain wall type and chirality

The pioneering studies on the gradient effect [20, 79, 81], focusing only on a single contrast, state that no information on the internal structure of the DW can be obtained from its features. However, the work studying a double contrast [80] inherently supposed a specific internal wall structure and proved that the structure does contribute to the boundary contrast. To put the utility of our simulations into perspective, the main reason for their implementation was to find to what extent the dielectric law theory correctly describes the observed boundary contrast. Further, after having the knowledge of the theory and experiment correspondence, we aimed to find whether it is possible to use the gradient effect to probe the internal DW structure. Here, we propose simulating other wall structures apart from those present in our samples and searching under what experimental conditions the DWs can be recognized.

In this chapter, we take what we have learned from the experiment-simulation correspondence in the case of Néel walls and translate the system's response if the DW was instead Bloch-type or of opposite chirality. More specifically, we focus on the two geometries with simultaneous polarizer-analyzer inversion. We will use the [Co/Pt] system in the following simulations.

First, we simulate a Néel wall in $\theta_{\text{pol}} = \pm 2^\circ$ and $\theta_{\text{an}} = \pm 10^\circ$ geometry under perpendicular incidence and both wall chiralities. In one case, the in-plane magnetization components of the wall point inside the bubble domain (-1 chirality), and in the other, they point outside ($+1$ chirality). The results, including subtraction and addition, are plotted in Fig. (6.1). Comparing the subtraction images to results with opposite chirality, we can see that the only difference is an overall switch of contrast polarity. The addition images give an alternating diagonal double contrast; however, in the case of [Co/Pt], the addition enhances the polar Kerr domain contrast and hence is not advantageous for experimental verification.

In the next set of simulations, we modelled a Bloch wall with counter-clock-wise chirality ($+1$ chirality) using the geometry with $\theta_{\text{pol}} = \pm 2^\circ$ and $\theta_{\text{an}} = \mp 10^\circ$. Here, the alternating diagonal double contrast appears in subtraction, and the stronger diagonal single contrast in the addition, see Fig. ((6.2) a,b). Simultaneously, we simulated the Néel wall with -1 chirality in the same geometry, and we saw that the subtraction gives the diagonal single contrast, while the addition alternating diagonal double contrast; see Fig. (6.2 c,d). When we compare the results with the Bloch and the Néel walls, Fig. (6.2), we can notice that it appears as if the subtraction and addition dependencies were swapped. Reversing the Bloch wall chirality (-1 chirality) results solely in a contrast polarity inversion.

Put together, we have demonstrated the swapping of subtraction and addition dependencies upon changing the DW from Néel to Bloch type using simulations. Therefore, we suggest that it could be possible to differentiate between the two DW types by measuring and comparing both geometries. Nevertheless, since the experiments and simulations are not in complete agreement and several open questions remain, the reliability of this suggestion for the DW differentiation needs to be further investigated. Moreover, additional experiments in systems with Bloch walls need to be conducted to support our proposal.

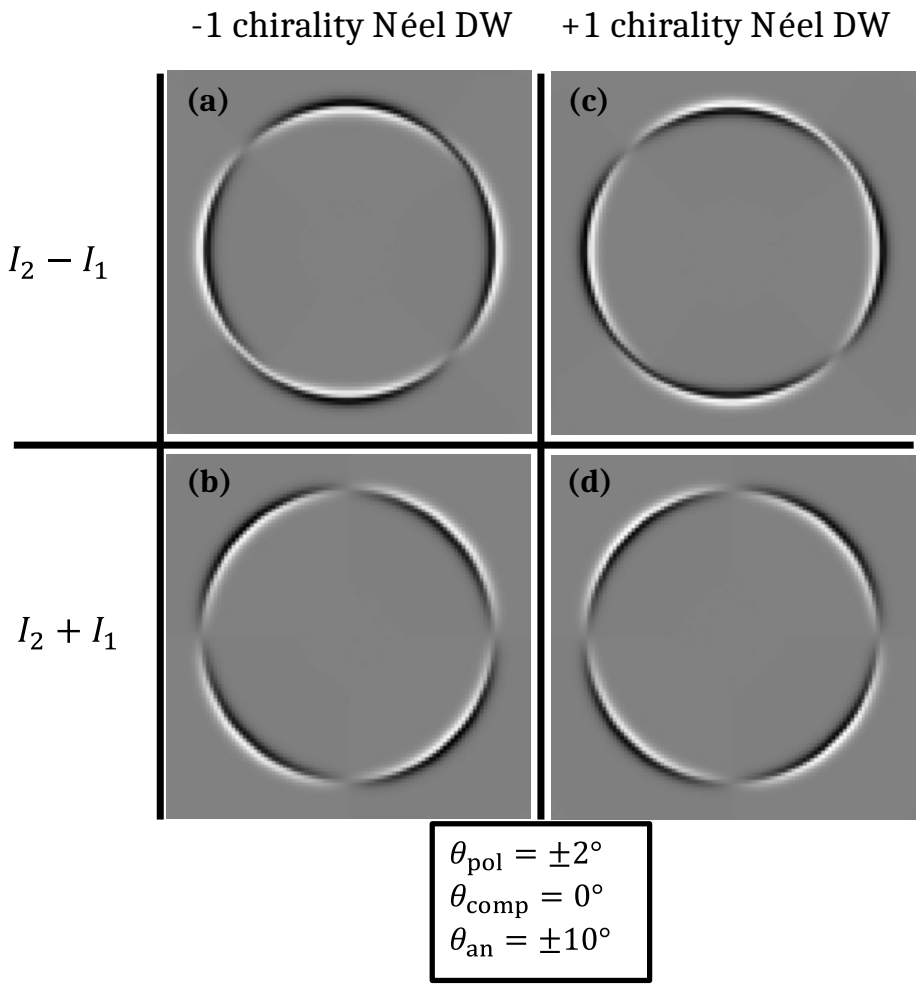

Figure 6.1.: Simulations of gradient effect signal in [Co/Pt] with Néel wall and $\theta_{pol} = \pm 2°$, $\theta_{an} = \pm 10°$ geometry. a) and b) depict subtraction and addition images for -1 wall chirality (magnetic moments pointing inside the bubble), respectively. c) and d) show results for $+1$ wall chirality.

Earlier, we showed simpler experiment geometries requiring a rotation of one element, which could also be used for DW recognition. However, measuring a series of these experiments is advisable since, as shown in Fig. (5.21), the boundary contrast can vary dramatically.

On the experiment front, another practical aspect is that we worked exclusively with the polarizer and analyzer in the presented experiments. However, it appears that manipulating the compensator instead of the analyzer gives almost exactly the same experimental results, which was even supported by simulations. Hence it might be beneficial to choose the compensator as a non-static element in cases where domain contrast cannot be switched by analyzer inversion but by compensator instead.

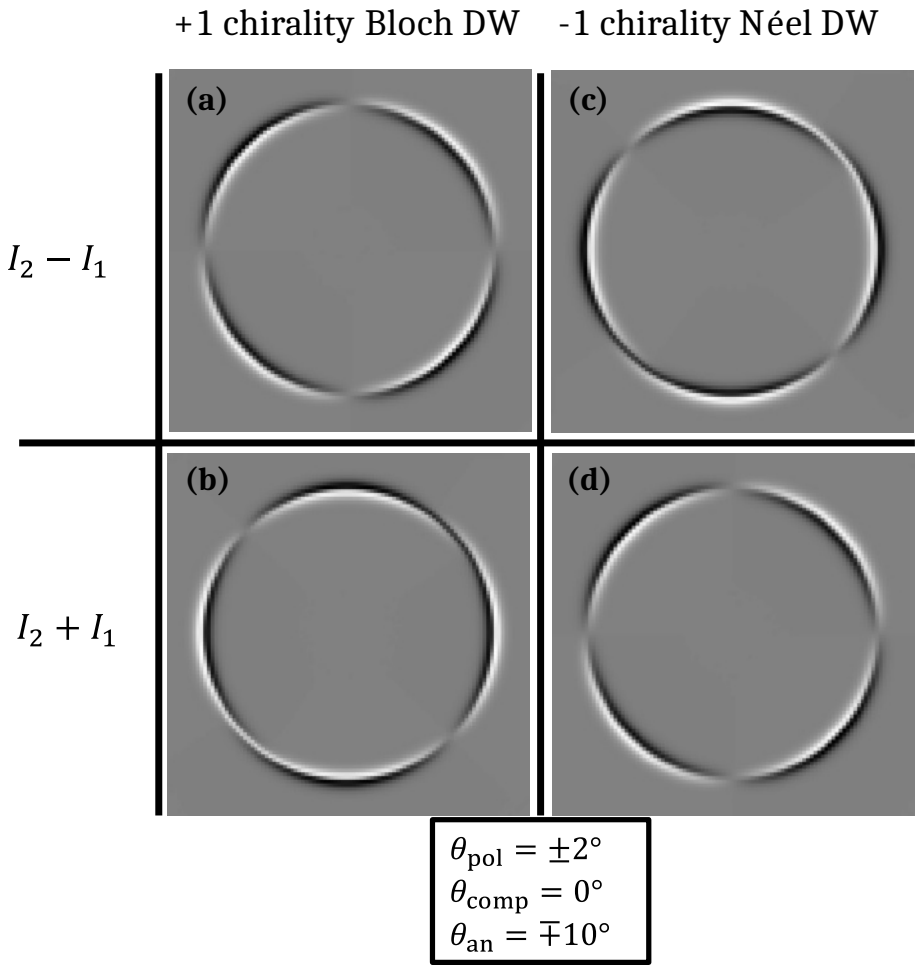

Figure 6.2.: Simulations of gradient effect signal in [Co/Pt] with Bloch wall in $\theta_{pol} = \pm 2°$ and $\theta_{an} = \mp 10°$ geometry. The modeled Bloch wall with +1 chirality (counter clockwise magnetization circulation) a) subtraction, b) addition results. Images c) and d) correspond to -1 chirality Néel wall in the same geometry.

Conclusion

In the presented thesis, we studied the magneto-optical gradient effect phenomenology and its possible utilization in domain wall imaging in systems with perpendicular magnetic anisotropy. The first chapter was devoted to providing a theoretical basis for nanoscale magnetism. We introduced magnetic free energy terms that lead to the formation of non-uniform magnetization configurations called magnetic domains. Then we discussed the most common in-plane and out-of-plane domain types and their accompanying domain walls. We even briefly commented on the magnetic textures reaching the nanometer scale and their promising features for utilization in future devices.

In conjuction with this, we reviewed the most common microscopy techniques used for magnetic imaging. The fundamentals of microscopy methods such as scanning probe microscopy, electron microscopy and finally, magneto-optics were briefly laid. Their drawbacks and advantages were described to provide a comparison between them. Finishing with magneto-optical microscopy, we gradually transitioned to the chapter focusing on the magneto-optical effects.

The third chapter was designed to provide an introduction to magneto-optical effects. Starting from a derivation of magnetization-dependent dielectric permittivity tensors describing Kerr and Voigt effects, their manifestation in experiments and the discovery of the gradient effect were presented. Last, we summarized the literature on the gradient effect, centering on the pioneering studies. We made the case that those studies predominantly focus on in-plane magnetized systems, whereas the perpendicularly magnetized systems were mostly overlooked.

In chapter four, we describe the fabrication of magnetic multilayer systems with perpendicular magnetic anisotropy, with systems based on Co/Pt, Co/Ni, Co/Gd and Fe/Gd multilayers. We also describe their magnetic properties using Kerr microscopy and their subsequent domain wall type determination, ultimately provided by Lorentz transmission electron microscopy.

The core of the thesis is in chapter 5, where the possibility to learn about the internal structure of magnetic domain walls via the magneto-optical gradient effect is discussed. It is firstly concluded that longitudinal Kerr effect microscopy is not reliable for magnetometry of magnetic domain walls in out-of-plane magnetized bubbles, as the arising contrast is largely focus dependent. Therefore bringing forth the hypothesis that the contrast at domain boundaries originates from the gradient effect. Further, we investigated how the individual magnetization gradients look in bubble domains with specific domain wall types. Then we used the magnetization gradients occurring in the dielectric law of gradient effect and suggested multiple experimental geometries in which the magnetization gradient components can be separated. We consequently measured the gradient effect separation in the corresponding proposed geometries and compared it with the analytical dependencies. We found multiple common features; however, there was no no one-to-one correspondence between the phenomenological dielectric tensor and the experimentally measured features. Aiming for a more accurate modeling of the optical experiment, we performed numerical simulations using the transfer matrix method. We then used these simulations to explain more complex experimental geometries, yet still without full correspondence.

Finally, we gathered the features in experiments and simulations that agreed and used them in chapter six to propose experimental geometries to differentiate between Néel and Bloch domain walls in bubble domains. Unfortunately, experimental confirmation was not possible

due to the lack of a perpendicularly magnetized multilayer system with stable bubble domains featuring Bloch walls.

We envision that further work on the exploration of the magneto-optical gradient has the potential to establish an approach based solely on optics to investigate sub-resolution magnetic textures (such as domain walls). Such a method would offer a fast, advantageous and inexpensive pathway for characterizing a large set of nanomagnetic systems that are currently of large interest in domains of scientific research and technical applications.

References

[1] SANDER, D., *et al. The 2017 magnetism roadmap*. Journal of Physics D: Applied Physics, 2017, 50.36: 363001. ISSN 1361-6463. doi:10.1088/1361-6463/aa81a1

[2] PARKIN, S. and S.-H. YANG. *Memory on the racetrack*. Nature Nanotechnology, 2015, 10(3), 195-198. ISSN 1748-3387. doi:10.1038/nnano.2015.41

[3] LUO, Z., *et al. Current-driven magnetic domain-wall logic*. Nature, 2020, 579(7798), 214-218. ISSN 0028-0836. doi:10.1038/s41586-020-2061-y

[4] FERT, A., V. CROS and J. SAMPAIO. *Skyrmions on the track*. Nature Nanotechnology, 2013, 8(3), 152-156. ISSN 1748-3387. doi:10.1038/nnano.2013.29

[5] WANG, X. S., A. QAIUMZADEH and A. BRATAAS. *Current-Driven Dynamics of Magnetic Hopfions*. Physical Review Letters, 2019, 123(14). ISSN 0031-9007. doi:10.1103/PhysRevLett.123.147203

[6] VEDMEDENKO, E. Y., *et al. The 2020 magnetism roadmap*. Journal of Physics D: Applied Physics, 2020, 53.45: 453001. ISSN 1361-6463. doi:10.1088/1361-6463/ab9d98

[7] MA, Y., *et al. A 600-μW ultra-low-power associative processor for image pattern recognition employing magnetic tunnel junction-based nonvolatile memories with autonomic intelligent power-gating scheme*. Japanese Journal of Applied Physics, 2016, 55(4S). ISSN 0021-4922. doi:10.7567/JJAP.55.04EF15

[8] KIMEL, A, *et al. The 2022 magneto-optics roadmap*. Journal of Physics D: Applied Physics, 2022, 55.46: 463003. ISSN 1361-6463. doi:10.1088/1361-6463/ac8da0

[9] HUBERT, A. and R. SCHÄFER. *Magnetic Domains: The Analysis of Magnetic Microstructures*. Springer-Verlag, 1998, ISBN 9783540641087.

[10] KUCH, W., *et al. Magnetic microscopy of layered structures*. Springer, 2015. ISBN 978-3-662-44532-7.

[11] LANGEVIN, P. *Magnétisme et theorie des électrons* (Magnetism and the theory of electrons). Ann. Chim. Phys., 1905, 5, 70–127. ISSN 0368-3893.

[12] WEISS, P. *L'hypothése du champ moléculaire et la propriété ferromagnétique* (The hypothesis of the molecular field and the property of ferromagnetism). J. de Phys. Rad., 1907, 6, 661–690. doi:10.1051/jphystap:019070060066100

[13] COEY, J. M. D. *Magnetism and magnetic materials*. Cambridge university press, 2010.

[14] BITTER, F. *Experiments on the nature of ferromagnetism*. Physical Review, 1932, 41.4: 507. doi:10.1103/PhysRev.41.507

[15] HEISENBERG, W. Zur Theorie des Ferromagnetismus (On the theory of ferromagnetism). Z. Phys, 1928, 49, 619–636. doi:10.1007/BF01328601.

[16] BLUNDELL, S. *Magnetism in Condensed Matter*. London, England: Oxford University Press, 2001.

[17] LANDAU, L. D. and E. M. LIFSHITZ. *Course of theoretical physic*s. Elsevier, 2013.

[18] KRONMÜLLER, H. and S. PARKIN. *Handbook of Magnetism and Advanced Magnetic Materials*. Chichester, UK: John Wiley & Sons, 2007. ISBN 0470022175. doi:10.1002/9780470022184

[19] NOZAKI, Y., *et al. Micromagnetic Structure Analysis of Head-on-Head-Type* 180° *Domain Wall in Submicron Size Co Wires*. Japanese Journal of Applied Physics, 1999, 38(11R). ISSN 0021-4922. doi:10.1143/JJAP.38.6282

[20] SCHÄFER, R., *et al. The magneto-optical gradient effect in an exchange-biased thin film: experimental evidence for classical diffraction theory*. New Journal of Physics, 2010, 12(5). ISSN 1367-2630. doi:10.1088/1367-2630/12/5/053006

[21] NÉEL, L. *Energie des parois de Bloch dans les couches minces*. Comptes Rendus Hebdomadaires Des Seances De L Academie Des Sciences, 1955, 241.6: 533–537.

[22] HUBER, E. E., D. O. SMITH and J. B. GOODENOUGH. *Domain-Wall Structure in Permalloy Films*. Journal of Applied Physics, 1958, 29.3: 294-295. doi:10.1063/1.1723105

[23] VAŇATKA, M., *et al. Magnetic vortex nucleation modes in static magnetic fields*. AIP Advances, 2017, 7.10: 105103.doi:10.1063/1.5006235

[24] DEBLOIS, R. W. and C. D. GRAHAM. *Domain Observations on Iron Whiskers*. Journal of Applied Physics, 1958, 29(6), 931-939. ISSN 0021-8979. doi:10.1063/1.1723334

[25] GRÜNBERG, P. *Layered Magnetic Structures: History, Highlights, Applications*. Physics Today, 2001, 54(5), 31-37. ISSN 0031-9228. doi:10.1063/1.1381100

[26] DEN BROEDER, F.J.A., W. HOVING and P.J.H. BLOEMEN. *Magnetic anisotropy of multilayers*. Journal of Magnetism and Magnetic Materials, 1991, 93, 562-570. ISSN 03048853. doi:10.1016/0304-8853(91)90404-X

[27] HELLWIG, O., *et al. Domain structure and magnetization reversal of antiferromagnetically coupled perpendicular anisotropy films*. Journal of Magnetism and Magnetic Materials , 2007, 319(1-2), 13-55. ISSN 03048853. doi:10.1016/j.jmmm.2007.04.035

[28] VAŇATKA, M., *et al. Velocity asymmetry of Dzyaloshinskii domain walls in the creep and flow regimes*. Journal of Physics: Condensed Matter, 2015, 27(32). ISSN 0953-8984. doi:10.1088/0953-8984/27/32/326002

[29] CHEN, G., *et al. Novel Chiral Magnetic Domain Wall Structure in Fe/Ni/Cu (001) Films*. Physical Review Letters, 2013, 110(17). ISSN 0031-9007. doi:10.1103/PhysRevLett.110.177204

[30] DZYALOSHINSKII, I. *A thermodynamic theory of "weak" ferromagnetism of antiferromagnetics*. Journal of Physics and Chemistry of Solids, 1958, 4(4), 241-255. ISSN 00223697. doi:10.1016/0022-3697(58)90076-3

[31] MORIYA, T. *Anisotropic Superexchange Interaction and Weak Ferromagnetism*. Physical Review, 1960, 120(1), 91-98. ISSN 0031-899X. doi:10.1103/PhysRev.120.91

[32] BODE, M., *et al. Chiral magnetic order at surfaces driven by inversion asymmetry*. Nature, 2007, 447(7141), 190-193. ISSN 0028-0836. doi:10.1038/nature05802

[33] STREUBEL, R., *et al. Magnetism in curved geometries*. Journal of Physics D: Applied Physics, 2016, 49(36). ISSN 0022-3727. doi:10.1088/0022-3727/49/36/363001

[34] SHEKA, D. D. *A perspective on curvilinear magnetism*. Applied Physics Letters, 2021, 118(23). ISSN 0003-6951. doi:10.1063/5.0048891

[35] CHEN, G., *et al. Tailoring the chirality of magnetic domain walls by interface engineering*. Nature Communications, 2013, 4(1). ISSN 2041-1723. doi:10.1038/ncomms3671

[36] HRABEC, A., *et al. Measuring and tailoring the Dzyaloshinskii-Moriya interaction in perpendicularly magnetized thin films*. Physical Review B, 2014, 90(2). ISSN 1098-0121. doi:10.1103/PhysRevB.90.020402

[37] FINOCCHIO, G., *et al. Magnetic skyrmions: from fundamental to applications*. Journal of Physics D: Applied Physics, 2016, 49(42). ISSN 0022-3727. 10.1088/0022-3727/49/42/423001

[38] QIN, G., *et al. Magnetic-Field-Assisted Diffusion Motion of Magnetic Skyrmions*. ACS Nano, 2022, 16(10), 15927-15934. ISSN 1936-0851. doi:10.1021/acsnano.2c03046

[39] SAMPAIO, J., *et al. Nucleation, stability and current-induced motion of isolated magnetic skyrmions in nanostructures*. Nature Nanotechnology, 2013, 8(11), 839-844. ISSN 1748-3387. doi:10.1038/nnano.2013.210

[40] EVERSCHOR-SITTE, K., and SITTE, M. *The vector field of two-dimensional magnetic skyrmions*, 2015, Wikimedia Commons. https://en.wikipedia.org/wiki/Magnetic_skyrmion#/media/File:2skyrmions.PNG (accessed Apr 23, 2023)

[41] REMOISSENET, M. and J. A. WHITEHEAD. *Waves Called Solitons: Concepts and Experiments*. American Journal of Physics, 1995, 63(4), 381-382. ISSN 0002-9505. doi:10.1119/1.18083

[42] ZANG, J., V. CROS and A. HOFFMANN. *Topology in Magnetism*. Cham: Springer International Publishing. Springer Series in Solid-State Sciences, 2018, ISBN 978-3-319-97333-3. doi:10.1007/978-3-319-97334-0

[43] JIANG, W., *et al. Blowing magnetic skyrmion bubbles*. Science, 2015, 349(6245), 283-286. ISSN 0036-8075. doi:10.1126/science.aaa1442

[44] WOO, S., *et al. Observation of room-temperature magnetic skyrmions and their current-driven dynamics in ultrathin metallic ferromagnets*. Nature Materials, 2016, 15(5), 501-506. ISSN 1476-1122. doi:10.1038/nmat4593

[45] JIANG, W., *et al. Direct observation of the skyrmion Hall effect*. Nature Physics, 2017, 13(2), 162-169. ISSN 1745-2473. doi:10.1038/nphys3883

[46] RYBAKOV, F. *Magnetic hopfions in solids*. APL Materials, 2022, 10(11). ISSN 2166-532X. doi:10.1063/5.0099942

[47] NAVAS, D., *et al. Domain-wall structure in thin films with perpendicular anisotropy: Magnetic force microscopy and polarized neutron reflectometry study*. Physical Review B, 2014, 90(5). ISSN 1098-0121. doi:10.1103/PhysRevB.90.054425

[48] HSIEH, C.T., J.Q. LIU and J.T. LUE. *Magnetic force microscopy studies of domain walls in nickel and cobalt films*. Applied Surface Science, 2005, 252(5), 1899-1909. Available at: doi:10.1016/j.apsusc.2005.05.041

[49] ZHU, J.-G., Y. ZHENG and X. LIN. *Micromagnetics of small size patterned exchange biased Permalloy film elements (invited)*. Journal of Applied Physics, 1997, 81(8), 4336-4341. ISSN 0021-8979. doi:10.1063/1.364761

[50] RAVE, W., *et al. Observations on high-anisotropy single crystals using a combined Kerr/magnetic force microscope*. Journal of Magnetism and Magnetic Materials, 1998, 177-181, 1474-1475. ISSN 03048853. doi:10.1016/S0304-8853(97)00793-2

[51] CASIRAGHI, A., *et al. Individual skyrmion manipulation by local magnetic field gradients*. Communications Physics, 2019, 2(1). doi:10.1038/s42005-019-0242-5

[52] HELLWIG, O., A. BERGER and E. E. FULLERTON.*Domain Walls in Antiferromagnetically Coupled Multilayer Films*. Physical Review Letters, 2003, 91(19). ISSN 0031-9007. doi:10.1103/PhysRevLett.91.197203

[53] THIAVILLE, A.,L. BELLIARD and J. MILTAT. *Micromagnetism and the interpretation of magnetic force microscopy images*. In: Scanning Microsc., accepted, Proc. Conf."Scanning Microscopy International" Chicago. 1997.

[54] TAYLOR, J. M., *et al. High-sensitivity diamond magnetometer with nanoscale resolution*. Nature Physics, 2008, 4(10), 810-816. ISSN 1745-2473. doi:10.1038/nphys1075

[55] TETIENNE, J.-P., *et al. The nature of domain walls in ultrathin ferromagnets revealed by scanning nanomagnetometry*. Nature Communications, 2015, 6(1). ISSN 2041-1723. doi:10.1038/ncomms7733

[56] KOIKE, K. *Spin-polarized scanning electron microscopy*. Microscopy, 2013, 62(1), 177-191. ISSN 2050-5698. doi:10.1093/jmicro/dfs092

[57] CORREDOR, E. C., *et al. SEMPA investigation of the Dzyaloshinskii-Moriya interaction in the single, ideally grown Co/Pt(111) interface*. Physical Review B, 2017, 96(6). ISSN 2469-9950. doi:10.1103/PhysRevB.96.060410

[58] SENG, B., *et al. Direct Imaging of Chiral Domain Walls and Néel-Type Skyrmionium in Ferrimagnetic Alloys*. Advanced Functional Materials, 2021, 31(33). ISSN 1616-301X. doi:10.1002/adfm.202102307

[59] ZHOU, X., *et al. Magnetic surface domain imaging of uncapped epitaxial FeRh(001) thin films across the temperature-induced metamagnetic transition*. AIP Advances, 2016, 6(1). ISSN 2158-3226. doi:10.1063/1.4940758

[60] ALTMAN, M. S. *Trends in low energy electron microscopy*. Journal of Physics: Condensed Matter, 2010, 22(8). ISSN 0953-8984. doi:10.1088/0953-8984/22/8/084017

[61] DUDEN, T. and E. BAUER. *Spin-Polarized Low Energy Electron Microscopy*. Surface Review and Letters, 2012, 05(06), 1213-1219. ISSN 0218-625X. doi:10.1142/S0218625X98001547

[62] ROUGEMAILLE, N. and A. K. SCHMID. *Magnetic imaging with spin-polarized low-energy electron microscopy*. The European Physical Journal Applied Physics, 2010, 50(2). ISSN 1286-0042. doi:10.1051/epjap/2010048

[63] ROBERTSON, MC., *et al. In-plane Néel wall chirality and orientation of interfacial Dzyaloshinskii-Moriya vector in magnetic films*. Physical Review B, 2020, 102(2). ISSN 2469-9950. doi:10.1103/PhysRevB.102.024417

[64] TANG, J., *et al. Lorentz transmission electron microscopy for magnetic skyrmions imaging*. Chinese Physics B, 2019, 28(8). ISSN 1674-1056. doi:10.1088/1674-1056/28/8/087503

[65] BENITEZ, M. J., *et al. Magnetic microscopy and topological stability of homochiral Néel domain walls in a Pt/Co/AlO_x trilayer*. Nature Communications, 2015, 6(1). ISSN 2041-1723. doi:10.1038/ncomms9957

[66] NELLIST, P. D., *et al. Direct Sub-Angstrom Imaging of a Crystal Lattice*. Science, 2004, 305(5691), 1741-1741. doi:10.1126/science.1100965

[67] POLLARD, S. D., *et al. Bloch Chirality Induced by an Interlayer Dzyaloshinskii-Moriya Interaction in Ferromagnetic Multilayers*. Physical Review Letters, 2020, 125(22). ISSN 0031-9007. doi:10.1103/PhysRevLett.125.227203

[68] MCCORD, J. *Progress in magnetic domain observation by advanced magneto-optical microscopy*. Journal of Physics D: Applied Physics, 2015, 48(33). ISSN 0022-3727. doi:10.1088/0022-3727/48/33/333001

[69] FISCHER, P. *Viewing spin structures with soft X-ray microscopy*. Materials Today, 2010, 13(9), 14-22. ISSN 13697021. doi:10.1016/S1369-7021(10)70161-9

[70] FISCHER, P., and FADLEY., Ch. S. *Probing nanoscale behavior of magnetic materials with soft X-ray spectromicroscopy*. Nanotechnology Reviews, 2012, 1(1), 5-15. ISSN 2191-9097. 10.1515/ntrev-2011-0001

[71] FISCHER, P., *et al. Magnetic imaging with full-field soft X-ray microscopies*. Journal of Electron Spectroscopy and Related Phenomena, 2013, 189, 196-205. ISSN 03682048. doi:10.1016/j.elspec.2013.03.012

[72] LUO, C., CHEN, K., UKLEEV, *et al. Direct observation of Néel-type skyrmions and domain walls in a ferrimagnetic thin film via scanning transmission X-ray microscopy*. arXiv:2304.13698

[73] PERSHAN, P. S. *Magneto-Optical Effects*. Journal of Applied Physics, 1967, 38(3), 1482-1490. ISSN 0021-8979. doi:10.1063/1.1709678

[74] AULD, B. A. and D. A. WILSON. *Bragg Scattering of Infrared Radiation from Coherent Spin Waves*. Journal of Applied Physics, 1967, 38(8), 3331-3336. ISSN 0021-8979. doi:10.1063/1.1710108

[75] WETTLING, W. *Magneto-optics of ferrites*. Journal of Magnetism and Magnetic Materials, 1976, 3(1-2), 147-160. ISSN 03048853. doi:10.1016/0304-8853(76)90026-3

[76] VISNOVSKY, S. *Optics in Magnetic Multilayers and Nanostructures*. CRC Press, 2006. ISBN 9781420019193.

[77] XU, J., *et al. Imaging antiferromagnetic domains in nickel oxide thin films by optical birefringence effect*. Physical Review B, 2019, 100(13). ISSN 2469-9950. doi:10.1103/PhysRevB.100.134413

[78] XU, J., *et al. Optical imaging of antiferromagnetic domains in ultrathin CoO(001) films*. New Journal of Physics, 2020, 22(8). ISSN 1367-2630. doi:10.1088/1367-2630/aba1b4

[79] SCHÄFER, R. and A. HUBERT. *A new magnetooptic effect related to non-uniform magnetization on the surface of a ferromagnet*. Physica status solidi (a), 1990, 118(1), 271-288. ISSN 00318965. doi:10.1002/pssa.2211180131

[80] SCHÄFER, R., M. RÜHRIG and A. HUBERT. *Magnetooptical Domain Wall Observation at Perpendicular Incidence*. Physica Status Solidi (a), 1994, 145(1), 167-176. ISSN 00318965. doi:10.1002/pssa.2211450116

[81] THIAVILLE, A., A. HUBERT and R. SCHÄFER. *An isotropic description of the new-found gradient-related magneto-optical effect (invited)*. Journal of Applied Physics, 1991, 69(8), 4551-4555. ISSN 0021-8979. doi:10.1063/1.348307

[82] KAMBERSKÝ, V. *The Schäfer-Hubert magneto-optical effect and classical gyrotropy in light-wave equations*. Journal of Magnetism and Magnetic Materials, 1992, 104-107, 311-312. ISSN 03048853. doi:10.1016/0304-8853(92)90811-2

[83] TRAEGER, G., L. WENZEL and A. HUBERT. *Computer experiments on the information depth and the figure of merit in magnetooptics*. Physica Status Solidi (a), 1992, 131(1), 201-227. ISSN 00318965. doi:10.1002/pssa.2211310131

[84] TRAEGER, G., *et al. Magnetooptical effects in non-uniformly magnetized media*. IEEE Transactions on Magnetics, 1993, 29(6), 3408-3410. ISSN 0018-9464. doi:10.1109/20.280830

[85] WENZEL, L., V. KAMBERSKÝ and A. HUBERT. *A systematic first-order theory of magnetooptic diffraction in magnetic multilayers*. Physica Status Solidi (a), 1995, 151(2), 449-466. ISSN 00318965. doi:10.1002/pssa.2211510223

[86] KAMBERSKÝ, V., L. WENZEL and A. HUBERT. *Magneto-optical interference and diffraction in isotropic and uniaxial multilayers*. Journal of Magnetism and Magnetic Materials, 1998, 189(2), 149-164. ISSN 03048853. hrefhttps://doi.org/10.1016/S0304-8853(98)00214-5

[87] CAO, A., *et al. Dynamics of all-optically switched magnetic domains in Co/Gd heterostructures with Dzyaloshinskii-Moriya interaction*. Physical Review B, 2020, 102(10). ISSN 2469-9950. doi:10.1103/PhysRevB.102.104412

[88] WENZEL, L. and A. HUBERT. *Simulating magnetooptic imaging with the tools of Fourier optics*. IEEE Transactions on Magnetics, 1996, 32(5), 4084-4086. ISSN 00189464. doi:10.1109/20.539271

[89] SCHÄFER, R., M. RUHRIG and A. HUBERT. *Exploration of a new magnetization-gradient-related magnetooptical effect*. IEEE Transactions on Magnetics, 1990, 26(5), 1355-1357. ISSN 00189464. doi:10.1109/20.104374

[90] BERREMAN, D. W. *Optics in Stratified and Anisotropic Media: 4×4-Matrix Formulation*. Journal of the Optical Society of America, 1972, 62(4). ISSN 0030-3941. doi:10.1364/JOSA.62.000502

[91] YEH, P. *Optics of anisotropic layered media: A new 4 × 4 matrix algebra*. Surface Science, 1980, 96(1-3), 41-53. ISSN 00396028. doi:10.1016/0039-6028(80)90293-9

[92] WÖHLER, H., *et al. Faster 4 × 4 matrix method for uniaxial inhomogeneous media*. Journal of the Optical Society of America A, 1988, 5(9). ISSN 1084-7529. doi:10.1364/JOSAA.5.001554

[93] SCHUBERT, M. *Polarization-dependent optical parameters of arbitrarily anisotropic homogeneous layered systems*. Physical Review B, 1996, 53(8), 4265-4274. ISSN 0163-1829. doi:10.1103/PhysRevB.53.4265

[94] SCHUBERT, M., T. E. TIWALD and J. A. WOOLLAM. *Explicit solutions for the optical properties of arbitrary magneto-optic materials in generalized ellipsometry*. Applied Optics, 1999, 38(1). ISSN 0003-6935. doi:10.1364/AO.38.000177

[95] JONES, R. C. *A New Calculus for the Treatment of Optical SystemsI Description and Discussion of the Calculus*. Journal of the Optical Society of America, 1941, 31(7). ISSN 0030-3941. doi:10.1364/JOSA.31.000488

[96] POLYANSKIY M. N. *Refractive Index Database* [online]. 2008–2023. Available at: refractiveindex.info

[97] ROBINSON, C. C. *Longitudinal Kerr Magneto-Optic Effect in Thin Films of Iron, Nickel, and Permalloy*. Journal of the Optical Society of America, 1963, 53(6). ISSN 0030-3941. doi:10.1364/JOSA.53.000681

[98] BALLANTYNE, J. M. *Kerr Magneto-Optic Effect in Thin Cobalt Films*. Journal of the Optical Society of America, 1964, 54(11). ISSN 0030-3941. doi:10.1364/JOSA.54.001352

List of abbreviations

CMOS	complemetary metal-oxide-semiconductor
DMI	Dzyaloshinskii-Moriya interaction
DW	domain wall
HDD	hard disk drive
LCP	left circular polarization
LEEM	low energy electron microscopy
L-TEM	Lorentz transmission electron microscopy
MFM	magnetic force microscopy
ML	monolayer
MO	magneto-optical / magneto-optics
MRAM	magnetic random access memory
NV	nitrogen vacancy
PMA	perpendicular magnetic anisotropy
RCP	right circular polarization
SEM	scanning electron microscopy
SEM-PA	scanning electron microscopy with polarization analysis
SP-LEEM	spin-polarized low energy electron microscopy
SP-STM	spin-polarized scanning tunneling microscopy
SOT	spin-orbit torque
STT	spin-transfer torque
TEM	transmission electron microscopy
XMCD	X-ray magnetic circular dichroism
XMLD	X-ray magnetic linear dichroism

A. Transfer matrix method

Transfer matrix connects the incident light polarization amplitudes with the reflected and transmitted ones. Since this transfer matrix describes the optical properties of the system, it is possible to find general solutions connecting the transfer matrix elements with Fresnel reflection coefficients.

However, most importantly, the transfer matrix of the whole system is at first divided into partial transfer matrices describing individual layers of the system. The dielectric permittivity tensors of the individual layers then enter the partial matrices, and then the calculus is applied to obtain the Fresnel reflection matrix.

Because the presence of magnetization in magnetic media presents an anisotropy in optical properties, and the optical response is also linear, it is possible to use the transfer matrix method in conventional magneto-optics. Moreover, it is highly beneficial for our gradient effect observations since we already know its permittivity tensor. Due to the high complexity of the transfer matrix method calculus, the polarization dependent reflectivity can only be computed numerically.

Another useful methodology for our purposes is the Jones formalism [95]. Jones formalism is a method used in polarization optics utilizing a matrix notation to represent the polarization state of the light and its change upon interaction with other optical elements. Typically, the incident light E_0 is represented by a column vector of its $x-$ and $y-$ polarization components

$$J = \begin{pmatrix} E_{0x}e^{i\phi_x} \\ E_{0y}e^{i\phi_y} \end{pmatrix}, \tag{A.1}$$

where ϕ_x and ϕ_y denote the corresponding phases of their polarization components. As the light passes through the optical setup M, its polarization state is modified as

$$J' = M \cdot J = M_1 \cdot M_2 \cdot ... \cdot M_n \cdot J, \tag{A.2}$$

where we can split the matrix describing the whole system M into separate matrices M_1, M_2, ..., M_n, each representing individual optical elements of the system.

The description of the experiments we deal with in the Kerr microscope setup only need four matrices to describe. The four matrices are the polarizer P, the reflection matrix R of the sample, the compensator C ($\lambda/4$-wave plate), and the analyzer A. In practice, the unpolarized light J_0 is polarized by the polarizer, it is reflected off the sample, passes through the compensator and analyzer, and finally, J_{out} is detected by the camera; in Jones formalism, we can write it as follows

$$J_{\text{out}} = A \cdot C \cdot R \cdot P \cdot J_0. \tag{A.3}$$

Matrices P, C and A can be easily obtained analytically and are formally written in Appendix B. Since we get the reflection matrix R from the transfer matrix method, we now know all the quantities on the right-hand side of the equation (above). Using this approach, we can just define the rotation angles of the polarization optics elements and find the final Jones vector that makes it to the detector. Taking $J_{\text{out}} \cdot J^*_{\text{out}} = I_{\text{detect}}$ gives us the detected intensity. Therefore, we can eventually simulate the gradient effect signal in particular setting of choice of the optical elements.

For the numerical simulations, we scripted a MatLab code. Our script is based on a code developed by Jon Arregi, PhD., which was primarily accustomed to magneto-optical Kerr ellipsometry and based on the work by Schubert *et al.* [94]. In the original code, the examined

layered system is defined by the layers' thicknesses, corresponding optical parameters (refractive index and Voigt constants, see Tab. (A.1)), and the uniform magnetization orientation if the layer is magnetic. This script used the Kerr effect permittivity tensor to get the reflection matrix via the transfer matrix method and, ultimately, was able to simulate the Kerr rotation and ellipticity upon reflection.

The modification implemented in this thesis to this code was the possibility of defining a non-uniform magnetization state. Since the domain state we observe in experiments is an out-of-plane bubble domain, we also modelled the magnetization state in a discrete xy grid according to a radial one-dimensional DW model following Eqs. (1.5) and (1.6) . Every matrix element then contained a full magnetization vector. Further, individual gradient components were calculated and inserted into the permittivity tensor. Other modifications allowed us to apply the transfer matrix method to every element of the xy grid and thus obtain the whole reflectivity matrix at each site of the modeled bubble domain. In the next step, the Jones formalism was used to calculate detected intensity point in each element of the matrix.

Table A.1.: Optical parameters used for transfer matrix method simulations, extracted from Refs. 96–98. While the experiments encompass a broad spectrum in the visible light region, simulations were performed at $\lambda = 532$ nm (green) for the sake of simplicity.

material	n [-]	Q_V [-]
Pt	0.4809 + 4.8707i	-
Co	2.0014+ 3.735i	0.0262 + 0.0072i
Gd	1.775 + 2.615i	-
Ta	1.1412 + 4.7151i	-
Ni	1.8775 + 3.4946i	0.0059 - 0.0057i
Si	4.152 + 0.051787i	-
SiO_2	1.4607	-

B. Light polarization and optical components in the Jones formalism

We recover the general definition of the Jones vector to represent polarized light as

$$J = \begin{pmatrix} E_x \\ E_y \end{pmatrix} = \begin{pmatrix} E_{0x}\, e^{i\phi_x} \\ E_{0y}\, e^{i\phi_y} \end{pmatrix}. \tag{B.1}$$

In the following, we may indicate the Jones representations of a set of most common polarization states using this notation. For instance, linearly polarized light with a slope α can be represented as [10]

$$J_\alpha = \begin{pmatrix} \cos\alpha \\ \sin\alpha \end{pmatrix}, \tag{B.2}$$

while both types of circular polarization are expressed as

$$J_{RCP} = \frac{1}{\sqrt{2}} \begin{pmatrix} 1 \\ -i \end{pmatrix}, J_{LCP} = \frac{1}{\sqrt{2}} \begin{pmatrix} 1 \\ i \end{pmatrix}. \tag{B.3}$$

On the other hand, the Jones vector for the most general elliptical polarization state is

$$J_{ell} = \begin{pmatrix} \cos\Omega \\ \sin\Omega e^{i\Delta\phi} \end{pmatrix}, \tag{B.4}$$

where $\Omega = \arctan\left(E_{0y}/E_{0x}\right)$. Furthermore, the individual components of the $\boldsymbol{E}$-vector may be written in the Jones formalism as follows,

$$J_x = \begin{pmatrix} 1 \\ 0 \end{pmatrix}, J_y = \begin{pmatrix} 0 \\ 1 \end{pmatrix}. \tag{B.5}$$

Because the two components are orthogonal, $J_x \cdot J_y^* = 0$, the two vector form a basis and they are therefore suitable for defining all other polarization states, for example, both circular polarizations:

$$J_{RCP} = \frac{1}{\sqrt{2}} \left(J_x - iJ_y\right), J_{LCP} = \frac{1}{\sqrt{2}} \left(J_x + iJ_y\right). \tag{B.6}$$

We might notice that even $J_{RCP} \cdot J_{LCP}^* = 0$ fulfills, which also means that the RCP and LCP polarization states are orthogonal (and orthornomal), and hence can be used to describe all possible polarization states; for instance, linearly polarized light can be expressed as

$$J_x = \frac{1}{\sqrt{2}} \left(J_{RCP} + J_{LCP}\right), J_y = \frac{i}{\sqrt{2}} \left(J_{RCP} - J_{LCP}\right). \tag{B.7}$$

In addition, we describe here the 2×2 Jonex matrix representation of exemplary optical components acting on the polarization state of light. One of the simplest optical elements is a polarizer. The key role of the polarizer is to change the initial polarization state to a

specific pre-defined state. There are different types of polarizers based on different physical principles, such as absorptive, reflective polarizers, etc. In the following, we will focus on absorptive polarizers.

Absorptive polarizers are made of specific materials whose crystal structure shows optical anisotropy [10]. Linear polarization passing through certain axes remains unchanged, while perpendicular polarization is absorbed; such material is called dichroic. The Jones matrix describing a polarizer polarizing (i.e., letting pass) the incident light along the $x-$axis is given by

$$A_{pol} = \begin{pmatrix} 1 & 0 \\ 0 & 0 \end{pmatrix}. \tag{B.8}$$

If we want to polarize the incoming light along a specified angle α_{pol}, we need to apply a rotational matrix and inverse rotational matrix, leading to

$$A_{pol,\alpha} = \begin{pmatrix} \cos\alpha & -\sin\alpha \\ \sin\alpha & \cos\alpha \end{pmatrix} \begin{pmatrix} 1 & 0 \\ 0 & 0 \end{pmatrix} \begin{pmatrix} \cos\alpha & \sin\alpha \\ -\sin\alpha & \cos\alpha \end{pmatrix} = \begin{pmatrix} \cos\alpha^2 & \cos\alpha\sin\alpha \\ \cos\alpha\sin\alpha & \sin\alpha^2 \end{pmatrix}. \tag{B.9}$$

Another optical element of interest in polarization microscopy is a compensator or phase retarder. The compensator is made of a material that is said to be birefringent. Generally, birefringent materials are the ones that have two different indices of refraction. The incoming light is split into two rays in uniaxial materials, called ordinary and extraordinary, which are perpendicularly polarized. Each ray (or polarization state) experiences a different index of refraction as it passes through the material.

The optical axis with a lower index of refraction is called the fast axis, and the other is termed as the slow axis. This principle is used to modify the incoming polarization state. Using a suitable birefringent plate of a certain thickness, we may compensate the path difference between the two perpendicular polarizations, introducing an effective phase shift between the two. We call such a device a compensator.

In wide-field microscopy, the most used compensators are Brace-Köhler compensators because they cause a homogeneous wavelength-dependent phase shift [9]. Depending on the path difference, there are quarter-wave (i.e. $\lambda/4$) and half-wave (i.e. $\lambda/2$) plates. For instance, incoming light polarized along the x-axis, $J_{in} = \begin{pmatrix} 1 \\ 0 \end{pmatrix}$, passes through a quarter-wave plate with the fast axis rotated by 45°, represented by Jones matrix:

$$A_{qwp} = \frac{1}{\sqrt{2}} \begin{pmatrix} 1 & -i \\ -i & 1 \end{pmatrix}. \tag{B.10}$$

The emerging polarization will be

$$J_{out} = A_{qwp} \cdot J_{in} = \frac{1}{\sqrt{2}} \begin{pmatrix} 1 \\ -i \end{pmatrix}, \tag{B.11}$$

which is a right-circular polarization, or RCP. Of course, the quarter-wave plate can be used vice versa, to change the elliptical or circular polarization to (nearly) linearly polarized light.